

Costa Rica Institute of Technology  
Department of Electronics Engineering



**Analysis and Extension of Segmented Physics-Based Via  
Modeling for Microstrip Transitions and Differential Signaling**

Graduate thesis to obtain the academic degree of Master of Science (M.Sc.) in  
Electronics Engineering: option in Microelectronics

Jonathan Cedeño Chaves

Cartago, Costa Rica

Declaro que el presente documento de tesis ha sido realizado enteramente por mi persona, utilizando y aplicando literatura referente al tema e introduciendo conocimientos y resultados experimentales propios.

En los casos en que he utilizado bibliografía he procedido a indicar las fuentes mediante las respectivas citas bibliográficas. En consecuencia, asumo la responsabilidad total por el trabajo de tesis realizado y por el contenido del presente documento.

Jonathan Cedeño Chaves

Cartago, 03 de Mayo, 2022

Cédula: 3-0455-0409

Instituto Tecnológico de Costa Rica  
Escuela de Ingeniería Electrónica  
Tesis de Maestría  
Tribunal Evaluador

Tesis de maestría defendida ante el presente Tribunal Evaluador como requisito para optar por el grado académico de maestría, del Instituto Tecnológico de Costa Rica.

Miembros del Tribunal

---

Dr. Juan Carlos Rojas Fernández  
Profesor Lector

---

M.Sc. Aníbal Coto Cortés  
Profesor Lector



---

M.Sc. Álvaro Camacho Mora  
Evaluador Externo

---

Dr.-Ing. Renato Rímolo Donadío  
Profesor Asesor

Los miembros de este Tribunal dan fe de que la presente tesis de maestría ha sido aprobada y cumple con las normas establecidas por la Escuela de Ingeniería Electrónica.

Cartago, 03 de Mayo, 2022



# Abstract

This work revisits the framework of physics-based modeling of multilayer substrates with vias. The first part reviews the model and discuss their limitations for irregular structures, when there exist cases where high-order modes are excited because of different situations, such as non-uniform current distributions, coupling between nearby interconnections, etc. Some of these irregular cases are not covered in the current physics-based modeling framework. From there, two aspects are explored in this work.

First, an extension of the physics-based via modeling is proposed, in order to handle microstrip line transitions on the bottom or top layers. This is implemented by using a simple model for the via to microstrip line transition that works up to 12 GHz. Here, the construction of a generalized network model is also discussed, and the proposed model is validated against full-wave methods, i.e. FEM, FIT; in order to evaluate the agreement between baseline cases and the proposed modeling approaches.

Second, the role of asymmetries in differential structures with stub vias is studied. It is shown that mode conversion can become an important source of degradation in differential links. These remnants via stubs can be present because of multiple reasons, such as residual stubs due to process tolerances or errors during back-drilling. Different via configurations are analyzed through full-wave simulations. Results show a large impact on mode conversion with an increment of around -35 and -15 dB when the residual stub difference changes from 2 to 14 mil at the fundamental frequency of 17.5 GHz. Furthermore, an estimation approach of the amount of mode conversion as a function of via stub asymmetry is analyzed and proposed.

**Author Key-words:** physics-based via modeling (PBV), printed circuit board (PCB), signal integrity, microstrip, via modeling, via stubs, mode conversion.

*All We Need is Love...*

# Acknowledgments

This thesis is result of my work as a graduate research assistant at the Electronics Engineering Department, Costa Rica Institute of Technology. During this time, some collaborations with the Institute of Electromagnetic Theory, Hamburg University of Technology, have contributed to the success of this investigation.

First, I want to express my deep gratitude to my advisor Prof. Dr.-Ing. Renato Rímolo Donadío. It is difficult to find the precise words to express my gratitude for his mentoring, honest feedback, professional advice, high principles, ethics, and more importantly, the good human being he is. I am indebted to him for providing me the confidence to keep working and growing professionally. In this same way, I would also like to express my gratitude to Prof. Dr. Juan Carlos Rojas Fernández, for all his guidance and professional advice, as well as his encouragement to pursue different goals for my career path. As part of the examiners, I want to thank also Prof. M.Sc. Aníbal Coto Cortés, for his careful review and worth feedback on this work. In addition, I would like to express my gratitude to Prof. Dr. Christian Schuster, Head of the Institute of Electromagnetic Theory, Hamburg University of Technology, for all his mentoring and help during my time working as an academic guest under his supervision.

Como parte de mis agradecimientos, no puedo dejar de lado el expresarle mi más profunda gratitud, cariño y respeto a mi padres Alexis y Siria. Sin ustedes nada de esto sería posible, por lo que esta tesis es por y para ustedes. Espero poder devolverles un poco de los muchos sacrificios que han hecho por mi bienestar. Adicionalmente, quiero expresar mi gratitud y cariño hacia algunos amigos y colegas que han sido parte importante en este proceso. Quiero hacer una mención especial a Gustavo, el cual fue el compañero perfecto de laboratorio durante mi tiempo en la universidad. Además, me gustaría agradecer a otras personas que me han apoyado durante este tiempo, como lo son Billy, Jonathan, Esteban, Arleen, Jonatan, Johanna, Marva, Johan, etc. Mis sinceras disculpas si he omitido a alguien, francamente no alcanzarían las páginas para agradecerle a todas las personas que lo merecen.

Finalmente, me gustaría expresar mi eterna gratitud y cariño a Paulina, quien ha sido mi especial apoyo y fuente de motivación en esta etapa final del trabajo. Muchas gracias por los sacrificios que vos también has hecho en este proceso, me has apoyado y alentado a no desfallecer y cumplir mis sueños. Esta tesis es también para vos...



# Contents

List of Figures	iii
List of Tables	ix
<b>1 Introduction</b>	<b>1</b>
1.1 Motivation and Context	1
1.2 Objectives	3
1.3 Organization	4
<b>2 Segmented Physics-Based Via Modeling of Multilayer Substrates</b>	<b>5</b>
2.1 Review of Physics-Based Via Modeling Formulation	6
2.1.1 Far-field Interaction Modeling	6
2.1.2 Description of the Near-field Modeling	8
2.1.3 Modeling Extension Including Power/Ground Vias and Stripline Traces	13
2.2 Analysis of Irregular Configurations in Multilayer Substrates	16
2.2.1 Microstrip-to-Via Transitions	16
2.2.2 Analytical Description for Microstrip Lines	18
2.2.3 Extraction of Fringing Capacitances of Turning Vias	20
<b>3 Validation of Physics-Based Via Modeling and Irregular Configurations</b>	<b>25</b>
3.1 Simulation of Physics-Based Via Modeling in Multilayer Substrates	26
3.2 Analysis of Irregular Configurations for Via Modeling	29
3.2.1 Considerations of Microstrip-to-Via Transitions	29
<b>4 Extension of Physics-Based Via Modeling for Microstrip Transitions</b>	<b>39</b>
4.1 A Formulation of Physics-Based Via Modeling Including Microstrip Tran- sitions	40
4.1.1 Determination of a Modeling Approach for Turning Vias	41
4.1.2 Analytical Formulation for Microstrip Ports Description	44
<b>5 Analysis of Mode Conversion Due to Asymmetrical Via Stubs</b>	<b>55</b>
5.1 Investigation of Mode Conversion Due to Asymmetrical Via Stubs	56
5.2 Estimation of Mode Conversion as a Function of Via Stub Mismatches	59

**6 Conclusions and Outlook****63****Bibliography****65**

# List of Figures

1.1	Description of the physics-based via model for a single via, (a) a via crossing two adjacent metal planes with the consequent electromagnetic fields interaction, (b) and equivalent $\pi$ -network representation of a cavity [1]. . . . .	2
1.2	Physics-based via modeling approaches (a) methodology proposed in [2] based on an electromagnetic analysis of the coaxial/radial line junction, (b) and intrinsic circuit via modeling based on via and plate domains analysis, presented in [3]. . . . .	3
2.1	Description of the physics-based via modeling for a single via in a multilayer substrate [1]. The extracted model is concatenated by using segmentation techniques, in order to obtain the response of the entire stackup structure.	5
2.2	Cavity segment to describe the via-to-plane capacitances. The via top segment presents as reference, the capacitances used for the $\pi$ -network modeling [1]. . . . .	9
2.3	Approach developed by Williamson for a cross-coupled junction. Dashed line refers to the calculation of the near-field interaction, which is more detailed than $\pi$ -network modeling. This approach has shown very accurate agreement compared to full-wave methods [2], [4]. . . . .	10
2.4	Intrinsic via modeling developed by Zhang in [3]. This approach is based on an electromagnetic analysis of the via and plane domains with their corresponding boundary conditions. Dashed lines represent the modeling for the via near-field propagation. . . . .	12
2.5	Different via-to-plane connectivity configurations. The connection or short circuit between the via and the plane results in a non-effect of the near-field interaction in the specific via segment, i.e. upper and lower [1]. . . . .	14
2.6	Electromagnetic modes presented in a cavity, as pointed in [5]. The transmission line and parallel-plate modes are coupled in case of a stripline trace routed into the cavity, and can be computed separately by using modal decomposition. . . . .	15
2.7	Stripline port definition for a trace embedded in a cavity. $I_2^s$ and $V_2^s$ are the electrical parameters that describe the stripline port, decoupled from the parallel-mode that co-exist into the cavity. . . . .	15

2.8	Turning via representation in top and side views. Quasi-TEM modes are propagated through the microstrip trace due to the difference of dielectrics. These modes arrive to the turning via and excite high-order modes in around the antipad geometrical sections, depicted with the dashed lines. . .	17
2.9	Microstrip line topology under analysis, where the characteristic impedance is a function of the geometrical parameters shown here. Besides, the frequency dependence is defined the propagation constant, and appears by the effect of the dielectric and conductor losses. . . . .	18
2.10	Via barrel crossing a metal plane, formulated in [6]. In this case, fringing capacitances between the via and plane can be calculated by using an integral equation. The calculation is defined by assuming axially symmetry around the via barrel. . . . .	20
2.11	Upper segment configuration that represents the fringing fields lines between the pad and the metal plane. . . . .	23
3.1	Top view of the structure under analysis for regular cases. As depicted, a signal via is surrounded by two ground vias to improve the return path performance, and coaxial ports are placed at the top and bottom of the each stackup. . . . .	26
3.2	Side view for the simulated structures, i.e (a) 11-cavities, (b) 5-cavities, and (c) 1-cavity stackups. All the configurations present coaxial ports of 20 mil of length, which have been dismissed by using de-embedding techniques. .	27
3.3	Scattering parameters for the 11-cavities model. Left graph refers to the transmission coefficient, similarly the right one represents the reflection parameter. The $\pi$ -network model presents an important deviation from the FEM solutions around 20 GHz and beyond. . . . .	27
3.4	Scattering parameters for the 5-cavities model. Same as 11-cavities case response, the $\pi$ -network model presents an important deviation from the FEM results in around 20 GHz, which is more denoted in the insertion losses parameter. . . . .	28
3.5	Scattering parameters for the 1-cavity model. Similar as the other regular cases, the $\pi$ -network model presents itself a lesser accuracy than Williamson approach for high-frequency ranges. For short vias, this effect is more pronounced in the $\pi$ -network model, as denoted in [1]. . . . .	28
3.6	Configuration that contains microstrip-to-via transitions. These transition structures are commonly present in break-out/in sections, e.g. memory interfaces. The analysis of the structure by using FEM allows the visualization of the turning via effects represented by using scattering parameters.	29
3.7	Comparison between full-wave results of the complete topology, shown in the Figure 3.6, and the scattering parameters by including only the pair of microstrip transmission lines and the cavity section. The effect of the turning vias is reflected mostly for frequencies beyond 8 GHz. . . . .	30

3.8	Phase constant for different configurations of Figure 3.6 (a) with no pad, and (b) including a 10 mil pads at top/bottom segments. High-order modes are present in relative high frequencies, where the 1 <sup>st</sup> one appears up to around 40 GHz. The effect of the pad can be neglected during the analysis of propagation of the high-order modes. . . . .	31
3.9	The (a) microstrip-via-microstrip configuration and (b) the equivalent $T$ -network representation. Each single turning via is represented by a inductance $L_t$ and a capacitance, defined as $C_t/2$ . . . . .	32
3.10	Segmented model including the turning vias for top and bottom at the stackup under analysis. This representation is based on the $T$ -network proposed in [7]. . . . .	32
3.11	Scattering parameters comparison between the structure shown in the Figure 3.6 and the segmented topology in Figure 3.10, which includes the modeling for the turning vias. There seems acceptable agreement between models for relatively low and high-frequency ranges. . . . .	33
3.12	Additional configuration that contains microstrip-to-via transitions. The cavity model includes the effect of the far and near-field interaction, as well as the scattering among vias. External structure includes a 200 mil microstrip trace connected in both sides by a turning via. . . . .	34
3.13	Scattering parameter of the structure shown in Figure 3.12. Main deviations are presented in high frequencies, where the frequency-dependence effects of lumped element appear and affect the model accuracy. . . . .	34
3.14	Phase constant $\beta$ for the configuration in Figure 3.12. Parasitic modes are highly attenuated due the the excitations of coaxial ports, where these modes tend to appear around 300 GHz for regular cases, according to [8]. . . . .	35
3.15	Different configurations to analyze the effect of parasitic modes propagation due to turning vias (a) 5-cavities stackup, and (b) microstrip-to-stripline transition. It has been shown the effect of these transitions in terms of the propagation of high-order modes, e.g. Figure 3.8. . . . .	35
3.16	Frequency response of the topology depicted in Figure 3.15 (a), where in (a) is shown the scattering parameters for insertion and return losses, and (b) presents the response of the propagated modes. Comparing with Figure 3.8, there is no evidence of the influence for parasitic modes due to higher number of cavities. It is expected due to the assumption of physics-based modeling that only fundamental mode propagates across these structures. . . . .	36
3.17	Response of (a) scattering parameters - return and insertion losses, and (b) propagated modes of the in Figure 3.15 (b). As same case as Figure 3.16, there is no influence of stripline transition for a matched stripline trace. . . . .	36
3.18	Propagated modes in a stripline-to-stripline transition for (a) matched and (b) mismatched striplines. By considering an impedance mismatch in the striplines traces can lead to a decreasing of the cut-off frequencies of high-order modes. The mismatched stripline case presents a characteristic impedance of around 31 Ohm. . . . .	37

3.19	Comparison of scattering parameters for different modeling approaches of the structure shown in Figure 3.6, where all the cases presents acceptable agreement compared to the baseline case (FEM) for all the approaches. However, in case of return losses, a segmented modeling by considering a LC network for turning vias, reflects a better agreement compared with the FEM method. . . . .	37
3.20	Phase parameter for same cases presented in Figure 3.19. In case of the phase response, as same as the scattering parameters, a modeling approach based on a LC networks is more suitable to represent the turning vias. . .	38
4.1	Configuration under analysis for the inclusion of microstrip ports in physics-based modeling. The topology includes the turning vias and microstrip traces, which are the external agents from the regular cavity modeling. . .	40
4.2	Modeling approaches for turning vias based on a via crossing a metal plane, by considering: (a) upper and lower sides, and (b) only one of the segments of the turning via, as shown in [7], where $L_1 = L_2 = L_t$ and $C_t = C/2$ . . . .	42
4.3	Frequency response of the Z-parameters of the network shown in Figure 4.2 (b) for $C_t = 53.4$ fF and $L_t = 133.5$ pH. The LC network influence is mostly given by the imaginary part of each matrix entity, and defines the behavior of the modeling stage. . . . .	43
4.4	Representation of the case under analysis, including the electrical parameters for each agent in <i>external</i> and <i>internal</i> sections. The analysis covers all the structure parameters, but constraints are applied in order to reduce the case of study for the electrical description of microstrip ports. . . . .	45
4.5	Upper segment of the case under study. The current coming from the microstrip trace is divided in the upper and lower cavity currents. This KCL analysis allows to correlate directly electrical parameters between exterior and internal sections. . . . .	46
4.6	Segmented modeling proposed in [1] for a general stackup configuration shown in (a). The <i>external</i> section is a contribution of the turning via and the microstrip line depicted in the Microstrip Transition Layer, which formulates the $\mathbf{Y}^{ext}$ parameter. (b) By using segmentation techniques [9], the entire effect is obtained and described as a single matrix, by including the all effects into the cavities, such as a via short-circuited to metal planes, transmission lines, stripline ports, etc. . . . .	48
4.7	Different stackup structures for the modeling approach validations. Each one has the difference in the number of cavities that is the stackup composed: (a) 1-cavity stackup, (b) 3-cavities stackup, and (c) 5-cavities stackup. Similar as the configuration shown in Figure 3.6, ground vias distance are 40 mil. . . . .	49
4.8	Scattering parameters for the 1-cavity stackup shown in Figure 4.7 (a). It is depicted the response for (a) insertion and (b) return losses. A good agreement is achieved up to around 12 GHz. . . . .	50

4.9	Phase parameters for the 1-cavity stackup shown in Figure 4.7 (a). The responses are for (a) insertion and (b) return losses, where the agreement in terms of frequency ranges is quite similar compared to the scattering parameters. . . . .	50
4.10	Scattering parameters for the 3-cavities stackup shown in Figure 4.7 (b). It is depicted the response for (a) insertion and (b) return losses. The agreement of this case seems to be some worst compared to 1-cavity and 5-cavities stackup. . . . .	51
4.11	Phase parameters for the 3-cavities stackup shown in Figure 4.7 (b). The response for (a) insertion and (b) return losses is presented. . . . .	51
4.12	Scattering parameters for the 5-cavities stackup shown in Figure 4.7 (c). It is depicted the response for (a) insertion and (b) return losses. Similarly as the case of 1-cavity stackup, a good agreement is achieved up to around 12 GHz. . . . .	52
4.13	Phase parameters for the 5-cavities stackup shown in Figure 4.7 (c). It is shown the parameters for (a) insertion and (b) return losses. As similar to the scattering parameters, a good agreement is achieved up to around 12 GHz. . . . .	52
4.14	Scattering parameters for the 5-cavities stackup shown in Figure 4.7 (c) and the ground via distance of 30 mil. The (a) insertion and (b) return losses are shown, and the agreement even up to 15 GHz by improving the return path performance. . . . .	53
4.15	Scattering parameters for the 5-cavities stackup shown in Figure 4.7 (c) and the ground via distance of 50 mil. Difference at the case of 30 mil distance, the accuracy is reduced even for frequencies below to 10 GHz. . .	53
5.1	Asymmetrical via stubs in a differential pair - cross sectional view. The difference $\Delta l_{stub}$ deals with differential to common-mode conversion. Differences in range of back-drilling tolerances can generates important amounts of this losses. . . . .	56
5.2	Differential via-to-via configuration: (a) top and, (b) side view. Differential stripline traces are routed on cavity 2 and via stub length on port 01 (-) has been varied to analyze the effect on mode conversion. . . . .	57
5.3	Skew effect observed at the Port 02 (+/-) in the differential pair for symmetrical and asymmetrical via stub cases (a) timing and stub effect for step responses, and (b) common-mode signals for each case, respectively. Generator and termination impedances are 50 Ohm. . . . .	57
5.4	Via stub effect in (a) differential transmissions, and (b) far-end mode conversion for reference cases including symmetric and asymmetric configurations. The mode conversion magnitude has a direct relation with the differential via asymmetry. Simulations performed with FIT method [10], considering a reference impedance of 50 Ohm. . . . .	58

5.5	Magnitude of far-end mode conversion for different via stub asymmetries. In (a), it is depicted the effect of asymmetries in the order of back-drilling residual tolerances, and in (b) the magnitude across fundamental frequencies and via stub asymmetries as well. . . . .	59
5.6	Asymmetric differential via-to-via link under analysis: electrical description of the stub effect in a differential pair. Skew exists between the signal (-) and signal (+) due to part of the signal propagating through the via stub and then being reflected (the red signal) . . . . .	60
5.7	Estimation of the far-end mode conversion magnitude (a) modeling approximation based on a first order low-pass filter and (b) frequency response as a function of the length stub difference. This approximation is based on low frequency response of the $\Delta l_{stub}$ in the differential configuration. . . . .	60

# List of Tables

5.1	Magnitude of far-end mode conversion for different via stub asymmetries. .	61
-----	--	----



# Chapter 1

## Introduction

### 1.1 Motivation and Context

Modern digital systems feature a high number of interconnects, over tenths of thousands in a custom printed circuit board (PCB). The increment of data transfer rates, smaller form factors, different types of agents as well as levels of integration have made the process of pre-layout design an essential stage for modern implementations. In this way, high-speed interfaces are reaching data rates up to several GHz [11], and at the same time, electromagnetic effects appear that degrade the transmitted signal integrity [12]. Power delivery issues must be considered as the data rate increases as well. Off-chip interconnects, due to their inherent low-pass behavior, have been the bottleneck on the bandwidth that can be achieved in high-speed interfaces. For these reasons, the design and validation of electrical links and their performance are one of the most relevant stages in modern systems and developments [13].

However, in order to design an electrical link, several aspects need to be considered. In the case of the communication channel, efficient modeling allows a more optimal design process, superlatively, in terms of computing time. This is a challenging stage because of the huge number of interconnects presented in modern system developments in the industry. Thus, different methodologies have been explored and developed for accurate models that result on more efficient simulations. For instance, physics-based modeling has shown higher efficiency in terms of computing time than regular full-wave methods. There exist plenty of research on this approach. As an example, Figure 1.1 (a) depicts the basic cell of the current physics-based via modeling [1], where the dashed blue lines represent the regions where some mode conversions occur on. The basic cavity cell is composed by the interaction of a coaxial and radial waveguides, which defines the propagated modes inside the structure.

It is well known that parallel-plate modes are excited into the cavity, and can propagate due to the return current on metal planes. This far-field interaction is described by the calculus of the parallel-plate impedance  $\mathbf{Z}^{pp}$ , which defines the return current path on

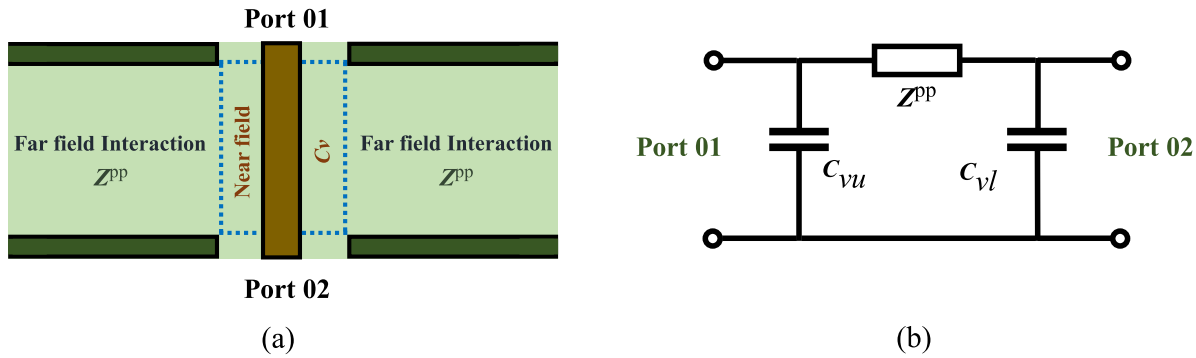


**Figure 1.1:** Description of the physics-based via model for a single via, (a) a via crossing two adjacent metal planes with the consequent electromagnetic fields interaction, (b) and equivalent  $\pi$ -network representation of a cavity [1].

the structure [14]. Also, the near-field interaction refers to the high-order modes excited nearby to the via barrel, which are rapidly attenuated. These interactions are described by including the coaxial and via-to-plane capacitances  $C_v$  as a first approach. The basic model representation is depicted in the Figure 1.1 (b). As mentioned, there exist several research regarding physics-based via (PBV) modeling. For instance, in [15] it is presented a semi-analytical model for the case shown in Figure 1.1 (a). Moreover, the analysis covers various types of vias, i.e. thru-hole, buried, blind, etc. This approach has been validated up to 40 GHz under several simulation scenarios. However, the calculations of the near fields around the via barrel have shown limitations for certain geometries and high-frequency ranges. By addressing this fact, there have been developed other approaches for the modeling of this section, as mentioned in [16]. These approaches are based on an electromagnetic analysis of the coaxial and radial waveguides junction [2] and an intrinsic via circuit model by defining a via and plate localized domains [3]. As depicted in Figure 1.2, both approaches are described in terms of equivalent electrical circuits, which allows that the computing time of the calculus would be faster than regular full-wave methods.

This thesis is a contribution to extend the state of the art in terms of the modeling and understanding of the interconnect behavior at high-frequencies, specifically for the generalization of the physics-based ports descriptions and a better understanding of their limitations. The aim pursued is the development and validation of an extension of the current physics-based via modeling, by improving the current description with the inclusion of microstrip ports as well as the transitions between microstrip and vias in multilayer substrates, which are commonly identified as turning vias.

Additionally, the evaluation of an effect that cannot be modelled with the physics-based approach is discussed, namely, the asymmetries in differential signaling and the effect on mode conversion, specifically for via stubs is analyzed. The impact of asymmetries in via stubs for differential connections is discussed, where it is shown that the effect could become important depending on the length of the stub and level of asymmetry.

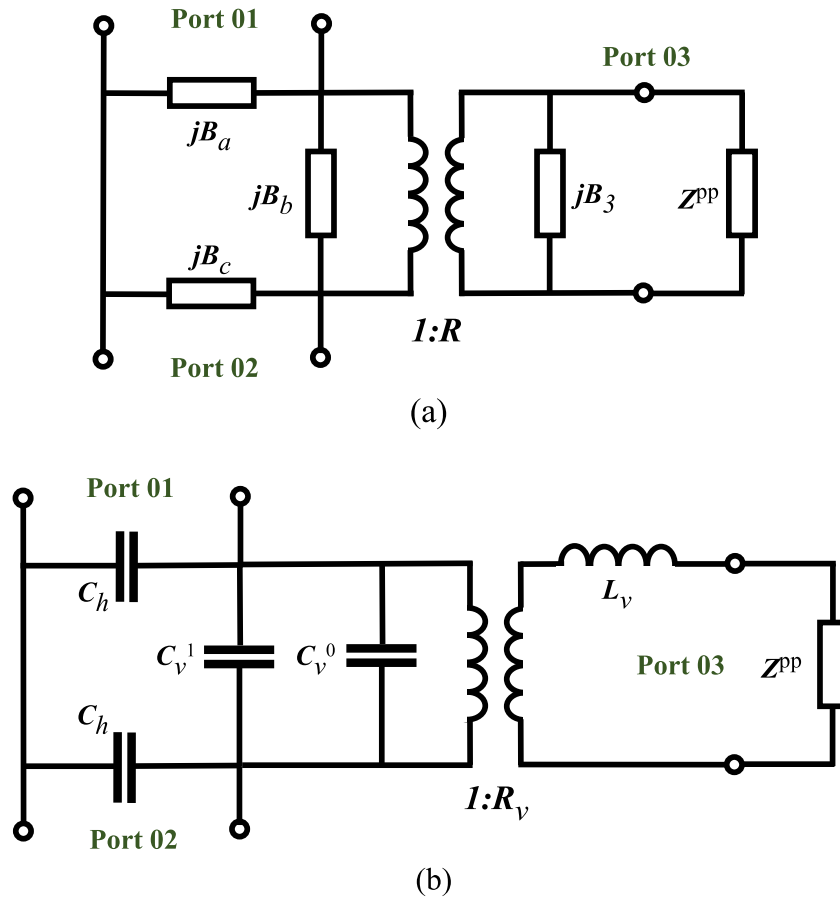


**Figure 1.2:** Physics-based via modeling approaches (a) methodology proposed in [2] based on an electromagnetic analysis of the coaxial/radial line junction, (b) and intrinsic circuit via modeling based on via and plate domains analysis, presented in [3].

## 1.2 Objectives

This work is focused on the extension of the current physics-based via modeling and exploring the limitations and importance of non-regular cases that escape to this type of modeling, by improving the description of irregular cases with the inclusion of microstrip ports and a proposal for modeling the transitions between microstrip transmission lines and vertical interconnects, identified as turning vias, as well as the effect of the asymmetric via stubs in differential signaling.

In order to achieve this, it was necessary to determine the behavior of electromagnetic modes for the topologies to analyze through full-wave simulations. Additionally, the analysis and development of a scheme of modeling for the selected topologies considering geometric and material properties of these configurations. The intention of the proposed modeling is to be based on an equivalent electrical circuit, that allows more efficient simulations. Then, the validation of the proposed modeling against full-wave simulations is the last section of this analysis, where a comparison of the agreement among them would determine the viability and accuracy of the proposal with the aim to explore the

limits of the physics-based modeling approaches. Also, this thesis also explores a case not reported previously in the literature: the effect of asymmetric via stubs in differential signaling, where it is presented the effect of the back-drilling process on the electrical link performance.

## 1.3 Organization

The core of this thesis is based on six chapters, where each one of these are briefly discussed as follows:

**Chapter 2:** presents a bibliographic review about updated topics related the physics-based via modeling. Also, this review covers topologies where high-order modes are present and configurations that are not already modeled.

**Chapter 3:** deals with an analysis of regular configurations where the physics-based via modeling has good agreement compared to full-wave methods. Moreover, cases that are not covered in the current modeling approach introduce the aim of this thesis.

**Chapter 4:** explains the modeling approach for the cases proposed in this work, based on theoretical concepts introduced as references. Also, deals with the validation of the proposed model. Here, the examples used to simulate and compare with the full-wave data reference are presented.

**Chapter 5:** deals with an analysis and estimation of the amount of mode conversion because of asymmetrical via stubs in differential signaling. This is caused by the residual via stubs present during back-drilling processes.

**Chapter 6:** covers the conclusions and further work based on discussed results.

# Chapter 2

## Segmented Physics-Based Via Modeling of Multilayer Substrates

Physics-based modeling has been mightily investigated and validated in the literature, e.g. [14], [17], [18]. By definition, the formulation of the via modeling considers that the via interconnection is crossing a cavity enclosed by two parallel metal planes [15]. Figure 2.1 depicts the description of the via model.

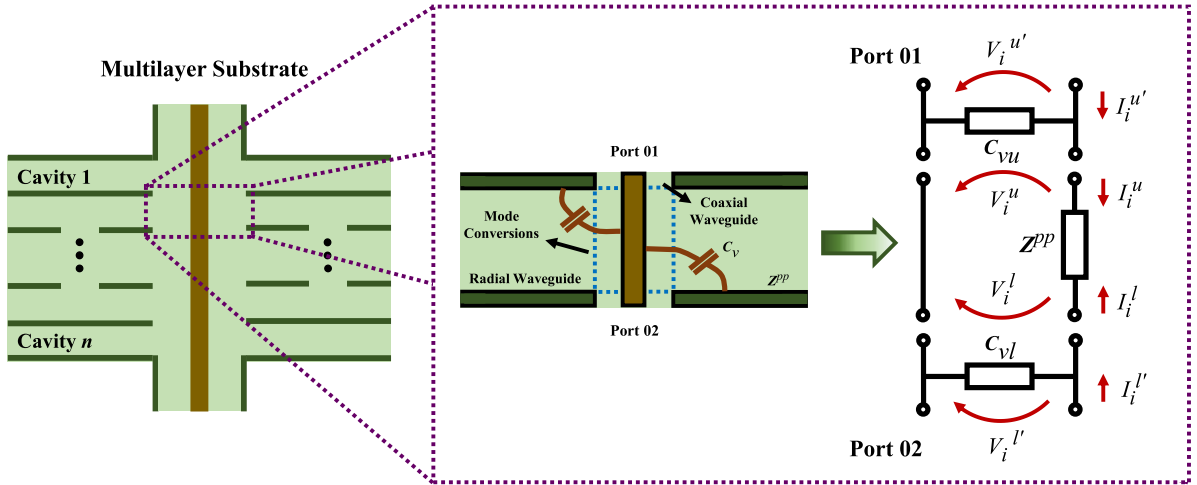


**Figure 2.1:** Description of the physics-based via modeling for a single via in a multilayer substrate [1]. The extracted model is concatenated by using segmentation techniques, in order to obtain the response of the entire stackup structure.

The representation in the Figure 2.1 [1] is a  $\pi$ -network composed by various elements. Specifically, there exist two elements that describe the far and near-field interactions in a via interconnection. For the near-field case, via-to-plane capacitances are proposed to describe the fringing fields section around the via, i.e. antipad section. The parallel-plate impedance  $Z^{pp}$  represents the far-field interaction of the reference planes in terms of electromagnetic modes that can propagate into the cavity. Hence, regarding the parallel-plate impedance, the  $Z^{pp}$  can be interpreted as the impedance seen by the via barrel, between

the reference planes. Thus, this impedance can be used to construct the expression:

$$\bar{V}_i = \mathbf{Z}^{pp} \cdot \bar{I}_i \quad (2.1)$$

According to (2.1), the voltages and currents represent the parameters defined into each cavity segment, which are directly related to the return path impedance between parallel metal planes [15].

## 2.1 Review of Physics-Based Via Modeling Formulation

It has been stated that the formulation of the physics-based via modeling is referred to include interactions about far and near-fields. Thus, the following subsections show a brief discussion of the developed methods for each one of these interactions.

### 2.1.1 Far-field Interaction Modeling

Several investigations have shown that parallel-plate modes can propagate between the reference metal planes. In this lane, the definition of a parallel-plate impedance  $\mathbf{Z}^{pp}$  to model the physical effect of far-field propagation has been successfully validated in real case scenarios. These electromagnetic modes are excited when a current flows out through a via barrel, and according to the theory, there exist a magnetic field wave who propagates with cylindrical symmetry into the cavity, in case of ideal conditions. This magnetic field excites the parallel-plate modes, and these waves can manifest themselves as voltage fluctuations between the metal planes, which might be identified as PDN noise. Among the developed approaches to calculate the parallel-plate impedance, it is possible to mention the contour integral method (CIM), the cavity resonator model (CRM), and the radial waveguide method (RWM), as an examples.

In case of CIM, the formulation of this approach allows to handle irregular plane shapes. Since the distance between planes is smaller than the wavelength of interest, the formulation is reduced as 2D approximation that yields to a decreasing of computing effort [19]. Furthermore, alternatives of this approach have been developed considering circular ports with isotropic [20] and anisotropic [21] excitations. By considering the formulation in [19], the parallel-plate impedance  $\mathbf{Z}^{pp}$  can be calculated as follows:

$$\mathbf{Z}^{pp} = \mathbf{U}^{-1} \mathbf{H} \quad (2.2)$$

The matrices  $\mathbf{U}$  and  $\mathbf{H}$  are used to calculate the impedances and are defined as [4]:

$$U_{ij} = \frac{k\pi r_{v,j}}{j} \cdot \begin{cases} J_0(kr_{v,i})J_1(kr_{v,j})H_0^{(2)}(kr_{ij}), & (i \neq j) \\ J_0(kr_{v,i})H_1^{(2)}(kr_{v,i}), & (i = j) \end{cases} \quad (2.3)$$

and

$$H_{ij} = \frac{k\eta h}{2} \cdot \begin{cases} J_0(kr_{v,i})J_1(kr_{v,j})H_0^{(2)}(kr_{ij}), & (i \neq j) \\ J_0(kr_{v,i})H_0^{(2)}(kr_{v,i}), & (i = j) \end{cases} \quad (2.4)$$

where  $J_0$  and  $J_1$  are the zero-order and first-order Bessel functions respectively,  $H_0^{(2)}$  and  $H_1^{(2)}$  the zero-order and first-order Hankel functions of second kind. Also,  $\eta = \sqrt{\mu/\epsilon}$  is the wave impedance and  $r_v$  is the radius of the via  $i$ , as well as  $r_{ij}$  is the center-to-center vias separation. As pointed out in [4], the CIM considers the influence of the backscattering from other vias around, which leads to a more accurate calculations.

Regarding the CRM approach, the principle of the small separation between the metal planes is still valid and given the boundary conditions, the parallel-plate impedance can be described using the 2D Helmholtz equation [1]. For rectangular planes, it can be expressed as follows:

$$Z_{ij}^{CRM}(\omega) = \frac{j\omega\mu d}{ab} \sum_{m=0}^{\infty} \sum_{n=0}^{\infty} c_m^2 c_n^2 \frac{f_{B.C.} \cdot f_P}{k_m^2 + k_n^2 - \underline{k}^2} \quad (2.5)$$

being  $c_m, c_n = 1$  for  $m, n = 1$ , and  $c_m, c_n = \sqrt{2}$  for  $m, n \neq 1$ ,  $k_m = m\pi/a$ , and  $k_n = n\pi/b$ . Also,  $f_P$  is expressed as a function of the side length of the ports, i.e. finite port sizes and it can be expressed:

$$f_P = \text{sinc}\left(\frac{k_m W_{xi}}{2}\right) \cdot \text{sinc}\left(\frac{k_n W_{yi}}{2}\right) \cdot \text{sinc}\left(\frac{k_m W_{xj}}{2}\right) \cdot \text{sinc}\left(\frac{k_n W_{yj}}{2}\right) \quad (2.6)$$

where the size of the rectangular ports are varied in order to match with the circular via perimeter,  $W_{xi} = W_{yi} = \pi \cdot r_i^v/2$  and  $r_i^v$  represents the  $i$ th via radius. The function  $f_{B.C.}$  can be defined as follows, by applying a PMC boundary conditions at the edges to approximate an open boundary:

$$f_{B.C.} = \cos(k_m x_i) \cdot \cos(k_n y_i) \cdot \cos(k_m x_j) \cdot \cos(k_n y_j) \quad (2.7)$$

Besides, for PEC boundary conditions, the function  $f_{B.C.}$  can be expressed by defining a short circuit at the edges, as following:

$$f_{B.C.} = \sin(k_m x_i) \cdot \sin(k_n y_i) \cdot \sin(k_m x_j) \cdot \sin(k_n y_j) \quad (2.8)$$

Additionally, the wave number can be defined as:

$$\underline{k} = \omega \sqrt{\mu_d \epsilon_d} \cdot \left( 1 - j \left[ \frac{(\tan \delta + d_s/d)}{2} \right] \right) \quad (2.9)$$

where  $\tan \delta$  is the dielectric loss and  $d_s = \sqrt{2/\omega \mu_c \sigma_c}$  is the electric conductor loss. It is important to highlight that the port definitions play a relevant role when the physical dimensions and frequency range increases [22], [1].

In [23], it is explained the RWM, which is a method used considering infinite planes. This means that there are no reflections from the edges of the board, and in order to consider finite planes, the formulation can be extended by using image theory. More details about this can be found in [1]. As mentioned in [23], the parallel-plate impedance  $\mathbf{Z}^{pp}$  can be expressed as follows:

$$Z_{ij}^{RWM}(\omega) = \frac{j\eta d}{2\pi\rho_0 H_1^{(2)}(k\rho_0)} \cdot H_0^{(2)}(k\rho_{ij}) \quad (2.10)$$

where  $H_0^{(2)}$  and  $H_1^{(2)}$  the zero-order and first-order Hankel functions of second kind,  $\rho_{ij}$  is the distance between the ports and  $\eta = \sqrt{\mu/\epsilon}$ . The assumption of the small distance between the planes is still valid here, which reduces significantly the analysis and calculations to a 2D approximation as well.

### 2.1.2 Description of the Near-field Modeling

For the local fields around the via barrel, the presence of electromagnetic modes are not restricted to fundamental ones. It has been recognized that high-order modes can propagate at the antipad section, but they are strongly attenuated for not-shared antipads [15]. Under this fact, this non-homogeneous field section can be approximated in a simplistic way by a capacitance value. These ones can represent also, the displacement current presented between the via barrel and the reference planes.

As the Figure 2.2 depicts, this via-to-plane capacitance can be separated by three contributions. The  $C_c$  represents the coaxial capacitance between the via barrel and the reference plane,  $C_b$  is the lateral capacitance between the plane side and the via, and  $C_f$  are the fringing capacitances at the up/bottom planes and the via barrel [1]. Thus, the capacitance of a via in a cavity can be calculated as follows:

$$C_v = C_c + C_b + C_f \quad (2.11)$$

For the calculation of these capacitances, [8] proposes an analytical expressions that have been employed and validated in the several works. For the coaxial capacitance  $C_c$ , it is well known that can be described as:

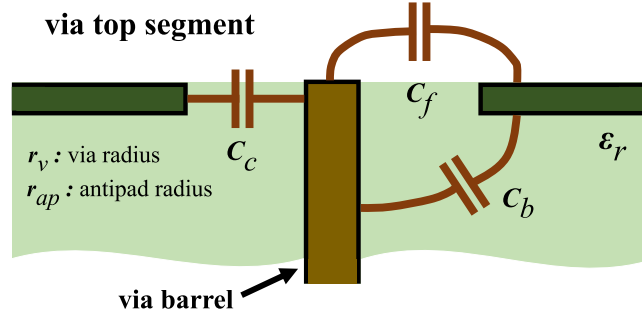


**Figure 2.2:** Cavity segment to describe the via-to-plane capacitances. The via top segment presents as reference, the capacitances used for the  $\pi$ -network modeling [1].

$$C_c = \frac{2\pi\epsilon_r\epsilon_0 t}{\ln(r_{ap}/r_v)} \quad (2.12)$$

with  $r_v$  and  $r_{ap}$  the via radius and antipad radius, respectively, and  $t$  is the plane thickness. Similarly, in case of the capacitance between the via barrel and the plane, i.e.  $C_b$ , in [8] can be also found an expression based on an analytical approach, which is defined:

$$C_b = \frac{8\pi\epsilon_r\epsilon_0}{h \cdot \ln(r_{ap}/r_v)} \sum_{n=1,3,5}^{2N-1} \frac{1}{k_n^2 H_0^{(2)}(k_n r_v)} \cdot \left\{ [H_0^{(2)}(k_n r_{ap}) - H_0^{(2)}(k_n r_v)] \right\} \quad (2.13)$$

being  $h$  the dielectric cavity thickness,  $k_n = \pm\sqrt{\omega^2\mu_h\epsilon_h - (n\pi/d)^2}$ , and  $H_0^{(2)}$  the zero-order Hankel function of second kind. For reference, typical values for via capacitances per cavity are in between 20 fF and 100 fF [1]. These approaches are defined by considering fundamental TEM modes as excitations. This assumption is valid due to, according to [8], in coaxial lines the high-order modes attend to appear in frequencies far away to the frequency range of interest, i.e. up to 40 GHz. Recently, other approximations have been developed in order to increase the calculation efficiency of these capacitance, e.g. in [24], [25]. On the other hand, the fringing field capacitances calculation take a different analysis. For instance, in [26] it is presented a method for the calculation of the external capacitances, based on an integral equation of the surface charge density in axially symmetric configurations.

Thus, by considering the far and near-field interactions described before, the cavity formulation for a via  $i$  can be expressed as follows [15]:

$$\begin{bmatrix} I_i^{u'} \\ I_i^{l'} \end{bmatrix} = \begin{bmatrix} Y^{cav} & -Y^{cav} \\ -Y^{cav} & Y^{cav} \end{bmatrix} \cdot \begin{bmatrix} V_i^{u'} \\ V_i^{l'} \end{bmatrix} \quad (2.14)$$

where the  $\mathbf{Y}^{cav}$  is defined as:

$$\begin{bmatrix} Y^{cav} & -Y^{cav} \\ -Y^{cav} & Y^{cav} \end{bmatrix} = \begin{bmatrix} Y^{cu} & 0 \\ 0 & Y^{cl} \end{bmatrix} + \begin{bmatrix} Y^{pp} & -Y^{pp} \\ -Y^{pp} & Y^{pp} \end{bmatrix} \quad (2.15)$$

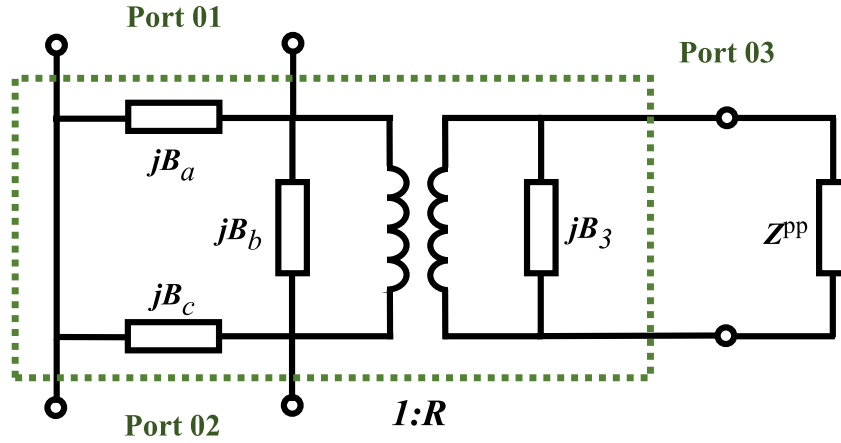


**Figure 2.3:** Approach developed by Williamson for a cross-coupled junction. Dashed line refers to the calculation of the near-field interaction, which is more detailed than  $\pi$ -network modeling. This approach has shown very accurate agreement compared to full-wave methods [2], [4].

with  $\mathbf{Y}^{pp} = \mathbf{Z}^{pp-1}$  and  $Y^c = j\omega C_v$ . Although this approach has shown good agreement and high efficiency compared to full-wave methods, for high frequencies presents a considerable deviation from the baseline cases. In this way, in [3] it is suggested that this approach is valid as intuitively method for low frequencies so, it can estimate the via capacitance with accurate results in a relative low frequency range, as presented in [4]. As the Figure 1.2 depicts, there exist another approaches for the via modeling, by considering a physics-based analysis and defining an equivalent circuit model. For instance, Williamson approach is presented in [2] and offers an analysis of the coaxial/radial lines, extended for a cross-coupled junction. Figure 2.3 depicts the equivalent circuit about this approach.

The Williamson method is based on the electromagnetic analysis of the junction of two different waveguides, which are coaxial and radial lines, by using a TEM approximation and assuming again that, high-order modes are rapidly attenuated in the antipad geometrical section. According to the Figure 2.3, the modeling parameters can be calculated as follows:

$$B_{11} = -\frac{2\pi}{\eta_0 \ln(r_{ap}/r_v)} \coth(kh) + 2 \sum_{m=1}^{\infty} D_m^c \quad (2.16)$$

$$B_{21} = -\frac{2\pi}{\eta_0 \ln(r_{ap}/r_v)} \frac{1}{\sin kh} + 2 \sum_{m=1}^{\infty} (-1)^m D_m^c \quad (2.17)$$

$$R = \frac{(2/\pi) \ln(r_{ap}/r_v)}{J_0(kr_v)Y_0(kr_{ap}) - J_0(kr_{ap})Y_0(kr_v)} \quad (2.18)$$

$$D_m^c = \frac{2\pi}{\eta_0 kh \ln^2(r_{ap}/r_v)} \frac{1}{q_m^2} \frac{K_0(q_m k r_{ap})}{K_0(q_m k r_v)} \left[ I_0(q_m k r_v) K_0(q_m k r_{ap}) - I_0(q_m k r_{ap}) K_0(q_m k r_v) \right] \quad (2.19)$$

where,

$$B_a = B_c = B_{11} - B_{21}, \quad B_b = B_{21} \quad (2.20)$$

$$B_3 = \frac{2\pi r_v}{\eta_0 h} \cdot \frac{J_1(kr_v)Y_0(kr_{ap}) - J_0(kr_{ap})Y_1(kr_v)}{J_0(kr_v)Y_0(kr_{ap}) - J_0(kr_{ap})Y_0(kr_v)} \quad (2.21)$$

In order to get more details related to the calculations and model parameters, [2] presents a deeper analysis and reference. Therefore, for this approach, the via model, by including the parallel-plate effects, is formulated similarly as (2.15), which is [4]:

$$\mathbf{Y}^{cav} = \begin{cases} jB_a + jB_b + \frac{1}{R_i R_j} (jB_3 + Y_{ij}^{cav}), & (i = j) \\ jB_b + \frac{1}{R_i R_j} (jB_3 + Y_{ij}^{cav}), & (i = j + N \text{ or } i + N = j) \\ \frac{1}{R_i R_j} Y_{ij}^{cav}, & (else) \end{cases} \quad (2.22)$$

where  $N$  is the number of vias. The Williamson approach has shown very good results in terms of accuracy at high frequencies, mostly because of the more detailed calculation of the near-field effects. Furthermore, a very similar results have been obtained by Zhang in [3]. This another approach is based on the definition of a domains for the via and the plane, and construct the analysis with a given boundary conditions. The equivalent circuit is quite similar as Williamson approach, with the difference of the presence of the inductance in series to the parallel-plate impedance. Figure 2.4 shows the equivalent circuit for the Zhang approach, identified as intrinsic via modeling.

The expressions to calculate the model parameters are defined as follows [3]:

$$C_h = \frac{j2\pi r_v}{h} \frac{2\epsilon_r \epsilon_0 \pi}{\ln(r_{ap}/r_v)} \sum_{n=1,3,5,\dots}^{2N-1} F_n^S(r_v) \quad (2.23)$$

$$C_v^1 = \frac{j\pi r_v}{h} \frac{2\epsilon_r \epsilon_0 \pi}{\ln(r_{ap}/r_v)} \sum_{n=1,3,5,\dots}^{2N-1} (-1)^n F_n^S(r_v) \quad (2.24)$$

For the cases where the boundary conditions are defined as PML (infinite planes),  $S = L$  is valid and the function  $F_n^S$  can be re-defined as [3]:

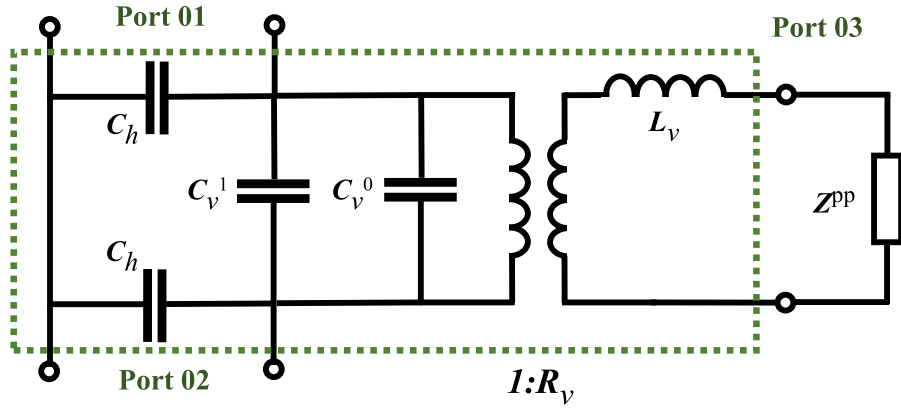


**Figure 2.4:** Intrinsic via modeling developed by Zhang in [3]. This approach is based on an electromagnetic analysis of the via and plane domains with their corresponding boundary conditions. Dashed lines represent the modeling for the via near-field propagation.

$$F_n^L(r_v) = \frac{H_0^{(2)}(k_n r_{ap}) - H_0^{(2)}(k_n r_v)}{k_n(1 + \delta_{n0})H_0^{(2)}(k_n r)} W_{10}(k_n r_v, k_n r) \quad (2.25)$$

where  $\delta_{n0}$  is the Kronecker delta function and  $W_{mn}(x, y)$  is an auxiliary function expressed by  $m$ -th Bessel and  $n$ -th second-order Hankel functions, given by:

$$W_{mn}(x, y) = \begin{bmatrix} J_m(x) & J_n(y) \\ H_m^{(2)}(x) & H_n^{(2)}(y) \end{bmatrix} \quad (2.26)$$

The another model parameters are defined as following:

$$L_v = -\frac{\mu h}{2\pi k b} \frac{W_{00}(kl, kr)}{W_{10}(kl, kr)} \quad (2.27)$$

$$C_v^0 = \frac{j\pi r_v W_{10}(kr_v, kr)}{2kh W_{10}(kl, kr)} \frac{2\epsilon_r \epsilon_0 \pi}{\ln(r_{ap}/r_v)} \left[ W_{10}(kl, kr_{ap}) - W_{10}(kl, kr_v) \right] \quad (2.28)$$

$$R_v = \sqrt{-R_m R_e} \quad (2.29)$$

where the parameters  $R_m$  and  $R_e$  are:

$$R_m = \frac{j\pi}{2 \ln(r_{ap}/r_v)} \frac{W_{10}(kl, kl)}{W_{10}(kl, kr)} \times \left[ W_{00}(kl, kr) - W_{00}(ka, kr) \right] \quad (2.30)$$

$$R_e = \frac{r_v}{l} \frac{W_{00}(kr_v, kr)}{W_{00}(kl, kr)} \quad (2.31)$$

### 2.1.3 Modeling Extension Including Power/Ground Vias and Stripline Traces

The literature refers to several studies related to the importance of power integrity issues in modern developments. The need to reduce the equivalent impedance of the power delivery network (PDN) has become relevant in high-frequency ranges, where the effects are more notable. Some techniques have been applied in order to compensate these issues, such as grounding, decoupling, etc [27]. In multilayer substrates, reference planes are connected to a defined voltage value that are generally the pull-up or pull-down references. The reference planes (power/ground) are part of the power delivery network of the system, and can be used for the placement of components of the PDN. This fact allows better localized voltage references for the agents involved on the system, increase the grounding in case of both planes connected to ground, and the decoupling for mixed-reference planes connection. Moreover, vias connected to reference planes are used as well, which allows the improvement of the return path, i.e. by reducing the  $\mathbf{Z}^{pp}$  impedance and the coupling between vias and planes [27]. Hence, in case of the physics-based modeling of power/ground vias, in [28] a formulation is proposed for vias connected to metal planes. Figure 2.5 depicts the interconnection cases for a single cavity structure. Following the convention shown in the Figure 2.1, the via barrel can be connected to both adjacent planes, connected to only one of those, and not connected at all. According to the via connection, the physics-based via model must be re-defined. These connections refer to a short circuit between the via and planes, which electrically means that the effects of the near-field are cancelled out and the resulted effect of the via is referred only to the far-field propagation, i.e.  $\mathbf{Z}^{pp}$ .

In case of a via connected to both planes, the  $\mathbf{Z}^{pp}$  can be reduced after a 2D computation [1]. Once the expansion of the impedance between the ports is developed, it is assumed that the voltage across the ground via is zero, thus:

$$\begin{bmatrix} V_s \\ 0 \end{bmatrix} = \begin{bmatrix} Z_s^{pp} & Z_{sg}^{pp} \\ Z_{gs}^{pp} & Z_g^{pp} \end{bmatrix} \cdot \begin{bmatrix} I_s \\ I_g \end{bmatrix} \quad (2.32)$$

In (2.32), the terms were re-ordered by grouping the shorted-circuit ports, where the subscripts  $s$  and  $g$  refer to signal and ground vias, respectively, and the impedance matrix defined as  $\mathbf{Z}_t^{pp}$ . Furthermore, the reduced impedance matrix contains only parameters related to signal vias in (2.32):

$$Z_{t'}^{pp} = Z_s^{pp} - Z_{sg}^{pp} \cdot (Z_g^{pp})^{-1} \cdot Z_{gs}^{pp} \quad (2.33)$$

where  $Z_{t'}^{pp}$  is the Schur complement of  $\mathbf{Z}_t^{pp}$  [29]. At the end, the resulted matrix would present a size given by the number of signal vias, i.e. non-shorter ports.

Moreover, current physics-based via modeling is capable to include stripline traces modeled as transmission lines. In this lane, it has been developed and validated the extension

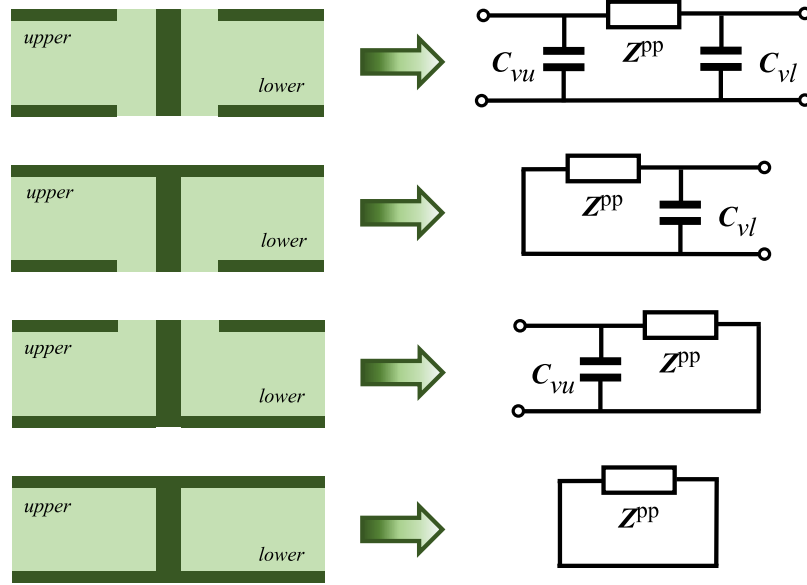


**Figure 2.5:** Different via-to-plane connectivity configurations. The connection or short circuit between the via and the plane results in a non-effect of the near-field interaction in the specific via segment, i.e. upper and lower [1].

of the modeling to include this interconnection [5]. The fact to model a via-to-trace transition represents a not-trivial topic due to the parallel-plate and transmission line modes are coupled at the cavity geometrical section. This coupling occurs at the via locations, which allows to compute each one separately. The analysis of these modes are based on a signal coming from a via and travelling through the stripline so, both modes can co-exist between the parallel planes. The Figure 2.6 shows a description of this physical effect.

Hence, modal decomposition [30] allows to analyze the presented modes as separate contributions. According to [31], it is possible to define a factor  $k$  who serves as coupling coefficient between the modes. This coefficient can be described as follows:

$$k \approx -\frac{h_l}{h_l + h_u} \quad (2.34)$$

where  $h_l$  and  $h_u$  are the dielectric lower and upper heights, shown in the Figure 2.6. More details about the extraction of the coupling coefficient can be found in [31]. The integration and formulation of the inclusion of stripline traces are presented in [5].

Thus, the formulation is expressed as following [1]:

$$\mathbf{Y}^T = \begin{bmatrix} Y^{cav} & -Y^{cav} \\ -Y^{cav} & Y^{cav} \end{bmatrix} + \begin{bmatrix} -k \cdot Y^{tl} & 0 \\ 0 & (k+1) \cdot Y^{tl} \end{bmatrix} + \begin{bmatrix} (k^2 + k) \cdot Y^{tl} & -(k^2 + k) \cdot Y^{tl} \\ -(k^2 + k) \cdot Y^{tl} & (k^2 + k) \cdot Y^{tl} \end{bmatrix} \quad (2.35)$$

The final effect  $\mathbf{Y}^T$  is a contribution of three components: the cavity model which contains

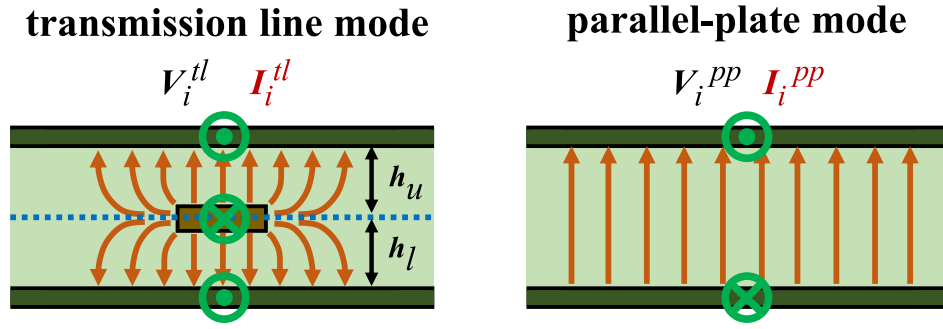


**Figure 2.6:** Electromagnetic modes presented in a cavity, as pointed in [5]. The transmission line and parallel-plate modes are coupled in case of a stripline trace routed into the cavity, and can be computed separately by using modal decomposition.

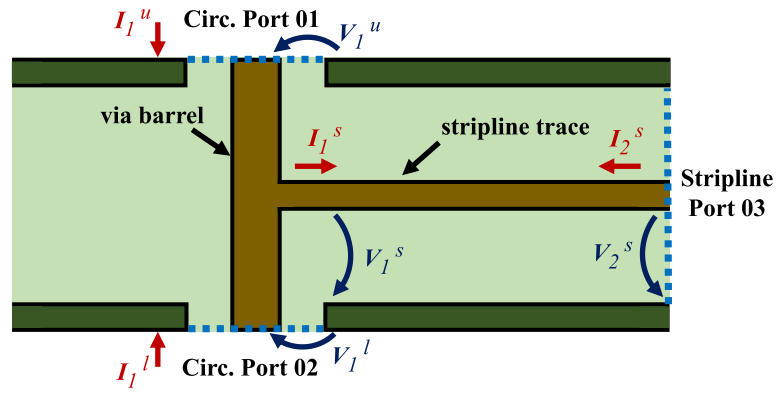


**Figure 2.7:** Stripline port definition for a trace embedded in a cavity.  $I_2^s$  and  $V_2^s$  are the electrical parameters that describe the stripline port, decoupled from the parallel-mode that co-exist into the cavity.

the via-to-plane interactions and the parallel-plate impedance, the trace transmission line model, and the modal transformation on the parallel-plate impedance and the transmission line mode [1]. This extension have been validated in several scenarios, as shown in [5]. Besides, a formulation to include stripline ports is proposed in [32] as well. The main aspect in this method is to get access to the electrical parameters of the port geometrical section. For instance, the Figure 2.7 presents the structure with the defined parameters for the analysis.

Theoretical formulation is expressed also in terms of the coupling coefficient  $k$  because of the need to obtain the transmission line mode, i.e. stripline mode, decoupled from the parallel-plate mode. Thus, the extended physics-based modeling is formulated as:

$$\begin{bmatrix} I_1^u \\ I_1^l \\ I_2^s \end{bmatrix} = \mathbf{Y}^{c3p} \cdot \begin{bmatrix} V_1^u \\ V_1^l \\ V_2^s \end{bmatrix} \quad (2.36)$$

where the matrix  $\mathbf{Y}^{c3p}$  contains the contribution of each element, and it is defined as:

$$\begin{aligned}
\mathbf{Y}^{c3p} = & \begin{bmatrix} Y^{cav} & -Y^{cav} & 0 \\ -Y^{cav} & Y^{cav} & 0 \\ 0 & 0 & 0 \end{bmatrix} + \begin{bmatrix} -kY_{11}^{tl} & 0 & kY_{12}^{tl} \\ 0 & (k+1)Y_{11}^{tl} & (-k-1)Y_{12}^{tl} \\ kY_{21}^{tl} & (-k-1)Y_{21}^{tl} & Y_{22}^{tl} \end{bmatrix} \\
& + \begin{bmatrix} (k^2+k)Y_{11}^{tl} & (-k^2-k)Y_{11}^{tl} & 0 \\ (-k^2-k)Y_{11}^{tl} & (k^2+k)Y_{11}^{tl} & 0 \\ 0 & 0 & 0 \end{bmatrix} \tag{2.37}
\end{aligned}$$

A more detailed analysis and validation can be found in [32], [33]. Until this point, there have been reviewed the analytical approximations to cover regular cases, where involves mostly fundamental modes that propagate across the conductor, whereas there exist several cases that do not present these characteristics, e.g. non-uniform currents, coupling and scattering between conductors, mode conversions, etc. Next section covers a review of some cases where physics-based modeling has not been enough to model these irregular behaviors.

## 2.2 Analysis of Irregular Configurations in Multilayer Substrates

Typically, in modern platforms exist more configurations and types of interconnects that differ with regard to what has been analyzed until this point. For instance, microstrip traces, differential signaling, coupling, shared antipads, non-ideal materials, etc., are some of the typical ones. In majority of these cases, anisotropic modes are excited and the current physics-based modeling cannot consider these kind of excitations. Several efforts have been made in order to close some of these gaps, e.g. [21]. In this work only the case of the microstrip transition and the mode conversion due to asymmetries are addressed.

### 2.2.1 Microstrip-to-Via Transitions

The transition between a microstrip trace and a via crossing into a cavity is called in the literature as turning via. These are smaller sections than a regular via crossing a cavity, and according to the literature, can present high-order propagated modes [34]. For instance, it is well known how the microstrip transmission lines present a non-uniform current across the conductor [35]. This produces that the current flowing through the turning via would also present the same characteristic so, the assumption of radial waveguide propagation by excited fundamental modes are not valid, and the effect can be extended to the parallel-plate propagation. Figure 2.8 depicts a representation of a turning via topology. According to [35], the field distribution here can be described as a function of the Fourier series of the azimuthal modes, as follows:

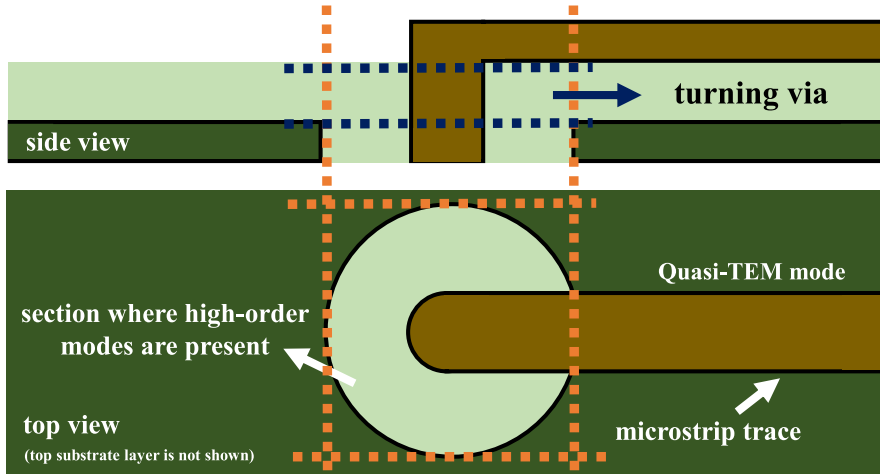


**Figure 2.8:** Turning via representation in top and side views. Quasi-TEM modes are propagated through the microstrip trace due to the difference of dielectrics. These modes arrive to the turning via and excite high-order modes in around the antipad geometrical sections, depicted with the dashed lines.

$$E_z(\phi) = \sum_{n=-\infty}^{\infty} E_n \cdot e^{jn\phi} \approx \sum_{n=-N}^N E_n \cdot e^{jn\phi} \quad (2.38)$$

This expression in (2.38) is a general solution of the 2D cylindrical wave function. The  $E_z$  represents the electric field strength in phasor notation,  $\phi$  the azimuthal angle, and  $n$  the mode order, whereas the Fourier coefficients can be expressed as:

$$E_n = \frac{1}{2\pi} \int_0^{2\pi} E_z \cdot e^{-jn\phi} d\phi \approx \sum_{k=0}^{N-1} E_z(k) \cdot e^{-jn \cdot 2\pi k/N} \quad (2.39)$$

where these coefficients represent the  $n$ th azimuthal mode of the electric field on the circumference of the port [35]. Nevertheless, in [7] it is proposed a model to this section, which is based on experimental results and extrapolates to geometrical parameters. This approach is proposed as  $T$ -connection made by lumped elements, similar as shown in the Figure 1.1 (b). It is important to denote that this model covers the turning via for the upper and lower stackup sections, but one turning via is modeled only as LC network. In the Chapter 3, it is presented an analysis about the convergence and agreement based on some simulation cases.

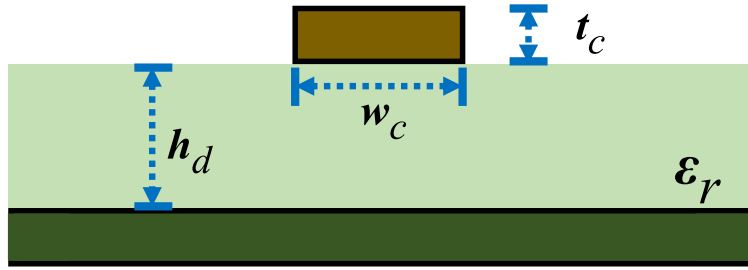


**Figure 2.9:** Microstrip line topology under analysis, where the characteristic impedance is a function of the geometrical parameters shown here. Besides, the frequency dependence is defined the propagation constant, and appears by the effect of the dielectric and conductor losses.

### 2.2.2 Analytical Description for Microstrip Lines

First of all, the analysis of the microstrip line is presented here, which has been mightly studied in literature. For instance, in [36], [37], and [38], it is formulated a robust analysis related to the description of this transmission line, main parameters and frequency dependencies, etc. In this work, a 2D definition is followed, similar as shown in [26]. This 2D representation is depicted in the Figure 2.9, where the structure is defined as  $2 \times 2$  admittance matrix, as a function of the geometrical and electrical parameters. Thus, the  $\mathbf{Y}^m$  can be described as follows:

$$\mathbf{Y}^m = \frac{1}{Z_0} \cdot \begin{bmatrix} \coth \gamma l & -1/\sinh \gamma l \\ -1/\sinh \gamma l & \coth \gamma l \end{bmatrix} \quad (2.40)$$

As shown in (2.40), the admittance matrix has roots on the characteristic impedance for each matrix entities, which everyone is scaled by this parameter and a function of the length of the microstrip  $l$  and the propagation constant  $\gamma$ . Both parameters can be computed analytically, with the exception that the dielectric material is non-homogeneous in the structure. This statement must be addressed by considering an effective permittivity that includes the substrate and air permittivities, respectively. In [37], it is presented an analysis for these considerations, which deal in more accurate results for high frequencies. Regarding the characteristic impedance parameter, in [36] is pointed a dependency in terms of the relation  $w_c/h_d$ , and can be approximated as following:

$$Z_0 = \begin{cases} \frac{60}{\sqrt{\epsilon_{eff}}} \ln \left( \frac{8h_d}{w_c} + \frac{w_c}{4h_d} \right), & w_c/h_d \leq 1 \\ \frac{120\pi}{\sqrt{\epsilon_{eff}[w_c/h_d + 1.393 + 0.667 \ln(w_c/h_d + 1.444)]}}, & w_c/h_d \geq 1 \end{cases} \quad (2.41)$$

being  $h_d$  the height of the dielectric, whereas  $w_c$  and  $t_c$  are the conductor width and thickness, respectively. As mentioned, the effective calculation of the permittivity considering both dielectrics can be more accurate, and also considers the different sources of losses in the structure that can predominate at high-frequency ranges. In this lane, three

approaches have been explored in terms of different calculations of the effective permittivity  $\epsilon_{eff}$  and propagation constant  $\gamma$ . The first approach is presented in [36], where the effective permittivity is expressed by:

$$\epsilon_{eff} = \frac{\epsilon_r + 1}{2} + \frac{\epsilon_r - 1}{2} \frac{1}{\sqrt{1 + 12w_c/h_d}} \quad (2.42)$$

This effective permittivity parameter is important when the dielectric losses is considered. A wave propagation across the microstrip line deals with an approximation, different as the stripline which faces an homogeneous material in its cross-sectional area. Furthermore, the second approach proposed a different calculation for this effective permittivity, based on Kirschning and Jansen's relations [38], where define an expressions as a function of the frequency and geometrical parameters. Thus, the effective permittivity is expressed as:

$$\epsilon_{eff}(f) = \epsilon_r - \frac{\epsilon_r - \epsilon_{eff}}{1 + P(F)} \quad (2.43)$$

where

$$P(F) = P_1 P_2 \left[ (0.1844 + P_3 P_4) 10 F H \right]^{1.5763} \quad (2.44)$$

The  $P$  expressions that describes the equation (2.44) are defined as:

$$P_1 = 0.27488 + \left[ 0.6315 + 0.525 / (1 + 0.157 F H)^{20} \right] (w_c / h_d) - 0.065683 e^{-8.7513 w_c / h_d} \quad (2.45)$$

$$P_2 = 0.33622 \left[ 1 - \exp(-0.03442 \epsilon_r) \right] \quad (2.46)$$

$$P_3 = 0.0363 \exp(-4.6 w_c / h_d) \left[ 1 - \exp \left[ - (F H / 3.87)^{4.97} \right] \right] \quad (2.47)$$

$$P_4 = 1 + 2.751 \left[ 1 - \exp \left[ - (\epsilon_r / 15.916)^8 \right] \right] \quad (2.48)$$

The third approach considers a better calculation of the conductor losses, based on what is proposed in [37]. This calculation involves the re-definition of the  $\gamma$  parameter with several dependencies. But, in terms of validation, the three approaches would be covered in order to find out the most convenient to include on the modeling proposal, according to accuracy, simulation time, etc.

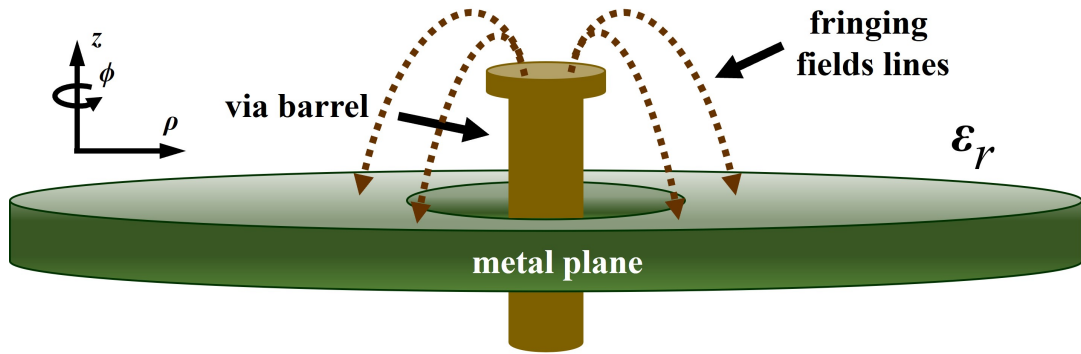


**Figure 2.10:** Via barrel crossing a metal plane, formulated in [6]. In this case, fringing capacitances between the via and plane can be calculated by using an integral equation. The calculation is defined by assuming axially symmetry around the via barrel.

### 2.2.3 Extraction of Fringing Capacitances of Turning Vias

The calculation of the contribution of the turning vias has been defined as a first approach in Section 2.2.1. It has been presented a briefly analysis where the effect of the presence of turning vias is analyzed, specifically in terms of the propagation of parasitic and fundamental modes. Thus, it has been shown that the contribution is mostly in terms of losses and scattering effects. Also, the statement of the physical height is pretty much shorter than the wavelength of interest addresses that the turning vias can be modeled with lumped elements.

Following this lane, there exist some approaches that have been characterized structures as similar to the turning vias. For instance, in [6] is presented a numerical method based on an integral equation, that describes the capacitance calculations between a via barrel crossing a metal plane. In case of regular platform implementations, pads need to be considered due to their presence in the majority of applications. Hence, a similar method is shown in [26], where the calculation of static capacitances due to the external fringing fields is presented as well, in presence of non-homogeneous dielectrics. The formulations of both methods are presented here.

In Figure 2.10 is shown the configuration under analysis to extract the via-to-plane capacitance, where some electric field lines are shown due to the excitation of propagation modes in the radial line. According to [6], an analysis of both structures, i.e. the via and plane, points the discretization of each conductor, and the respective calculation of each short-circuit capacitance. It is important to denote that, in this analysis, it is assumed both conductors are axially symmetric and the charge distribution as well. Thus, the short-circuit capacitance can be described as:

$$\mathbf{Q} = \mathbf{C}_s \cdot \Phi \quad (2.49)$$

where  $\mathbf{C}_s$  represents the short-circuit capacitance matrix,  $\mathbf{Q}$  is the vector with all conduc-

tors charge, and  $\Phi$  is the potential of each conductor with regard to the infinity. Thus, in case of the via (conductor 1) and the plane (conductor 2), it can be defined:

$$\begin{bmatrix} Q_1 \\ Q_2 \end{bmatrix} = \begin{bmatrix} C_{s11} & C_{s12} \\ C_{s21} & C_{s22} \end{bmatrix} \cdot \begin{bmatrix} \Phi_1 \\ \Phi_2 \end{bmatrix} \quad (2.50)$$

In case that the plane is connected to reference potential at the infinity, i.e.  $\Phi_2 = 0$ , it is possible to obtain the evaluation of the short-circuit via-to-plane capacitance, as following:

$$C_{via-to-plane} = C_{s21} = \frac{Q_2}{\Phi_1} \quad (2.51)$$

For the calculation of the relation between the charge density at the surface of conductors and potentials, an integral solution of Maxwell's equations based on the Green's function at the free space can be obtained. In this way, the discretization of each conductor and the integration across the geometrical parameters of each cell would lead to the calculation of the short-circuit capacitances. According to the geometry of the conductors, the cells are defined as vertical (via) and horizontal (plane) rings. Thus, assuming that there exist  $R$  ring cells, it would result in a  $R \times R$  system of equations, that can be shown as [6]:

$$\Phi = \mathbf{P}_s \cdot \mathbf{Q}_s \quad (2.52)$$

where  $\mathbf{Q}_s$  is the vector of charge of all the ring cells,  $\Phi$  is the vector of potentials of all ring cells, and  $\mathbf{P}_s$  is the matrix of  $ps_{ij}$  terms, that would be evaluated in the surface integrals to calculate the short-circuit capacitances. A set of integrals can be defined in order to calculate the mutual or self capacitances. For vertical (2.53) and horizontal (2.54) ring cells, the self-integrals can be defined as:

$$ps_{ii} = \frac{1}{8\pi^2\epsilon_0 h^2} \int_0^h \int_0^h \int_0^{2\pi} \frac{d\phi' dz' dz}{\sqrt{2\rho^2(1 - \cos \phi') + (z - z')^2}} \quad (2.53)$$

$$ps_{ii} = \frac{1}{2\pi^2\epsilon_0 (b^2 - a^2)^2} \int_a^b \int_a^b \int_0^{2\pi} \frac{\rho' d\phi' d\rho' d\rho}{\sqrt{\rho^2 + \rho'^2 - 2\rho\rho' \cos \phi'}} \quad (2.54)$$

where the parameters  $\rho$  is the radius of the vertical cell and  $h$  is the height of the same cell, and  $a$  and  $b$  are inner and outer radius of the horizontal cells. Following, the three different integrals are depicted in order to evaluate: a) vertical-to-vertical cell, (b) horizontal-to-horizontal cell, and (c) the vertical-to-horizontal cell. Thus, the expression for the vertical-to-vertical cell is defined as following:

$$ps_{ij} = \frac{\int_{l_1}^{l_2} \int_0^h \int_0^{2\pi} \frac{d\phi' dz' dz}{\sqrt{\rho^2 + \rho'^2 - 2\rho\rho' \cos \phi' + (z - z')^2}}}{8\pi^2\epsilon_0 h (l_2 - l_1)} \quad (2.55)$$

being  $h$  the height of the source cell,  $l_1$  and  $l_2$  the relative bottom and top elevations of the observation cell with regard to the bottom elevation of the source cell, and  $\rho'$  and  $\rho$  are the radius of the source and observation cells, respectively. For the horizontal-to-horizontal term, the integral is defined as:

$$ps_{ij} = \frac{\int_a^b \int_c^d \int_0^{2\pi} \frac{\rho\rho' d\phi' d\rho' d\rho}{\sqrt{\rho^2 + \rho'^2 - 2\rho\rho' \cos \phi' + (z-z')^2}}}{2\pi^2 \epsilon_0 (b^2 - a^2)(d^2 - c^2)} \quad (2.56)$$

where  $a$  and  $b$  are the inner and outer radius of the observation cell,  $c$  and  $d$  the inner and outer radius of the source cell,  $z$  and  $z'$  are the z-coordinates of the observation and source cells. Now, the integral formulation for vertical-to-horizontal cell is expressed as:

$$ps_{ij} = \frac{\int_a^b \int_0^h \int_0^{2\pi} \frac{\rho d\phi' dz' d\rho}{\sqrt{\rho^2 + \rho'^2 - 2\rho\rho' \cos \phi' + (z-z')^2}}}{4\pi^2 \epsilon_0 h (b^2 - a^2)} \quad (2.57)$$

and  $a$  and  $b$  are inner and outer radius of the horizontal cell,  $\rho'$  is the radius of the vertical cell,  $h$  is the height of the vertical cell, and  $z$  is the relative elevation of the horizontal cell to the bottom of the vertical cell, as pointed in [6]. The calculation of the terms  $ps_{ij}$  leads to obtain the matrix  $\mathbf{P}_s$ , depicted in (2.52). In general, let it assumes that there exist  $m$  conductors, and each conductor  $i$  ( $i = 1, 2, \dots, m$ ) is discretized into  $n_i$  cells, it is possible to define, considering (2.49) that:

$$\mathbf{Q}_{m \times 1} = \mathbf{A}' \mathbf{P}_s^{-1} \mathbf{A} \Phi_{m \times 1} \quad (2.58)$$

where  $\mathbf{A}$  is a matrix with vectors at the entities that relates the capacitances between conductors. Thus, considering all these parameters, the short-capacitances can be described as:

$$\mathbf{P}_s^{-1} = \begin{bmatrix} [\mathbf{C}_{11}]_{n_1 \times n_1} & \cdot & [\mathbf{C}_{1i}]_{n_1 \times n_i} & [\mathbf{C}_{1m}]_{n_1 \times n_m} \\ \cdot & \dots & \cdot & \cdot \\ [\mathbf{C}_{i1}]_{n_i \times n_1} & \cdot & [\mathbf{C}_{ii}]_{n_i \times n_i} & [\mathbf{C}_{im}]_{n_i \times n_m} \\ [\mathbf{C}_{m1}]_{n_m \times n_1} & \cdot & [\mathbf{C}_{mi}]_{n_m \times n_i} & [\mathbf{C}_{mm}]_{n_m \times n_m} \end{bmatrix} \quad (2.59)$$

where the total charge of the  $m$ -conductor can be assumed to zero. These formulations summaries the method of calculation of the via-to-plane capacitance in [6]. Now, the formulation for the pad-to-plane fringing capacitances is explored, based on the analysis in [26]. The Figure 2.11 depicts the configuration that refers as baseline of the analysis. One of the main concerns related to this calculation is to address the treatment of different dielectrics, which can be shown in the Figure 2.11. For instance,  $\epsilon_{r1}$  is commonly defined as air, whereas the parameter  $\epsilon_{r2}$  refers to the substrate used to build up the stackup. According to [26], the surface charges are considered as a single layer, and at the interface the field strength presents a discontinuity, as similar case than the field lines distribution

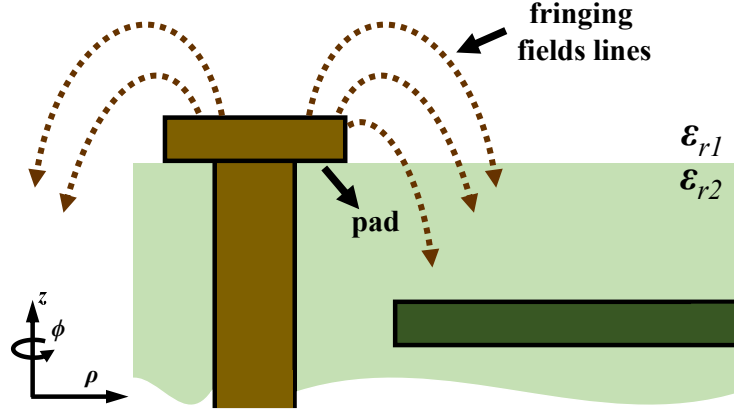


**Figure 2.11:** Upper segment configuration that represents the fringing fields lines between the pad and the metal plane.

around a microstrip line. Thus, the electric field in  $r$  and  $z$ -coordinates can be expressed as:

$$E^{(r)} = \frac{1}{2\pi\epsilon_0 r} \int_{S_Q} \sigma(\vec{r}'_Q) \cdot \rho_Q \cdot \frac{b^2 \cdot K(k) - [\rho_Q^2 - \rho^2 + (z - z_Q)^2] \cdot E(k)}{a \cdot b^2} dr_Q \quad (2.60)$$

$$E^{(z)} = \frac{1}{\pi\epsilon_0} \int_{S_Q} \sigma(\vec{r}'_Q) \cdot \rho_Q \cdot \frac{(z - z_Q)^2 \cdot E(k)}{a \cdot b^2} dr_Q \quad (2.61)$$

where  $\sigma$  is the surface charge density,  $\rho_Q$  and  $z_Q$  are the coordinates of the source point, and  $\rho$  and  $z$  are the same for the observation point. Also,  $K(k)$  and  $E(k)$  is the complete elliptic integral of first and second kind respectively, with modulus  $k = \sqrt{4\rho\rho_Q}/a$ , and  $b^2 = (\rho - \rho_Q)^2 + (z - z_Q)^2$  and  $a^2 = (\rho + \rho_Q)^2 + (z - z_Q)^2$ , where are the distance between the observation and source points. In case of the matching condition at the interface of dielectrics, the normal components of electric fields  $E_n$  is given by:

$$\epsilon_{r1} E_{n1} = \epsilon_{r2} E_{n2} \quad (2.62)$$

Following the same relation in (2.52), the matrix that relates the potentials in the conductors with the surface charge density in the via, plane and dielectric, is expressed as:

$$\begin{bmatrix} \Phi_{via} \\ \Phi_{plane} \\ 0 \end{bmatrix} = \begin{bmatrix} \mathbf{P}_{via,via} & \mathbf{P}_{via,plane} & \mathbf{P}_{via,diel} \\ \mathbf{P}_{plane,via} & \mathbf{P}_{plane,plane} & \mathbf{P}_{plane,diel} \\ \mathbf{M}_{diel,via} & \mathbf{M}_{diel,plane} & \mathbf{M}_{diel,diel} \end{bmatrix} \cdot \begin{bmatrix} \sigma_{via} \\ \sigma_{plane} \\ \sigma_{diel} \end{bmatrix} \quad (2.63)$$

where the sub-matrices  $\mathbf{p}$  is the potential between each contour segment defined in each conductor, and  $\mathbf{M}$  is the matching condition on the dielectrics interface. The  $\sigma_{diel}$  repre-

sents the surface density charge on each segment of the dielectrics interface. In order to calculate the free charge for the calculation of the capacitances, each element in  $\sigma_{via}$  and  $\sigma_{plane}$  must be multiplied by the  $\epsilon_r$  of the adjacent substrate. At the end, the calculation of the capacitance is calculated by considering the relation in (2.49).

## Chapter 3

# Validation of Physics-Based Via Modeling and Irregular Configurations

As mentioned before, physics-based modeling has been developed by considering fundamental electromagnetic modes propagating through different configurations and interconnects, such as a via crossing adjacent metal planes, striplines traces, etc. In this chapter, different topologies are explored in order to explore the limits of the current modeling approach, compared with full-wave simulations. Thus, some structures and configurations with different numbers of metal layers are correlated here, which will cover the baseline about the aim of this thesis. For instance, regular and irregular cases are built and the extraction of their frequency response by using scattering parameters would present the comparison among them.

First of all, the analysis of regular cases is presented. Three different topologies with the exactly same geometrical parameters, but different number of metal layers are shown, and these will depict the effect of the number of cavities for each stackup in frequency domain. For these cases, the structures are excited by fundamental modes and fringing capacitances are not considered due to the coaxial ports. On each of these cases, two different modeling approaches are evaluated, i.e. Williamson [2] and  $\pi$ -network model [15], in order to analyze the agreement against full-wave solvers [39]. These modeling approaches are extracted by using CONMLS [40], which is a simulation framework for multilayer substrates developed at the Institute of Electromagnetic Theory, TUHH. Once the regular cases are validated, cases of study related to microstrip-to-via transitions are analyzed. This irregular case has been mentioned in Section 2.2.1 of this thesis, where these via transitions are called as turning vias. A first approach is presented based on an experimental results, and the correlation in a segmented environment against full-wave solutions is validated as well.

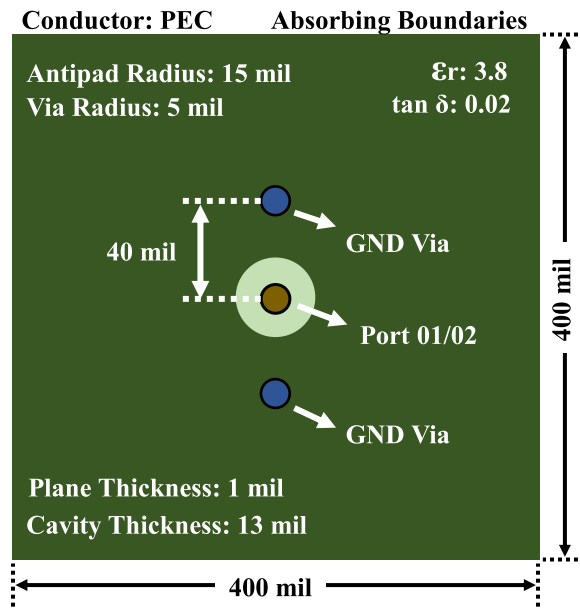


**Figure 3.1:** Top view of the structure under analysis for regular cases. As depicted, a signal via is surrounded by two ground vias to improve the return path performance, and coaxial ports are placed at the top and bottom of the each stackup.

### 3.1 Simulation of Physics-Based Via Modeling in Multilayer Substrates

In order to validate the current physics-based via modeling, the three structures shown in Figure 3.1 and Figure 3.2 are simulated under different modeling approaches. First, the baseline reference is FEM [39], which is the most accurate method considered in this thesis. Besides, approaches based on Williamson method and the  $\pi$ -network model are included as well. The Williamson approach is described in (2.22), considering the effect of the parallel-plate impedance. Related to the  $\pi$ -network model, it is described in (2.15), where the capacitance values are calculated in (2.12) and (2.13). It is important to note that the CIM was used for the calculus of the far-field interaction, and all these results are obtained from CONMLS [40] framework. The via and antipad radius are defined as 5 and 15 mil respectively, the cavity thickness is 13 mil, infinite planes are considered as boundary conditions, the coaxial ports are described by 20 mil length, but they have been de-embedded in order to dismiss their effects, and two ground vias are placed in a 40 mil equidistance with regard to the signal via.

Regarding to the model characteristics, the Figure 3.1 presents the top view for the configurations. In fact, all the analyzed cases here present same geometrical parameters, with the corresponding additions according to the case of study. The Figure 3.2 depicts the side view of the structures. As mentioned in [15], a topology with more than one cavity is modeled by using segmentation techniques, where each cavity is processed separately, assuming no interaction between them due to the skin effect, which is expressed by the

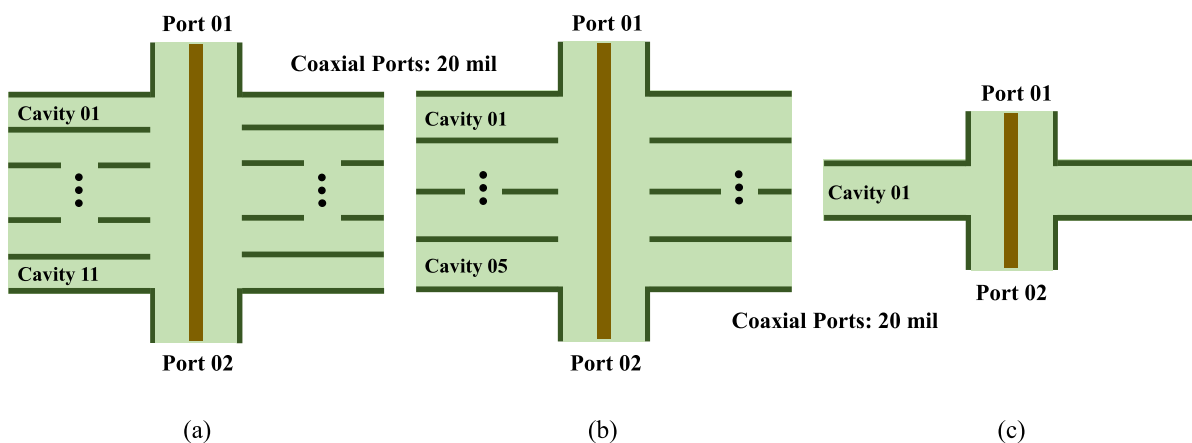


**Figure 3.2:** Side view for the simulated structures, i.e (a) 11-cavities, (b) 5-cavities, and (c) 1-cavity stackups. All the configurations present coaxial ports of 20 mil of length, which have been dismissed by using de-embedding techniques.

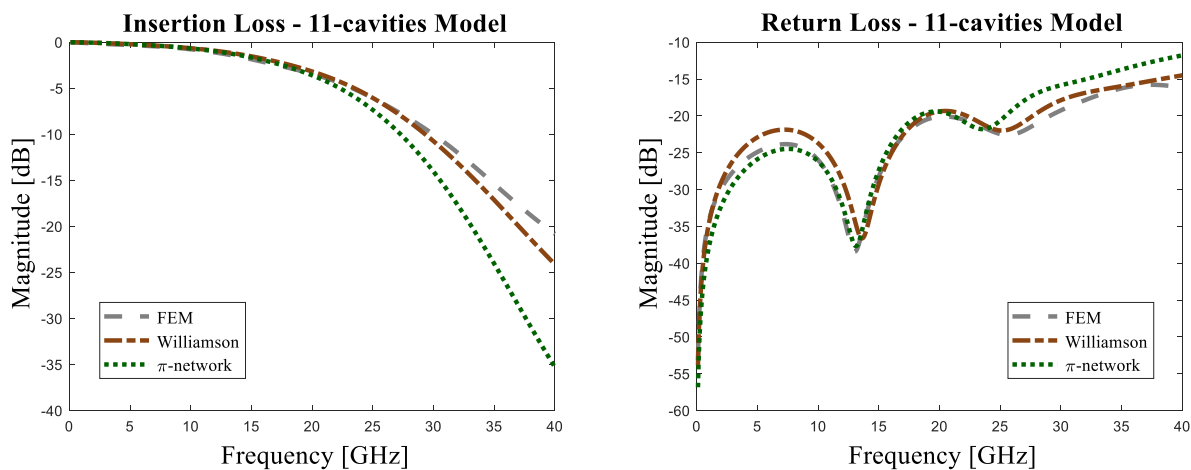


**Figure 3.3:** Scattering parameters for the 11-cavities model. Left graph refers to the transmission coefficient, similarly the right one represents the reflection parameter. The  $\pi$ -network model presents an important deviation from the FEM solutions around 20 GHz and beyond.

return currents flowing across the metal plane surfaces. It is expected to obtain higher losses on cases that present high number of cavities, because of the interconnection would increase the electrical length, and more scattering effects and interactions are produced due to the multiple cavities. Hence, the frequency responses for the cases depicted in the Figure 3.2 are presented in the Figures 3.3, Figure 3.4, and Figure 3.5. As it is possible to note, it is confirmed that the 11-cavities configuration presents more losses than the rest ones, and the resonance frequencies increase as well.

The correlation between modeling approaches confirms what it is pointed in the literature [4]. For instance, the  $\pi$ -network model presents a good agreement in relative low frequencies, but as the frequency increases, an important deviation begins to appear. This deviation starts to be relevant up to around 20 GHz, and as mentioned in [3], the calcu-

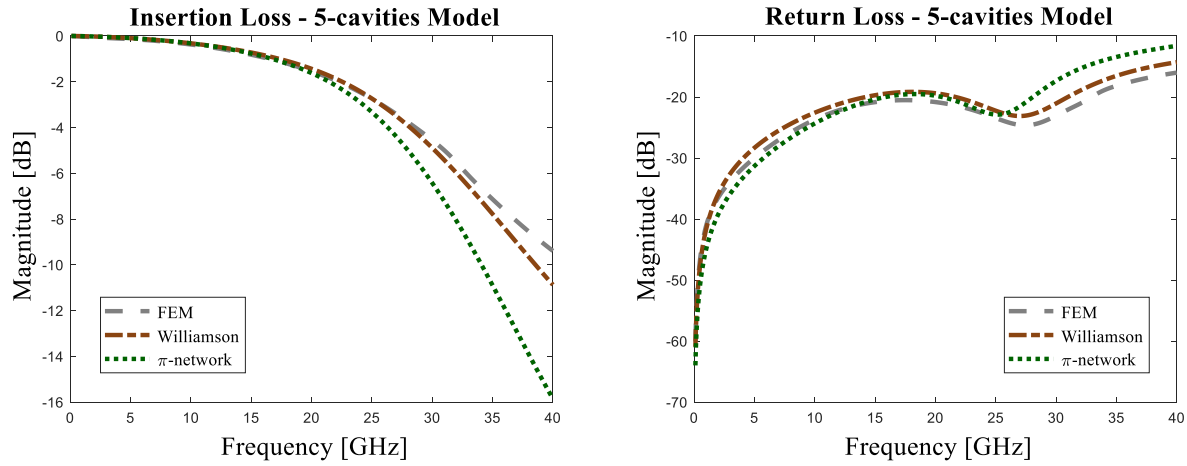


**Figure 3.4:** Scattering parameters for the 5-cavities model. Same as 11-cavities case response, the  $\pi$ -network model presents an important deviation from the FEM results in around 20 GHz, which is more denoted in the insertion losses parameter.

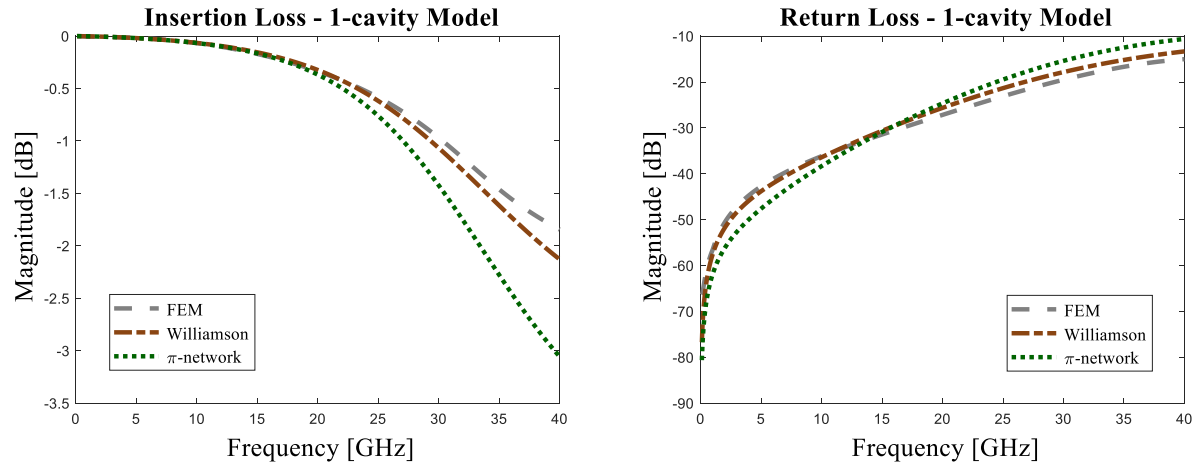


**Figure 3.5:** Scattering parameters for the 1-cavity model. Similar as the other regular cases, the  $\pi$ -network model presents itself a lesser accuracy than Williamson approach for high-frequency ranges. For short vias, this effect is more pronounced in the  $\pi$ -network model, as denoted in [1].

lation of the near-field interaction is more intuitively for low-frequency ranges. However, in case of Williamson approach, it presents a better agreement compared to the FEM solution, mostly at high frequencies. According to [4], the deviation between Williamson approach and the  $\pi$ -network model refers to, in frequencies up to 10 GHz, the ratio  $R$  of the transformer in the equivalent circuit (Figure 2.3) is around 1, and the magnitude of the susceptances  $jB_b$  and  $jB_3$ , who behave as a positive and negative inductance respectively, are similar to each other so, they might be canceled out. Thus, based of these topics, the Williamson approach would be a better option to use in multilayer substrate simulations, in order to get more accurate results. An analysis about the behavior of the elements in the Williamson equivalent circuit as a function of the frequency is presented in [4].

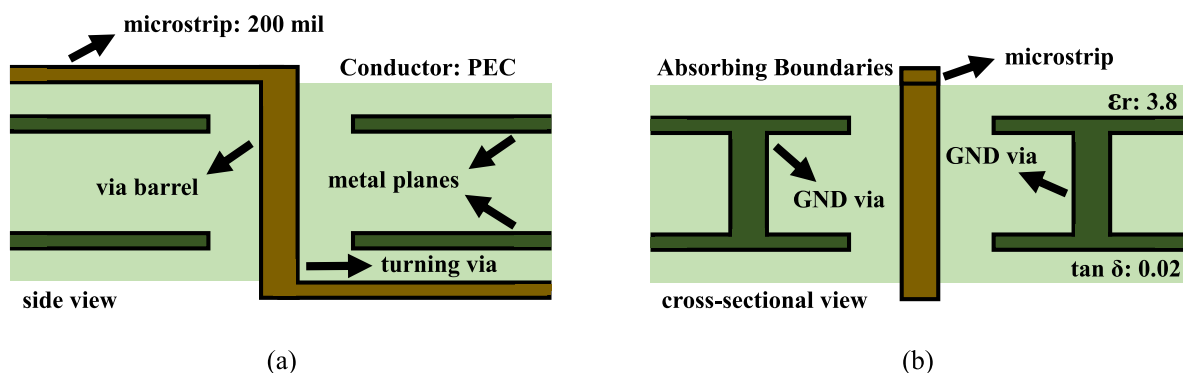


**Figure 3.6:** Configuration that contains microstrip-to-via transitions. These transition structures are commonly present in break-out/in sections, e.g. memory interfaces. The analysis of the structure by using FEM allows the visualization of the turning via effects represented by using scattering parameters.

## 3.2 Analysis of Irregular Configurations for Via Modeling

### 3.2.1 Considerations of Microstrip-to-Via Transitions

The microstrip-to-via transition configuration is categorized as irregular case, according to the characteristics mentioned in the Section 2.2.1. The microstrip excited by a current would create a quasi-TEM modes that propagate across the trace, i.e. due to the differences on the substrates, and produces a variation of the field propagation around the microstrip. Additionally, the current distribution across the trace is non-uniform, oriented to the bottom side of the microstrip, which is the closest one to the metal plane. Once the non-uniform current arrives to the turning via, it must be re-oriented to flowing vertically out across the via section, which deals to the excitation of high-order modes in the structure. In [35], it is possible to get a deeper insight of this behavior. Figure 3.6 presents the structure to analyze these effects, where it is presented a microstrip-via-microstrip configuration with the respective transitions. The via barrel is enclosed between two metal planes, being the regular cavity model defined for a via in the physics-based via modeling approaches. Among the geometrical parameters, the via and antipad radius are defined as 5 and 10 mil respectively, cavity substrate thickness is 13 mil, metal plane thicknesses are both 1 mil, and ground vias are placed with 40 mil of equidistant with regard to the signal via as well. The microstrip thickness and width are 1 and 10 mil, and top/bottom substrate thicknesses are defined as 5.6 mil; in order to obtain around 50 Ohm of characteristic impedance. As same as before cases, infinite planes are considered as boundary conditions, and all these parameters are used for the next cases of analysis.

Hence, this structure is simulated by using FEM method, and the scattering parameters are depicted in the Figure 3.7. These results can show the effect of the turning vias, and conclude whether they have relevance to consider in pre-layout simulations or can

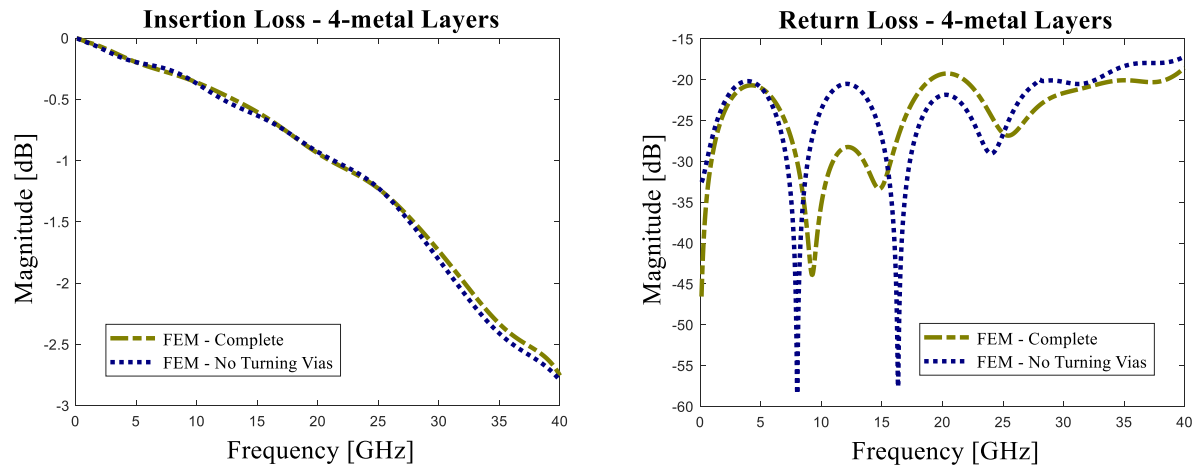


**Figure 3.7:** Comparison between full-wave results of the complete topology, shown in the Figure 3.6, and the scattering parameters by including only the pair of microstrip transmission lines and the cavity section. The effect of the turning vias is reflected mostly for frequencies beyond 8 GHz.

be neglected. In that way, it is possible to construct a segmented model for comparison purposes, such as two microstrip transmission lines, separated by a cavity model. The difference between both models is that the segmented model does not consider any turning via. The scattering parameters about this segmented model is shown in the Figure 3.7 too. The microstrip models are extracted by using FEM as well as the cavity mode, shown in the Figure 3.2 (c). As it is possible to visualize, the effect of the turning vias has roots on the return loss values. Regarding these ones, a good agreement is achieved for values up to around 8 GHz, with the differences in the respective anti-resonant frequencies. In terms of insertion losses, the interconnects do not present a considerable deviation with regard to complete FEM results. Moreover, it is also possible to see how the turning vias become more important as the frequency increases, which it is the trend in modern interfaces.

Furthermore, as it was analyzed in Section 2.2.1, the structure shown in Figure 3.6 (a) can propagate high-order modes, depends on the frequency range of interest. In this lane, it is possible to extract the effect of these modes, by looking the propagation constant  $\gamma$ . This is a common parameter in transmission lines theory, which provides information related to the change that a signal undergoes by the amplitude and phase when it propagates in a given direction. Specifically, by analyzing the phase constant  $\beta$  [deg/m], it is possible to observe the frequency ranges where the high-order modes would be significant for the mode propagation of the topology. For instance, the same scenario in the Figure 3.6 is considered, whereas another one similar is defined, with the difference that includes a 10 mil pads at top/bottom on the structure. The Figure 3.8 presents the effect of these high-order modes up to 100 GHz. The effect on the pads in the parasitic mode propagation is basically very low, because of the 1<sup>st</sup> and 2<sup>nd</sup> high-order modes present very similar cut-off frequencies. Moreover, the 1<sup>st</sup> high-order mode is presented up to around 40 GHz,

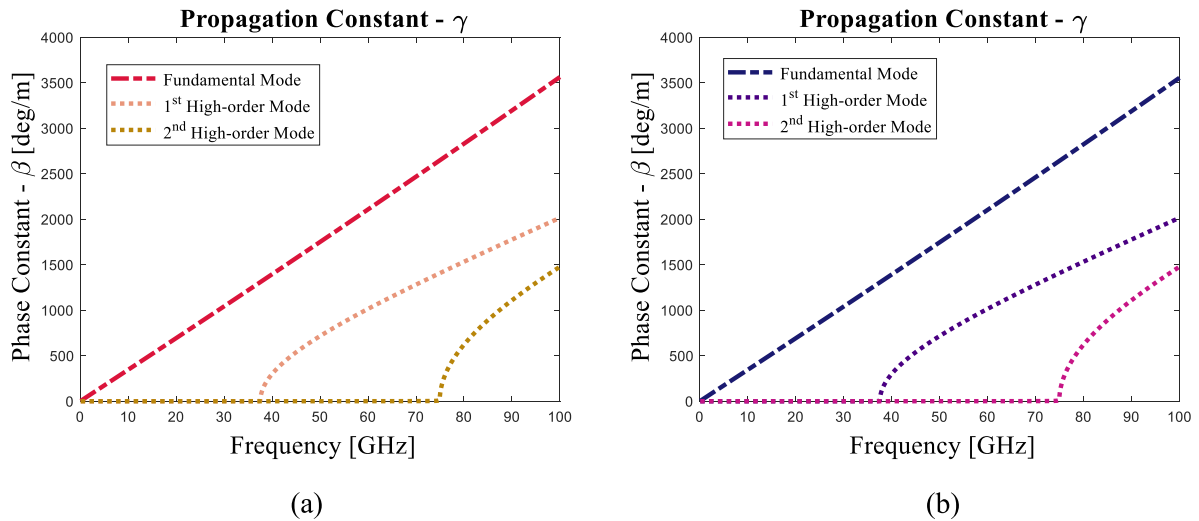


**Figure 3.8:** Phase constant for different configurations of Figure 3.6 (a) with no pad, and (b) including a 10 mil pads at top/bottom segments. High-order modes are present in relative high frequencies, where the 1<sup>st</sup> one appears up to around 40 GHz. The effect of the pad can be neglected during the analysis of propagation of the high-order modes.

which indicates that for these types of configurations, a modeling approximation can be estimated by assuming fundamental modes propagating through the turning vias with no high relevance from parasitic modes. This statement would give a baseline for the turning via modeling approach.

Following the turning via modeling considerations, in [7] is presented a proposal for microstrip-via-microstrip configuration, which can be extended to model a single turning via. Thus, the Figure 3.9 shows the proposed topology. As mentioned, some approaches before have tried to model it out as a  $\pi$ -network, but it has been found that a  $T$ -network would be more suitable according to the equivalent admittance seen by each port [7]. The lumped parameters come from experimental results, as a function of the geometrical parameters of the configuration, such as dielectric height, via barrel and antipad radius, and pad radius. In case to describe a configuration that contains turning vias at the top and bottom of the stackup, the model can be separated, by dividing the equivalent capacitance  $C_t$  by the half. Hence, the modeling for a single turning via is proposed by one inductance  $L_t$  and a capacitance  $C_t/2$ . As a method that came from experiment analysis, it can be used as first approach to model the turning via, but it is insufficient to consider it into a formal description. Even though, this modeling provides a good feeling about the inherent nature of this section. These ones are shorter than a regular cavity height, and this permits that the sections can be described with lumped elements, as a first approximation. This statement can be also supported by the physical height is pretty much shorter than the wavelength of interest.

Thus, the  $T$ -network model formulation can be used to compare the agreement against full-wave solutions, similar as the Figure 3.7. For instance, the same segmented structure has been modified by adding the LC lumped models for each turning via, as the Figure 3.10

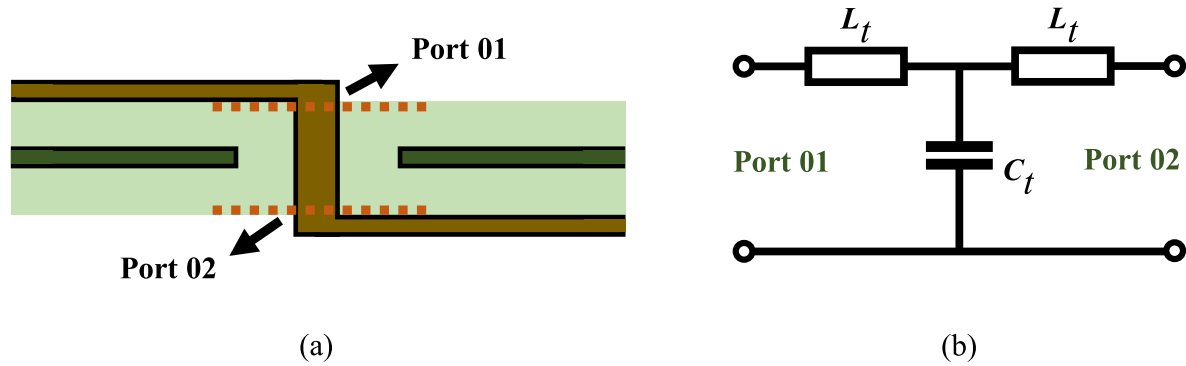


**Figure 3.9:** The (a) microstrip-via-microstrip configuration and (b) the equivalent  $T$ -network representation. Each single turning via is represented by a inductance  $L_t$  and a capacitance, defined as  $C_t/2$ .

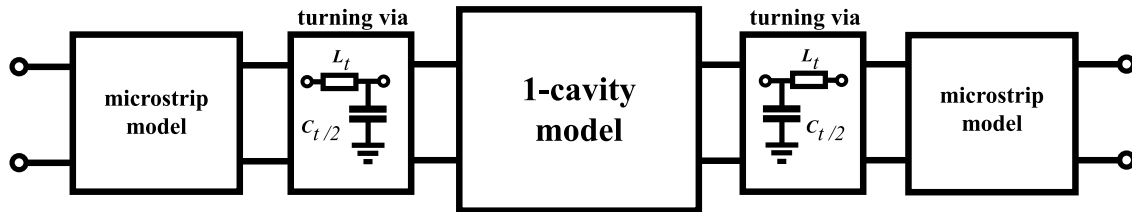


**Figure 3.10:** Segmented model including the turning vias for top and bottom at the stackup under analysis. This representation is based on the  $T$ -network proposed in [7].

depicts. In case of the physical parameters used in the configuration, the approximation for these elements are  $L_t = 110.7 \text{ pH}$  and  $C_t = 41.2 \text{ fF}$  [7] though, these values are not exactly for the configuration under analysis. The scattering parameters comparison is shown in the Figure 3.11, where the agreement has been improved compared to the Figure 3.7. There exist some deviations, for example the anti-resonant frequency at around 15 GHz, but in general the model presents good agreement against full-wave results. Hence, this confirms the nature of the turning vias behavior, which can be approximated as lumped elements model.

Regarding the modeling comparison, a second structure is proposed to analyze. This consists in two via barrels embedded in a cavity, connected to each other by a microstrip line of 200 mil of length. As similar than before cases, each signal via is surrounded by two ground vias to improve the performance of the return path. Geometrical parameters are the same as before as well, and the Figure 3.12 shows the cross-section of the configuration under analysis. The structure is composed by a segmented model with a 4-port cavity model which includes the far and near-field propagation into the cavity and between the vias, connected to the external structure, i.e. a couple of turning via models and the microstrip transmission line. The compared scattering parameters are depicted in the Figure 3.13. Similar to the before case, in high frequencies present the relevant disagreements, which can be associated with the frequency-dependence effects of lumped elements. However, a formulation to describe these sections are proposed in chapter 4,

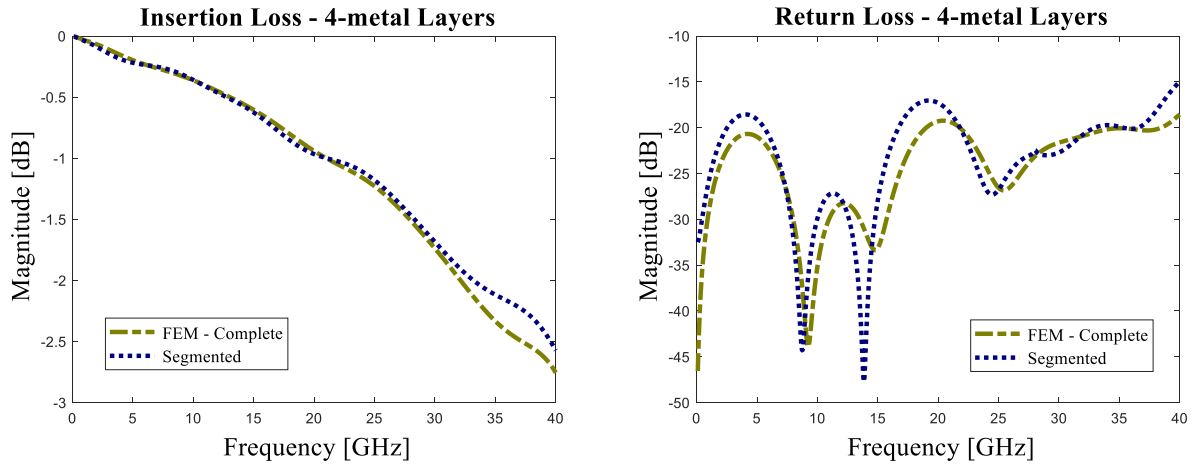


**Figure 3.11:** Scattering parameters comparison between the structure shown in the Figure 3.6 and the segmented topology in Figure 3.10, which includes the modeling for the turning vias. There seems acceptable agreement between models for relatively low and high-frequency ranges.

as part of the extension of physics-based modeling including the turning via description, as well as microstrip ports. These formulations are based on previous investigations, but the extension of these approaches to the existing physics-based modeling framework, is part of the main contribution of this work.

Similarly as the analysis in the Figure 3.8, the propagation constant  $\gamma$  provides a sense about the modes propagating through the structure. The Figure 3.14 depicts the response of the phase constant  $\beta$  as a function of the frequency up to 100 GHz. It is interesting to note that fundamental mode is almost the only that propagates in the structure, whereas the high-order modes are suppressed. This effect can be explained because of the excitations are made by circular ports, de-embedding the effect of the coaxial extensions. The modeling of coaxial lines is based on fundamental modes propagating to the structure, due to the high-order modes cut-off frequencies appear around 300 GHz for regular geometries [8]. Hence, in this case of study in Figure 3.12, the parasitic modes are attenuated and it is expected to not get high influence for relative interested frequency ranges, as shown in Figure 3.14.

Moreover, it has been stated the influence of microstrip and turning vias in the excitation of parasitic modes propagation, but it is interesting to analyze also the effect under different configuration contexts. For instance, these external structures can be connected to several cases and topologies, e.g. stackup with different number of cavities, striplines traces, differential configurations, etc. Thus, a couple of scenarios have been defined in order to analyze the effects. These configurations are depicted in the Figure 3.15, where a case with microstrip-to-microstrip interconnection through 5-cavities stackup is analyzed, and the frequency response is shown in the Figure 3.16. The scattering parameters response in Figure 3.16 (a) presents the insertion and return losses which presents similar trend as the results of 5-cavities stackup shown in Figure 3.4, but the most interesting behavior is shown in Figure 3.16 (b), where the high-order modes response is

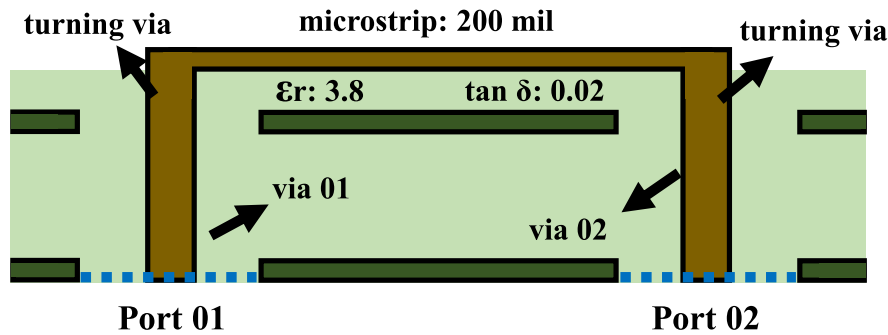


**Figure 3.12:** Additional configuration that contains microstrip-to-via transitions. The cavity model includes the effect of the far and near-field interaction, as well as the scattering among vias. External structure includes a 200 mil microstrip trace connected in both sides by a turning via.

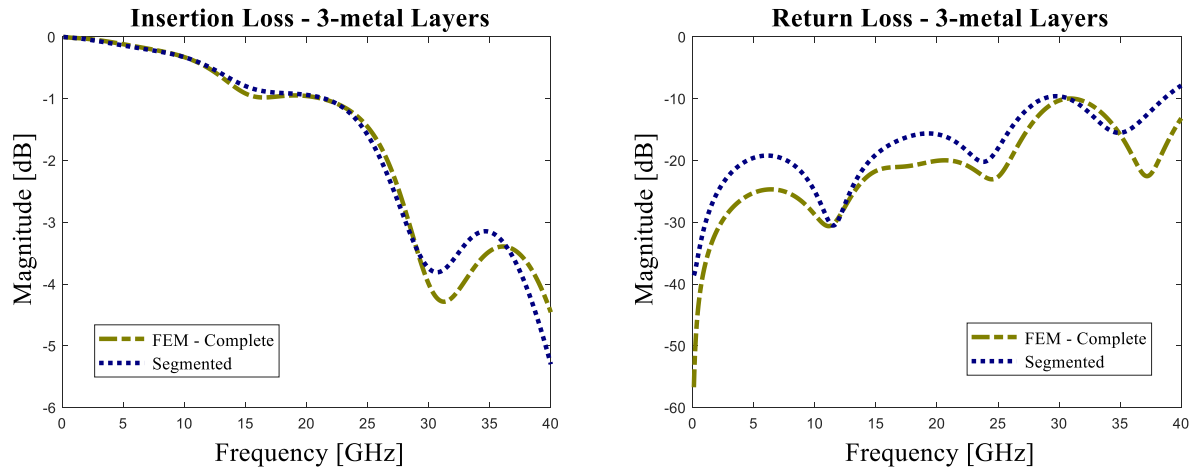


**Figure 3.13:** Scattering parameter of the structure shown in Figure 3.12. Main deviations are presented in high frequencies, where the frequency-dependence effects of lumped element appear and affect the model accuracy.

quite similar as the obtained for only 1-cavity case. This statement is expected because of, as analyzed in Chapter 2, the assumption for the cavity modeling is that only fundamental modes propagates in the structure so, in this case the effect of parasitic modes is still caused by the external connection, i.e. microstrip and turning vias.

Another case to analyze is depicted in the Figure 3.15 (b). A transition to a stripline trace, which is commonly used in multilayer applications is shown. This is a structure where the near-field interaction is not completely described in literature, but good approximations have been developed in order to include stripline trace descriptions in physics-based modeling [15], [32]. Similar as before, scattering parameters and propagated modes responses are extracted, and results can be visualized in the Figure 3.17. It is interesting that there is no relevant differences again compared other cases, and the the external connections are still the dominant in terms of the propagation of high-order modes. According to full-wave simulations, these stripline transitions can lead to the propagation of parasitic

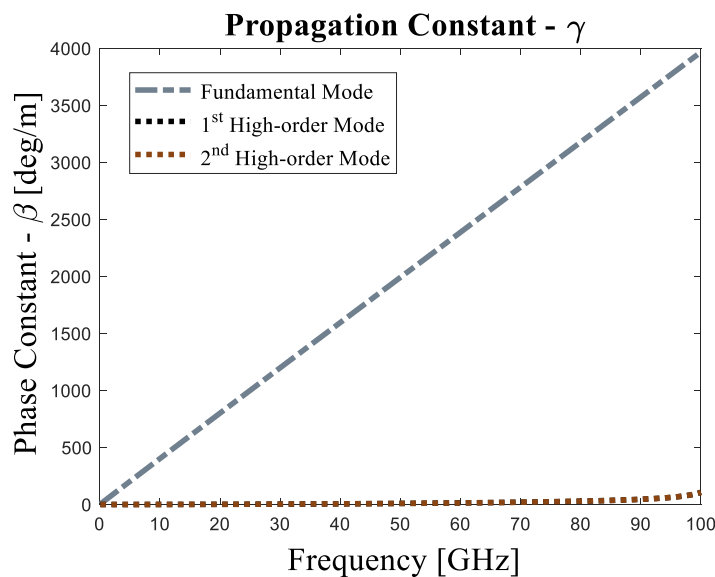


**Figure 3.14:** Phase constant  $\beta$  for the configuration in Figure 3.12. Parasitic modes are highly attenuated due to the excitations of coaxial ports, where these modes tend to appear around 300 GHz for regular cases, according to [8].

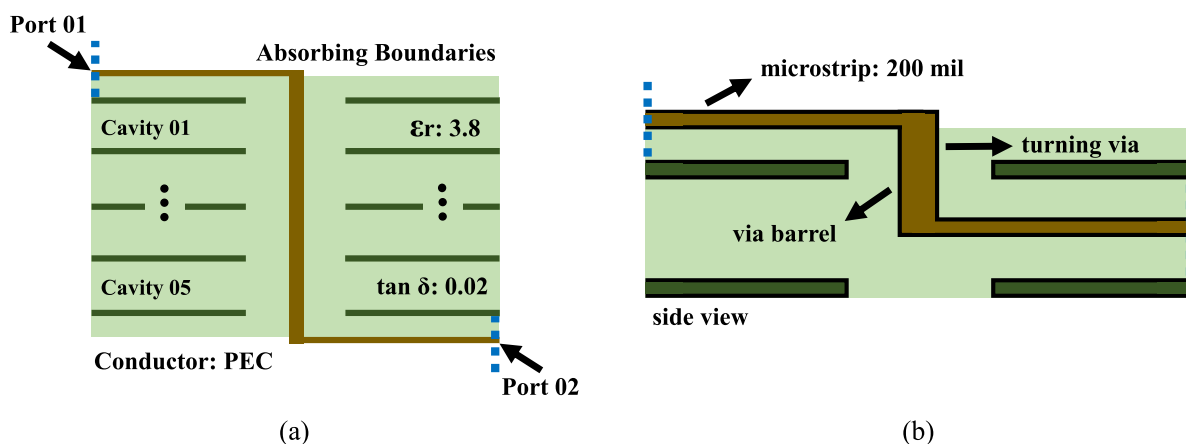


**Figure 3.15:** Different configurations to analyze the effect of parasitic modes propagation due to turning vias (a) 5-cavities stackup, and (b) microstrip-to-stripline transition. It has been shown the effect of these transitions in terms of the propagation of high-order modes, e.g. Figure 3.8.

modes when there exists an impedance mismatching in the structure, as depicted in Figure 3.18. These frequency response graphs correspond to a stripline-to-stripline transition structure, where the difference between each other is the characteristic impedance. The Figure 3.18 (a) shows the propagated modes for an impedance of around 51 Ohm, whereas the Figure 3.18 (b) correspond to a 31 Ohm. It is possible to visualize from results that the cut-off frequencies for parasitic modes are decreasing by around the half, in case of 31 Ohm. In this way, in physics-based modeling, the inclusion of stripline traces must be considered with the disclaimer of matched transmission lines. However, in manufacturing

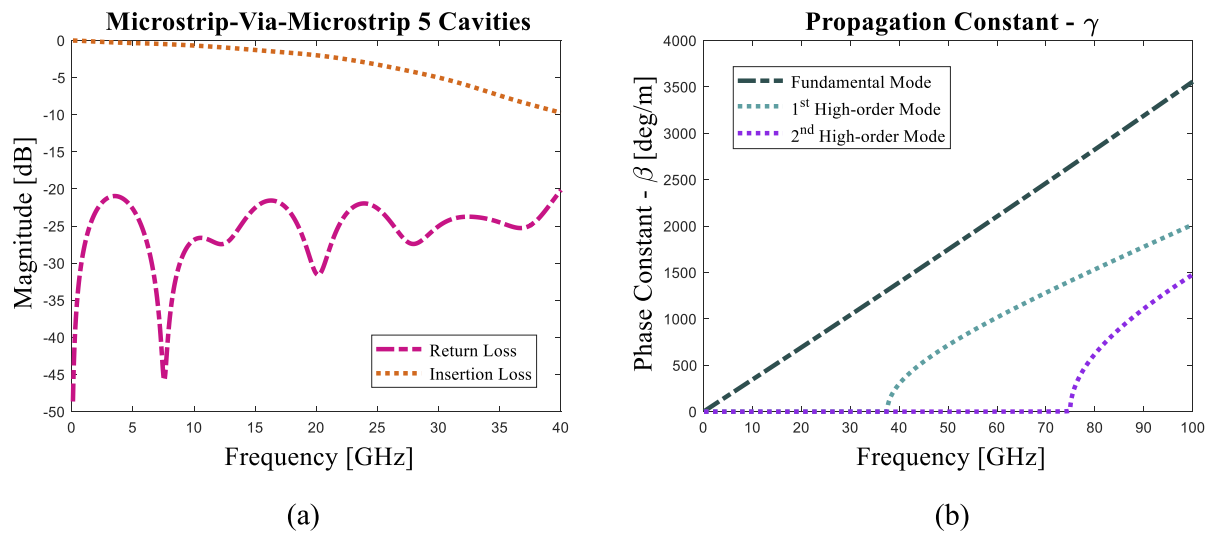


**Figure 3.16:** Frequency response of the topology depicted in Figure 3.15 (a), where in (a) is shown the scattering parameters for insertion and return losses, and (b) presents the response of the propagated modes. Comparing with Figure 3.8, there is no evidence of the influence for parasitic modes due to higher number of cavities. It is expected due to the assumption of physics-based modeling that only fundamental mode propagates across these structures.

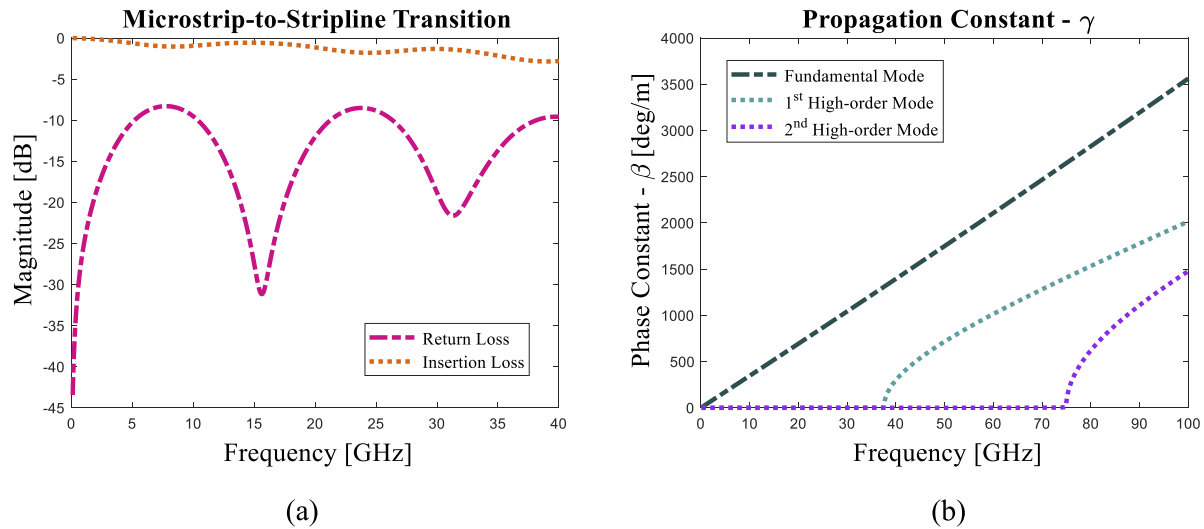


**Figure 3.17:** Response of (a) scattering parameters - return and insertion losses, and (b) propagated modes of the in Figure 3.15 (b). As same case as Figure 3.16, there is no influence of stripline transition for a matched stripline trace.

process, this can be a potential issue for implementations of high-speed interfaces.

Based on the approaches presented, it is interesting to make a comparison between them, in order to analyze the agreement in terms of the scattering parameters, as well as the phase response for each case. In this particular, an analysis of the topology shown in the Figure 3.6 is the case of study. As same as the cases before, FEM method is the baseline to compare the convergence of the modeling approaches. In Section 2.2.4, it is considered

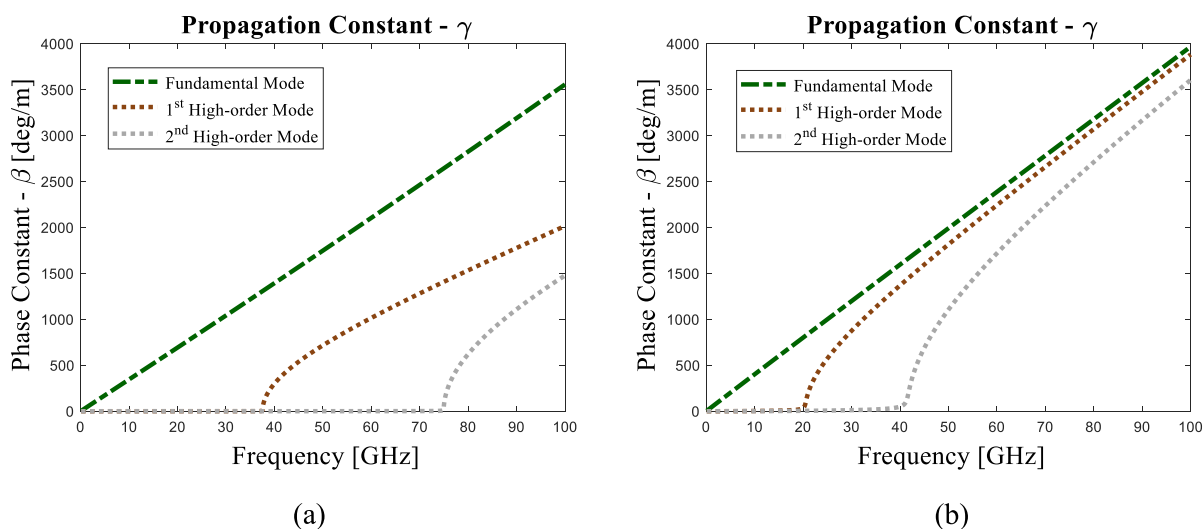


**Figure 3.18:** Propagated modes in a stripline-to-stripline transition for (a) matched and (b) mismatched striplines. By considering an impedance mismatch in the striplines traces can lead to a decreasing of the cut-off frequencies of high-order modes. The mismatched stripline case presents a characteristic impedance of around 31 Ohm.

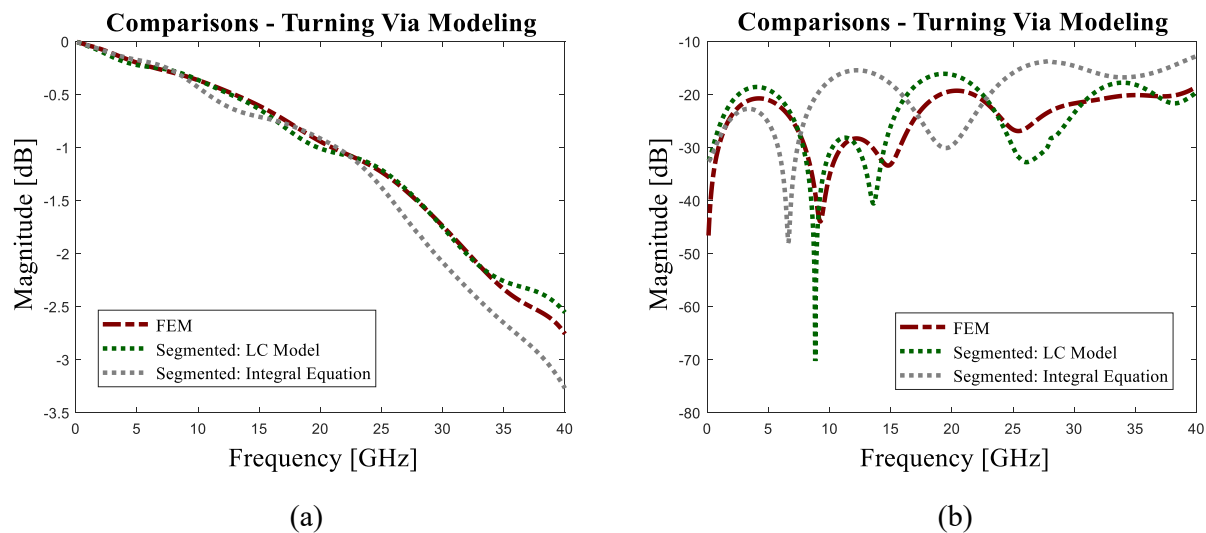


**Figure 3.19:** Comparison of scattering parameters for different modeling approaches of the structure shown in Figure 3.6, where all the cases presents acceptable agreement compared to the baseline case (FEM) for all the approaches. However, in case of return losses, a segmented modeling by considering a LC network for turning vias, reflects a better agreement compared with the FEM method.

some approximations to calculate the fringing capacitances of a via barrel crossing a metal plane. A method proposed in [6] uses an integral equation to calculate numerically these capacitances. Here, this method is going to be identified as Integral Equation. As shown in Figure 3.11, this additional method to compare provides a better understanding of the possible approach to extend and improve the turning via modeling, in order to propose a more accurate approximation. Thus, the LC model is considered in the comparison,

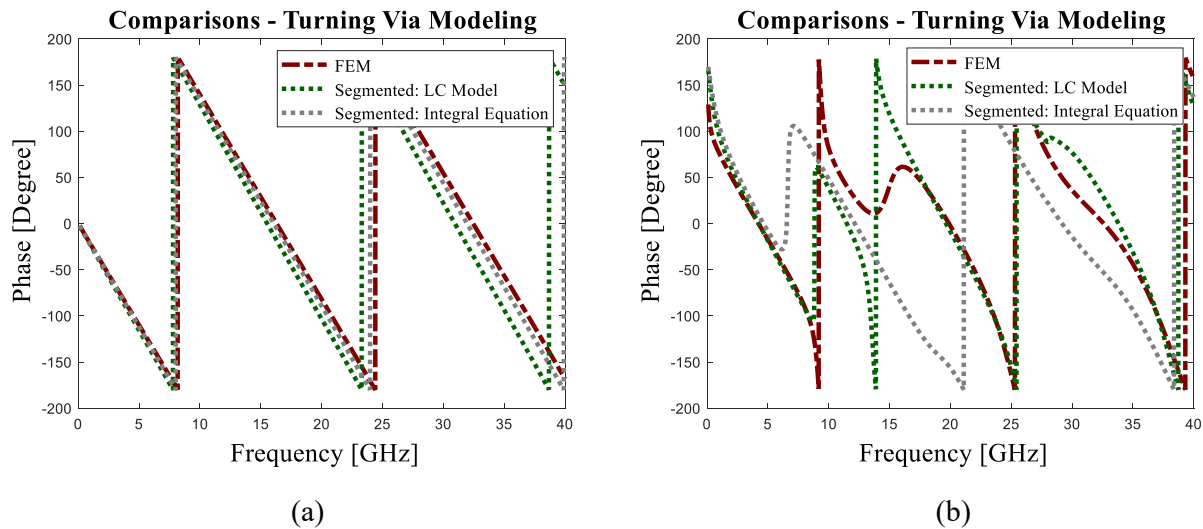


**Figure 3.20:** Phase parameter for same cases presented in Figure 3.19. In case of the phase response, as same as the scattering parameters, a modeling approach based on a LC networks is more suitable to represent the turning vias.

which is shown in Figure 3.19 and Figure 3.20. As it is possible to see, by combining an LC model different than the case in [6], which involves the consideration only of a capacitance, provides a better fitting for the insertion and return losses, as depicted in Figure 3.18 (a) and Figure 3.18 (b) respectively. The main variance for this simple case is presented mostly on reflections beyond 2.5 GHz. Besides, in Figure 3.20, it is depicted the analysis of the phase in case of the response for transmission and reflections as well. This can be observed in Figure 3.20 (a) and Figure 3.20 (b). Similarly, the main deviations are presented for return losses. Thus, it is corroborated that the LC model can describe accurately the turning vias. In this lane, the intention of this work is to represent this interconnection in a more appropriate and accurate way, which will be covered in the Chapter 4.

# Chapter 4

## Extension of Physics-Based Via Modeling for Microstrip Transitions

In some platform implementations, microstrip routing is commonly used in break-in,out sections, in particular, for thin PCBs. For instance, channel implementations for different memory technologies consider these types of surface routing, due to the high-density interconnects. In more recent technologies, the stripline routing is directly implemented because it inherently presents lesser losses rather than the microstrip lines. Regarding this case, the current physics-based modeling framework does not consider external cavity agents, such as transition vias, microstrip traces, microstrip differential signaling, etc, even though there exist approximations based on some individual analyses of the different interconnects and effects inside and outside the cavities. Therefore, this part of the work presents an extension of the physics-based modeling and its description, in order to include the approach in the current simulation framework, that may be useful for high-efficient simulations that include microstrip line traces connected to vias. The modeling approach is chosen from a comparative analysis of solutions proposed in the literature, inserting an equivalent circuit model in a generalized network structure.

Thus, based on the stated before, an analysis of some structures that include these types of external and internal agents is presented, and the definition of the electrical parameters which are the baseline statement of the modeling of each external agent. Furthermore, turning vias description is proposed based on the formulation in [26], which presents a via barrel crossing a metal plane and the calculation of the equivalent fringing capacitances of these interconnects, under non-homogeneous dielectrics. Besides, by complementing the modeling approach, a calculation of an inductance value as a function of the fringing capacitance based on filter design criteria is developed to create a complete modeling for turning vias description, based on the LC approach analyzed in Section 3.2.1.

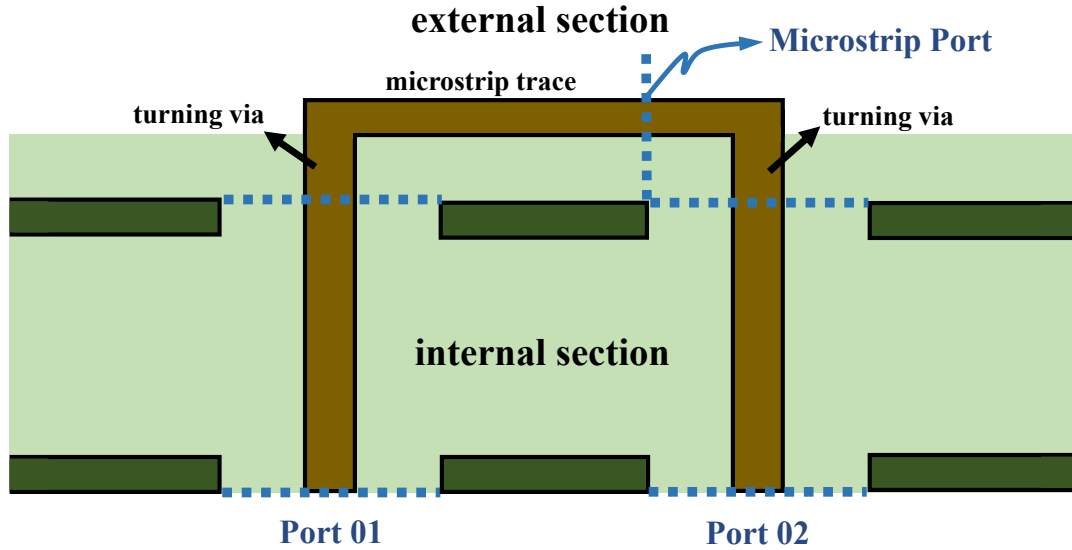


**Figure 4.1:** Configuration under analysis for the inclusion of microstrip ports in physics-based modeling. The topology includes the turning vias and microstrip traces, which are the external agents from the regular cavity modeling.

## 4.1 A Formulation of Physics-Based Via Modeling Including Microstrip Transitions

The analysis of the physics-based modeling with the inclusion of microstrip ports and via transitions is based on the configuration shown in Figure 4.1. As similar as in [32], a segmented approach that includes these agents can be integrated into the current modeling formulation. In this case, the Figure 4.1 depicts a cavity configuration with two signal vias embedded between the pair of metal planes, and these ones are connected to the microstrip trace, by the turning via interconnections. As shown in Chapter 3, these turning vias can lead to high-order modes propagation for a specific frequency ranges, due to non-uniform current distributions. This configuration is divided by two sections, such as the external and internal, where the formulation presented in this work tries to integrate both ones. In order to clarify conventions, the modes that propagate into the cavity are defined in the *internal* section, whereas the modes that propagate outside the cavity are identified in the *external* section. As it was described, the cavity modeling, defined in the *internal* section, is described as follows:

$$\begin{bmatrix} \bar{I}_i^{u'} \\ \bar{I}_i^{l'} \end{bmatrix} = \begin{bmatrix} \mathbf{Y}^{int} & -\mathbf{Y}^{int} \\ -\mathbf{Y}^{int} & \mathbf{Y}^{int} \end{bmatrix} \cdot \begin{bmatrix} \bar{V}_i^{u'} \\ \bar{V}_i^{l'} \end{bmatrix} \quad (4.1)$$

and  $i$  is the index of a specific via in the configuration and  $\mathbf{Y}^{cav}$  is defined by the near and far-field interactions:

$$\mathbf{Y}^{int} = \begin{bmatrix} Y^{cu} & 0 \\ 0 & Y^{cl} \end{bmatrix} + \begin{bmatrix} \mathbf{Y}^{pp} & -\mathbf{Y}^{pp} \\ -\mathbf{Y}^{pp} & \mathbf{Y}^{pp} \end{bmatrix} \quad (4.2)$$

The expression in (4.2) includes the entire effect into the cavity, such as the parallel-plate impedance, which describes the far-field propagation and coupling with other vias, and the near-field around each via barrel. The near-field interaction can be described by different approaches, such as the different ones analyzed in the Chapter 3. Also, as part of the modeling generalization, the stripline port and transmission lines definitions can be included in terms to consider the influence of the stripline mode propagating into the cavity, decoupled from the parallel-plate mode [32]. It is important to denote that the *internal* section does not present any electromagnetic interaction or coupling with the *external* section, and the defined ports in the Figure 4.1 would reflect all the electrical effects into the cavity that represent the interaction with the external agents. This is a well known effect caused by the skin effect on the metal planes, when the return current flow across the surface of these structures, and the interaction with the rest of agents happen through the defined electrical ports. These topics will be discussed in more details in next formulations. Following these statements, the *external* section can be expressed as following:

$$\begin{bmatrix} V_1^{ext} \\ V_2^{ext} \end{bmatrix} = \begin{bmatrix} \mathbf{Z}^{ext} & -\mathbf{Z}^{ext} \\ -\mathbf{Z}^{ext} & \mathbf{Z}^{ext} \end{bmatrix} \cdot \begin{bmatrix} I_1^{ext} \\ I_2^{ext} \end{bmatrix} \quad (4.3)$$

where the impedance matrix  $\mathbf{Z}^{ext}$  can be also expressed in terms of admittance parameters, defined as  $\mathbf{Y}^{ext} = \mathbf{Z}^{ext^{-1}}$ . This impedance matrix represents the relation between the vectors of current and voltage across all the exterior sections with regard to the cavity, which includes the microstrip trace and the pair of turning vias. The overall effect is conventionally identified in next formulations as external coupling. In that lane, in order to find out a description for each agent presented in the *external* section, an analysis of the microstrip transitions is considered here.

#### 4.1.1 Determination of a Modeling Approach for Turning Vias

It is been analyzed that, the microstrip transitions or turning vias, are part of the irregular cases where the current physics-based via modeling may be insufficient to represent accurately their behavior, as part of the developed physics-based approaches for efficient pre-layout simulations. This section deals with a proposal for a semi-analytical modeling of the turning vias based on the investigations in [7] and [26]. This work tries to contribute to the physics-based via modeling approach by proposing a method to calculate the lumped elements for the adequate modeling of the via transition, as explained in Section 3.2.1. In [7], it has been shown how a *T*-model is more suitable for modeling both sections (upper and lower) of a via crossing a metal plane. This *T*-model is basically a low-pass filter of second-order, which is composed by a pair of inductances and

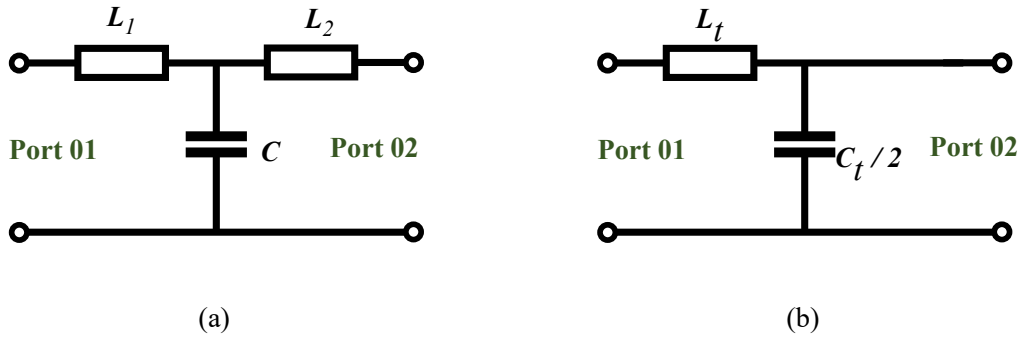


**Figure 4.2:** Modeling approaches for turning vias based on a via crossing a metal plane, by considering: (a) upper and lower sides, and (b) only one of the segments of the turning via, as shown in [7], where  $L_1 = L_2 = L_t$  and  $C_t = C/2$ .

a capacitance, where the experimental lumped values are extracted by using commercial tools, for different geometries and material parameters. However, it is appropriate to figure out a method to determine an analytical or semi-analytical approach to calculate these elements, as a function of these material and geometrical parameters as well. In this lane, Figure 4.2 depicts the  $T$ -model approach proposed for the turning vias, where are separated by for the upper and lower sides and the modeling for only one side, shown in Figure 4.2 (a) and Figure 4.2 (b), respectively.

In order to understand the effect of the modeling approach depicted in Figure 4.2 (b), in (4.4) is shown the  $Z$ -parameter matrix that is extracted through mesh equations. Basically, the system has not the property to be categorized as symmetrical, different than the case of Figure 4.2 (a) presented in [7]. The inductance and capacitance values are defined generically for a LC network, where the proposed modeling approach is described by this impedance matrix, where might be converted to  $Y$  or  $S$ -parameter matrix as needed. Furthermore, it is important to denote that, as mentioned, the system follows the behavior of a low-pass filter of second-order, where the transfer function (4.5) and cut-off frequency (4.6) follow the theory reported in literature.

$$\mathbf{Z}^{tr} = \begin{bmatrix} j\left(\omega L - \frac{1}{\omega C}\right) & -\frac{j}{\omega C} \\ -\frac{j}{\omega C} & -\frac{j}{\omega C} \end{bmatrix} \quad (4.4)$$

Similar as shown in [7], Figure 4.3 depicts the  $Z$ -parameters response of the LC network presented in Figure 4.2 (b). From there, it is possible to denote that the influence of each parameter is pretty similar compared with the network shown in Figure 4.2 (a) [7], where it is reflected in the imaginary part of the matrix entities. In this same way, by looking the network as a filter stage, the transfer function can be defined in frequency domain, by considering the Port 1 and 2 as input and output respectively, as:

$$H(\omega) = \frac{1}{1 - \omega^2 LC} \quad (4.5)$$

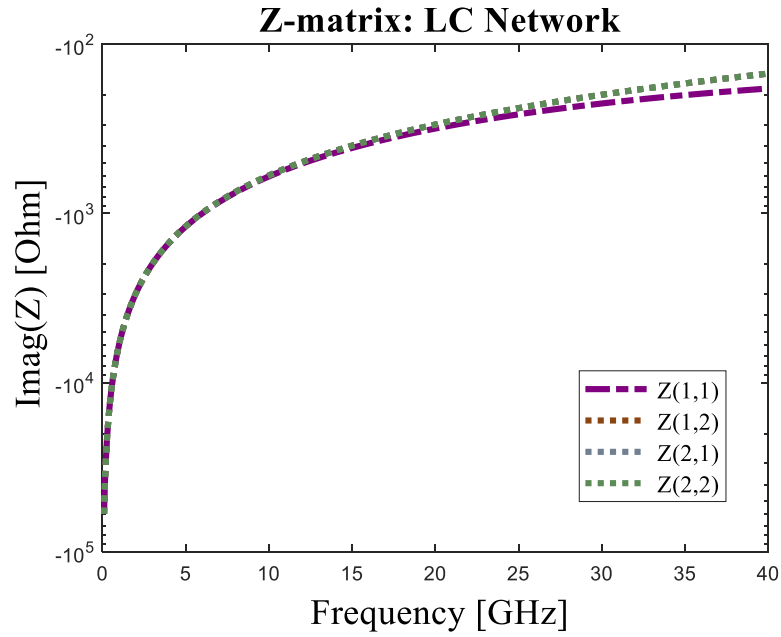


**Figure 4.3:** Frequency response of the Z-parameters of the network shown in Figure 4.2 (b) for  $C_t = 53.4$  fF and  $L_t = 133.5$  pH. The LC network influence is mostly given by the imaginary part of each matrix entity, and defines the behavior of the modeling stage.

where the cut-off frequency is defined as following:

$$\omega_0 = \frac{1}{\sqrt{LC}} \quad (4.6)$$

In [26], it is investigated a numerical method to extract the fringing capacitances for a via crossing a metal plane in homogeneous and non-homogeneous dielectric media, based on an integral equation for surface charge density. Specifically, for the purposes on this work, the case of non-homogeneous dielectric is considered in terms of the calculation on the fringing capacitances for the turning via modeling. Moreover, for validation purposes, an specific geometry is used for the analysis of the modeling approach presented here. Thus, by defining a via radius of 5 mil, antipad radius is 15 mil, and a pad radius of 10 mil, a fringing capacitance calculation based on [26], is around 53.4 fF. A good rule of thumb for filter modeling, and according to circuits theory, the characteristic impedance of a LC network is given by:

$$Z_0 \approx \sqrt{\frac{L_{total}}{C_{total}}} \quad (4.7)$$

where, by assuming a characteristic impedance of 50 Ohms, it is possible to calculate the inductance of the system. For this specific case, the inductance value is around 133.5 pH as well, and the Z-parameters for these values are shown in Figure 4.3. Of course, it is possible to obtain a more detailed analysis for this inductance value, since it is based on a very simple approximation and with the assumption that the structure

has an impedance matching, which is not the case in multiple scenarios. However, this inductance calculation can be useful to obtain a low frequency approximation for these type of structures that involve external and internal sections. This modeling approach for microstrip transitions can be part of the interconnection layer as the framework explained in [1]. Thus, all the agents and topologies presented on the integration of the *external* and *internal* sections are described already, where this integration itself is described in next section. and presents the basic concepts of the considerations of the actual physics-based via modeling by including these external formulations.

### 4.1.2 Analytical Formulation for Microstrip Ports Description

The extension of physics-based modeling that includes the microstrip ports can be achieved by analyzing the structure and electrical parameters of each section. The purpose of this analysis is to formulate the effect of the external section in terms of admittance or impedance forms, which can be concatenated with the current cavity modeling approaches by using segmentation techniques, where the resultant model considers the overall effects, and can be described in terms of S or Y-parameters. Thus, the Figure 4.4 presents the main configuration that will be the baseline for the analysis, and as different as the Figure 4.1, this one depicts all the electrical parameters that will be considered in the formulation, but the description will also be specified for the microstrip ports. In order to do that, some constraints will be defined and applied to reduce the dependence of the parameters, as it is depicted with the reduction of the brightness in the Figure 4.4, where the general formulation would be defined without the consideration of the electrical parameters of that via and effects section.

First of all, the configuration presents two signal vias into a cavity, connected by a microstrip line trace. Each signal via, indexed as 1 and 2, are described by the current and voltage parameters, which are related by the corresponding admittance or impedance equivalence of the cavity. These parameters are separated by defining the upper and lower segments. Thus, *internal* section parameters can be described with the following vectors:

$$\bar{I}^{u'} = \begin{bmatrix} I_1^{u'} \\ I_2^{u'} \end{bmatrix} \quad \bar{I}^{l'} = \begin{bmatrix} I_1^{l'} \\ I_2^{l'} \end{bmatrix} \quad (4.8)$$

$$\bar{V}^{u'} = \begin{bmatrix} V_1^{u'} \\ V_2^{u'} \end{bmatrix} \quad \bar{V}^{l'} = \begin{bmatrix} V_1^{l'} \\ V_2^{l'} \end{bmatrix} \quad (4.9)$$

Regarding the description of the *external* section, the current and voltages are correlated by a contribution of various agents. As it was described, the external section contains the microstrip trace and the turning vias so, the voltage vector should consider the contribution of both ones in each side, where these voltages are referred to the upper metal planes. In case of the electrical current parameter, rather than define contributions, the current flowing out would be the same for all the agents, with the consideration of the directions

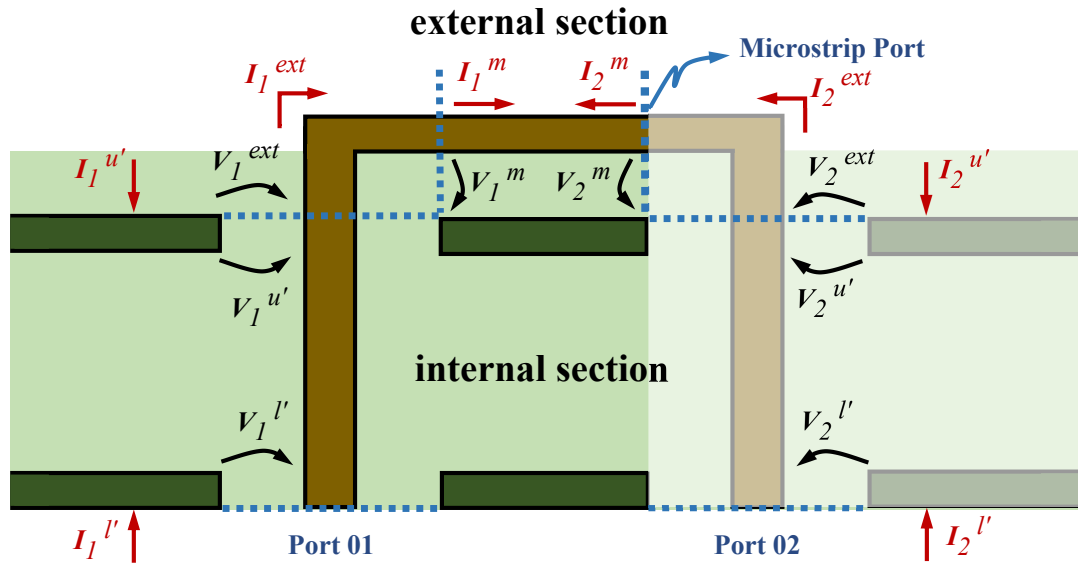


**Figure 4.4:** Representation of the case under analysis, including the electrical parameters for each agent in *external* and *internal* sections. The analysis covers all the structure parameters, but constraints are applied in order to reduce the case of study for the electrical description of microstrip ports.

defined by the nomenclature. Now, it is important to analyze the current distribution at the electrical port interface, between the *internal* and *external* sections. As it is shown in the Figure 4.5, there exist three different currents that are involved in the node under analysis, where also defines the  $\bar{I}^{cav}$ . Applying the KCL, it is possible to define that:

$$i_{ext} = -i_u = i_l \quad (4.10)$$

An explanation about (4.10) can be addressed as when a current is excited at the microstrip port, it flows out across the external section, and at the analyzed junction, it would be described by the upper and lower cavity currents, which are defined in the current physics-based approach. These parameters define the cavity current parameter as well, and as it was explained, this confirms the statement that the *external* and *internal* sections only have influence and interaction between each other through the electrical ports. Extending the relation in (4.10), the relation can describe the parameters defined in Figure 4.5 as following:

$$\bar{I}^{ext} = -\bar{I}^{u'} = \bar{I}^{l'} \quad (4.11)$$

The expression in (4.11) is the first to describe the integration of the *external* and *internal* sections. Besides, in terms of the segmentation techniques, it is one of most important constraints to define the electrical continuity of the ports, where addresses the definition of the currents across the ports connected to each other, in this case between the *internal* and *external* sections. Thus, a collection of equations can be gathered in order to figure out an electrical equivalent formulation. For instance, according to the Figure 4.5, the

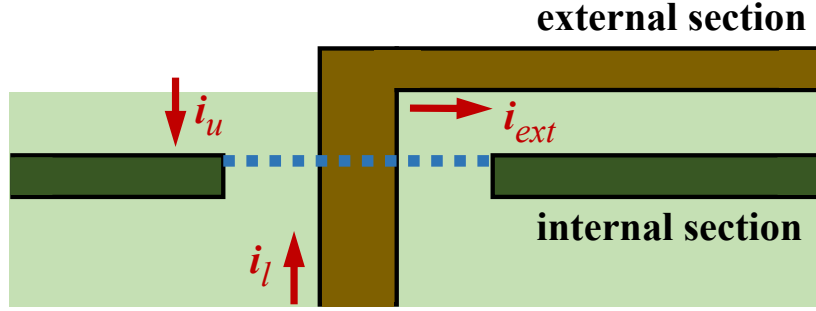


**Figure 4.5:** Upper segment of the case under study. The current coming from the microstrip trace is divided in the upper and lower cavity currents. This KCL analysis allows to correlate directly electrical parameters between exterior and internal sections.

*external* section is composed by the microstrip trace and a pair of turning vias. This external configuration is directly connected to a cavity model that includes two signal vias. First, it is relevant to define an expression for this *external* section in terms of Y-parameters, which is described by:

$$\bar{I}^{ext} = \mathbf{Y}^{ext} \cdot \bar{V}^{ext} \quad (4.12)$$

for a 2-port network configuration, which is a function of the voltage and equivalent admittance matrix of the exterior section, expressed as follows:

$$\begin{bmatrix} I_1^{ext} \\ I_2^{ext} \end{bmatrix} = \begin{bmatrix} \mathbf{Y}^{ext} & -\mathbf{Y}^{ext} \\ -\mathbf{Y}^{ext} & \mathbf{Y}^{ext} \end{bmatrix} \cdot \begin{bmatrix} V_1^{ext} \\ V_2^{ext} \end{bmatrix} \quad (4.13)$$

Above equations, i.e. (4.1) and (4.13), introduce the relations for the *internal* and *external* parameters, where both expressions address the integration of the *internal* section in (4.1) with the *external* section described by (4.13). For both sections, it is important to denote that several topology cases can be included, such as striplines ports and transmission lines, short-circuited vias, coupling between different vias, etc. In case of the external sections, the proposed approach is limited to include turning vias, as well as microstrip lines with the quasi-TEM modes that defines its propagation. By considering the topology depicted in Figure 4.4, some constraints need to be applied in order to express the relations in terms of the electrical parameters for the microstrip ports. The analysis about the first constraint applied to the formulation is based to the voltage across the signal via identified by  $i = 2$ , which is the right one. This via is described by the voltages  $V_2^{u'}$  and  $V_2^{l'}$ . The scattering effects of this via should be discarded so, for that reason, the propagated modes into the cavity must be short-circuited. In this way, it is possible to obtain access to the electrical parameters of the microstrip line without the influence of the signal via at the right side. Thus, the first constraint is defined as:

$$V_2^{u'} = V_2^{l'} = 0V \quad (4.14)$$

Besides, the second constraint that should be defined has to deal with the access to the electrical parameters at the microstrip port. This suggests that, the parameters  $\bar{V}^{ext}$  and  $\bar{I}^{ext}$ , would be described as a function of  $V_2^m$  and  $I_2^m$ , respectively. Similar as the case in [32], the external section, i.e. microstrip line and turning vias, connected to vias in both sides, defines the following:

$$V_2^{tr} = 0V \quad (4.15)$$

However, it is important to mention that the first constraint is still valid, and under these conditions, a direct access to the electrical parameters at the microstrip port can be obtained. These constraints allow to dismiss the effects of the cavity mode overall of the signal via at the right side, and are based on the baseline definition of the electrical ports. In this way, the descriptions and parameters for the *internal* and *external* sections are defined, where the Figure 4.4 presents an overall of both sections and the respective integration. Both sections are described by their respective electrical port parameters. However, it is important to analyze the different agents presented in the *external* section. As mentioned before, this section is composed by a turning via and a microstrip line, where both ones are well defined in literature [36]. In terms to define a description that concatenates the microstrip line and the turning via, a simple way is to treat the configurations by using ABCD-parameters, where allows an easier way correlates both agents at the *external* section. Thus, the expressions (4.16) and (4.17) are used to describe both sections, the microstrip line and via transition, respectively.

$$\begin{bmatrix} V_1^m \\ I_1^m \end{bmatrix} = \begin{bmatrix} \cosh(\gamma l) & Z_0 \cdot \sinh(\gamma l) \\ \sinh(\gamma l)/Z_0 & \cosh(\gamma l) \end{bmatrix} \cdot \begin{bmatrix} V_2^m \\ I_2^m \end{bmatrix} \quad (4.16)$$

$$\begin{bmatrix} V_1^{tr} \\ I_1^{tr} \end{bmatrix} = \begin{bmatrix} 1 + Y_C Z_{L_1} & Z_{L_1} + Z_{L_2} + Y_C Z_{L_1} Z_{L_2} \\ Y_C & 1 + Y_C Z_{L_2} \end{bmatrix} \cdot \begin{bmatrix} V_2^{tr} \\ I_2^{tr} \end{bmatrix} \quad (4.17)$$

The advantage of the using of ABCD-parameters is, in order to concatenate the model of the microstrip line and  $T$ -model of the transition, only necessary to multiply the matrices between each other, and can be used to include more effects inherently, such as coupling from other microstrip traces, crosstalk, etc., that might be investigated as future work. This is important since, modern platforms topologies have a thousands of traces in their implementations, and the consideration of all these effects lead to more accurate modeling descriptions. Thus, a representation for the *external* section is achieved, which was introduced in (4.13). In that lane, the following expressions depict a complete description for the *external* section, and correlate the electrical parameters for each port, i.e.  $V_1^{tr}$ ,  $I_1^{tr}$ ,  $V_2^m$ , and  $I_2^m$ :

$$\begin{bmatrix} V_1^{tr} \\ I_1^{tr} \end{bmatrix} = \begin{bmatrix} A_{ext} & B_{ext} \\ C_{ext} & D_{ext} \end{bmatrix} \cdot \begin{bmatrix} V_2^m \\ I_2^m \end{bmatrix} \quad (4.18)$$

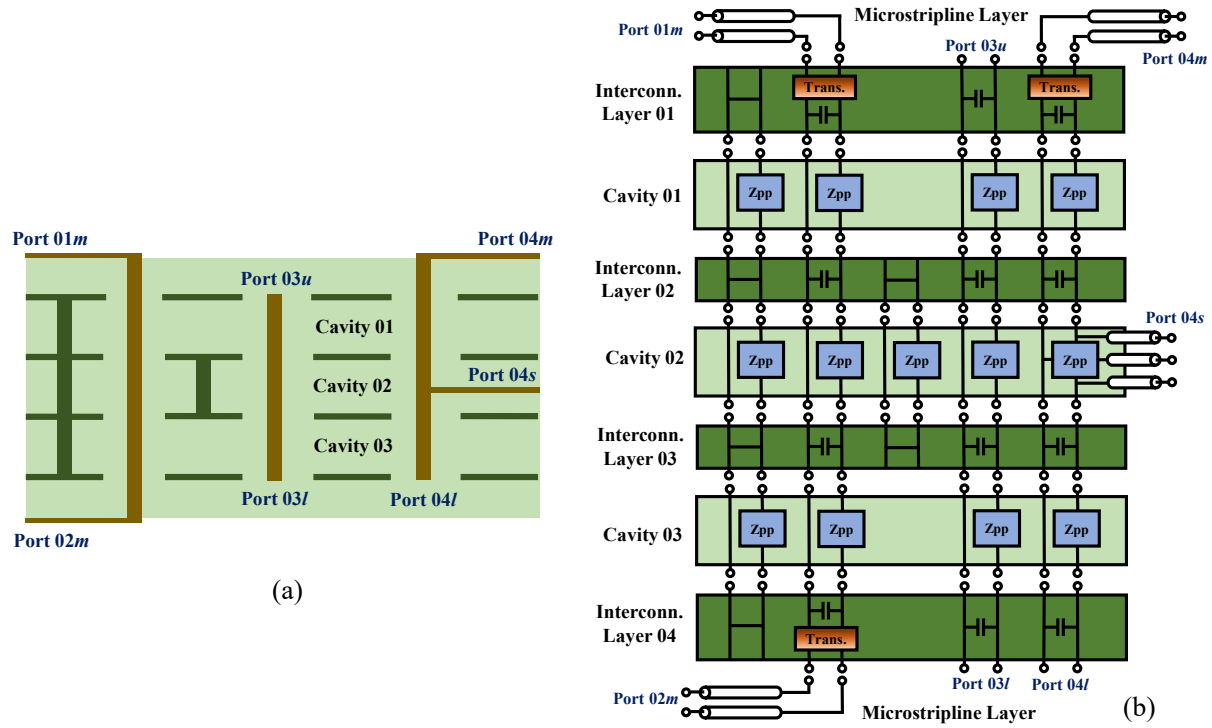


**Figure 4.6:** Segmented modeling proposed in [1] for a general stackup configuration shown in (a). The *external* section is a contribution of the turning via and the microstrip line depicted in the Microstrip Transition Layer, which formulates the  $\mathbf{Y}^{ext}$  parameter. (b) By using segmentation techniques [9], the entire effect is obtained and described as a single matrix, by including the all effects into the cavities, such as a via short-circuited to metal planes, transmission lines, stripline ports, etc.

where the matrix entities are defined as:

$$A_{ext} = \cosh(\gamma l) \cdot (1 + Y_C Z_{L_1}) + Y_C Z_0 \cdot \sinh(\gamma l) \quad (4.19)$$

$$B_{ext} = \cosh(\gamma l) \cdot (Z_{L_1} + Z_{L_2} + Y_C Z_{L_1} Z_{L_2}) + Z_0 \cdot \sinh(\gamma l) \cdot (1 + Y_C Z_{L_2}) \quad (4.20)$$

$$C_{ext} = (\sinh(\gamma l)/Z_0) \cdot (1 + Y_C Z_{L_1}) + Y_C \cdot \cosh(\gamma l) \quad (4.21)$$

$$D_{ext} = (\sinh(\gamma l)/Z_0) \cdot (Z_{L_1} + Z_{L_2} + Y_C Z_{L_1} Z_{L_2}) + \cosh(\gamma l) \cdot (1 + Y_C Z_{L_2}) \quad (4.22)$$

Once the expression in (4.18) is obtained, it can be converted to Z, S or Y-parameters and obtain the entire response of the system. Actually, the *external* section might be able to describe more agents, similar to the Figure 3.12, where it is depicted a pair of turning vias and a microstrip line trace. In that case, the methodology explained before is suitable to include those additional agents. Now, the expression in (4.18) can be integrated or

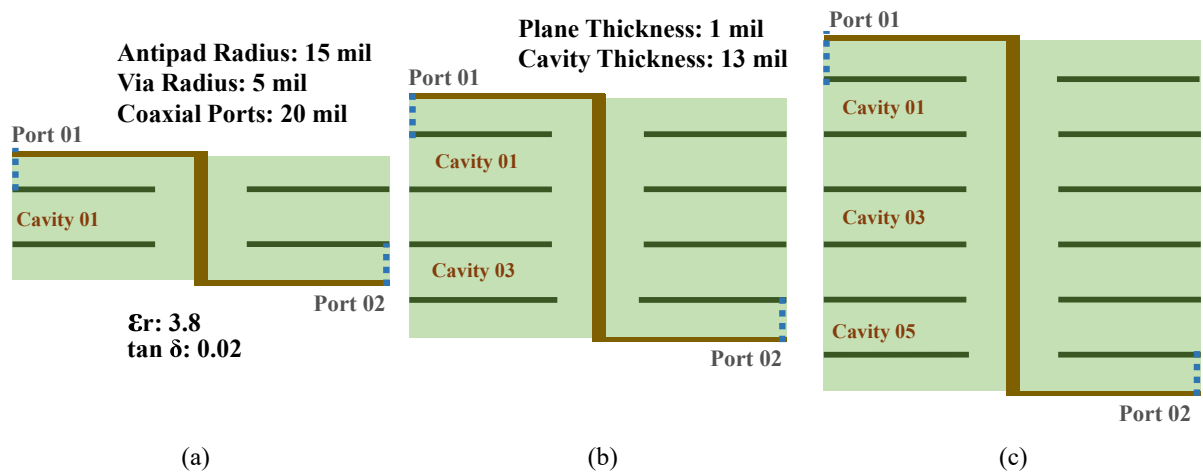


**Figure 4.7:** Different stackup structures for the modeling approach validations. Each one has the difference in the number of cavities that is the stackup composed: (a) 1-cavity stackup, (b) 3-cavities stackup, and (c) 5-cavities stackup. Similar as the configuration shown in Figure 3.6, ground vias distance are 40 mil.

concatenated with the *internal* section, described in (4.1), by considering the conversion of (4.18) to Y-parameters, and applying segmentation techniques described in [9].

Thus, in order to exemplify a more realistic case, Figure 4.6 (a) shows a configuration where several signal and ground vias are presented, as well as some different types of transmission lines inside and outside the cavities. This topology can be described by using the same methodology explained before, in case to include the microstrip ports, i.e. *Port01m*, *Port02m*, and *Port04m*. The entire structure can be segmented by following the same methods shown in [1], where the Interconnection and Cavity Layers can be defined as shown in Figure 4.6 (b). As depicted, the modeling related to the turning vias, identified in orange as *Trans.*, can be included as part of the external Interconnection Layers, and then connected to the microstrip lines. Basically, this same methodology has been quite used on the physics-based via modeling framework, which has used and proved the efficiency of this approach. In this lane, different validation scenarios are defined for exercise the modeling approach and find out the viability of the proposal, where the description of the turning vias presented in Section 4.1.1 is considered. Thus, in the Figure 4.7 the defined validation cases are presented: (a) 1-cavity stackup, (b) 3-cavities stackup, and (c) 5-cavities stackup. Similar as before, the comparison of the modeling proposal is against the baseline method, i.e. FEM, and the validation is developed by analyzing the scattering parameters in terms of the response of magnitude and phase in frequency domain, which provides a sense of the time-domain response as well. Also, all the geometrical and material parameters are depicted in the Figure 4.7. The validation results for the Figure 4.7 (a) are shown in Figures 4.8 and 4.9, for Figure 4.7 (b) in Figures 4.10 and 4.11, and for Figure 4.7 (c) in Figures 4.12 and 4.13, where each pair shows the response in terms of magnitude and phase, respectively. The intention is to analyze the influence on number of cavities of a generic stackup on the modeling approach and simulation cases.

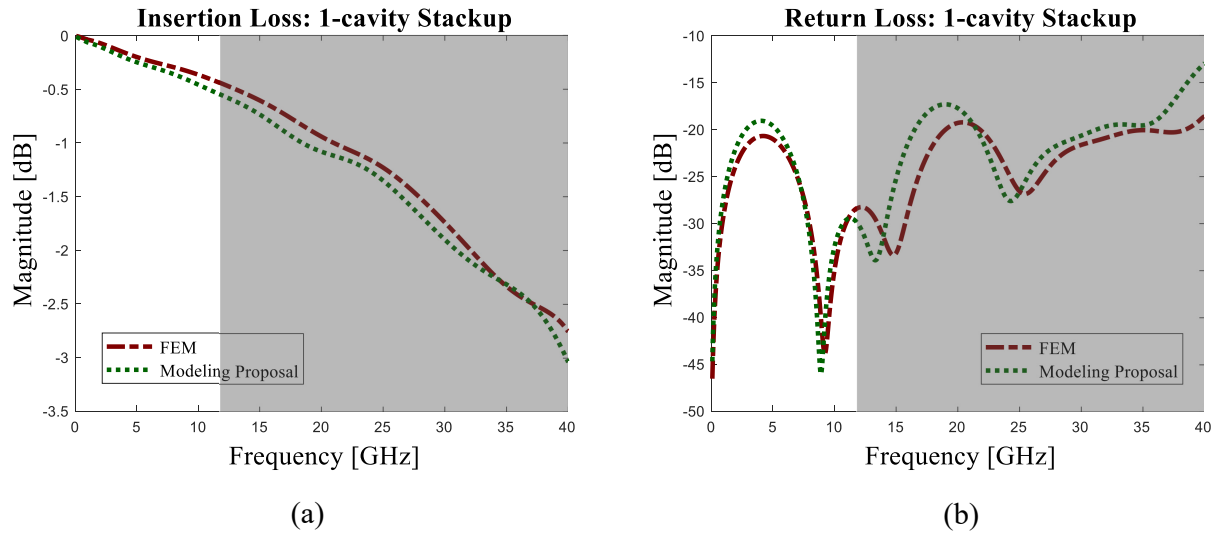


**Figure 4.8:** Scattering parameters for the 1-cavity stackup shown in Figure 4.7 (a). It is depicted the response for (a) insertion and (b) return losses. A good agreement is achieved up to around 12 GHz.

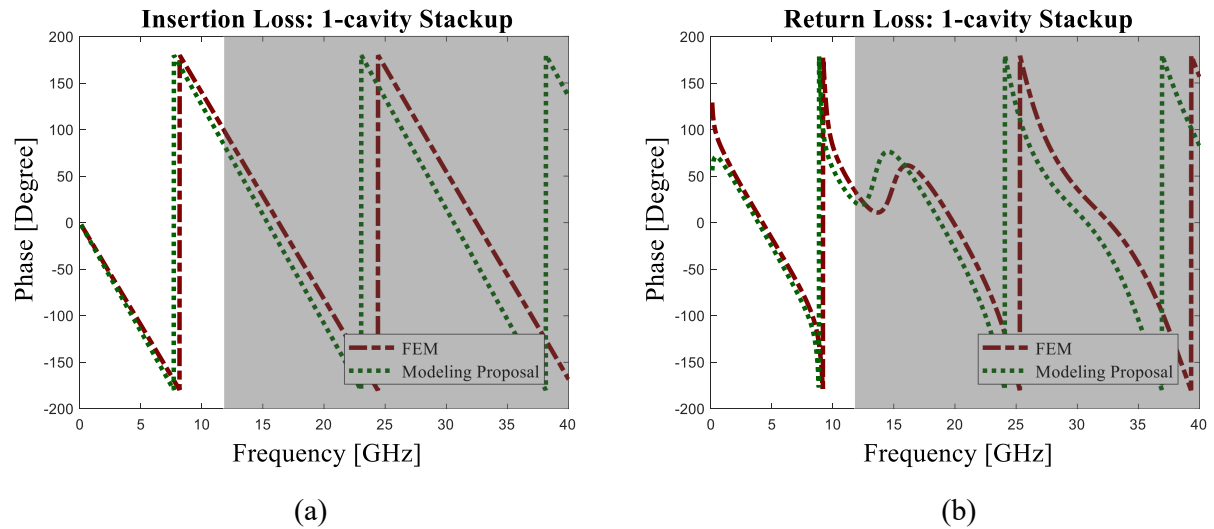


**Figure 4.9:** Phase parameters for the 1-cavity stackup shown in Figure 4.7 (a). The responses are for (a) insertion and (b) return losses, where the agreement in terms of frequency ranges is quite similar compared to the scattering parameters.

As mentioned in Section 2.2.1, turning vias excites high-order modes because of the non-uniform current distribution across the via barrel, and the calculations of the modeling approach are based on a distributed charge density and the lumped elements do not have frequency dependencies, which could address for inaccuracies of the modeling mostly at high frequencies. In fact, these statements can be confirmed on the validation figures, where an acceptable agreement is shown on the non-shadowed graph sections, which is a frequency range up to around 12 GHz. Furthermore, it is relevant to analyze the different cases and configurations for the turning vias, since the charge density may be axially different when the current distribution comes from a microstrip line or a regular cavity, due

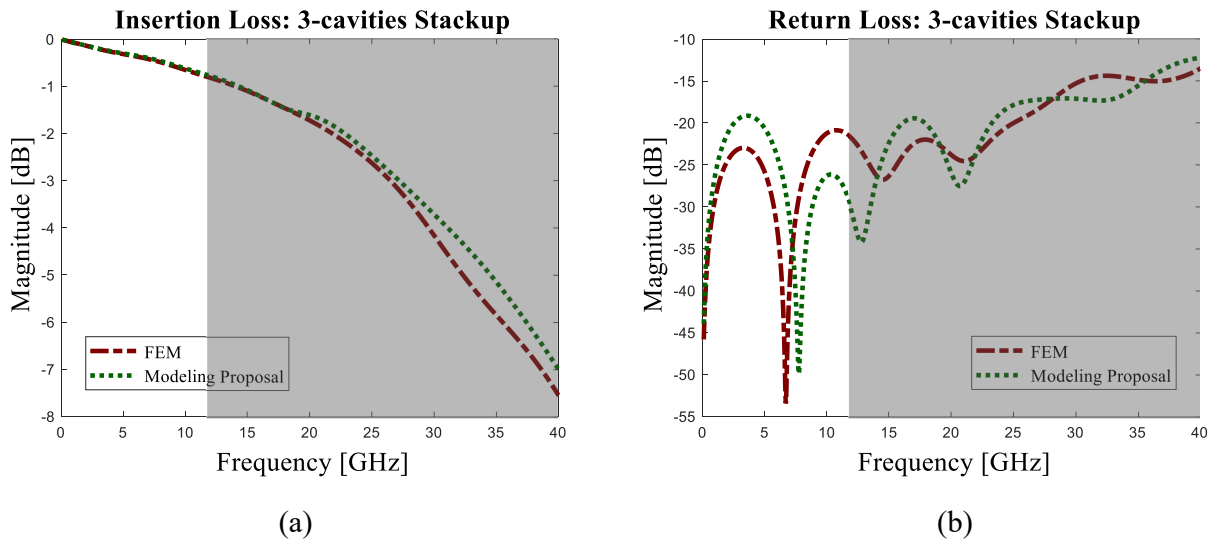


**Figure 4.10:** Scattering parameters for the 3-cavities stackup shown in Figure 4.7 (b). It is depicted the response for (a) insertion and (b) return losses. The agreement of this case seems to be some worst compared to 1-cavity and 5-cavities stackup.

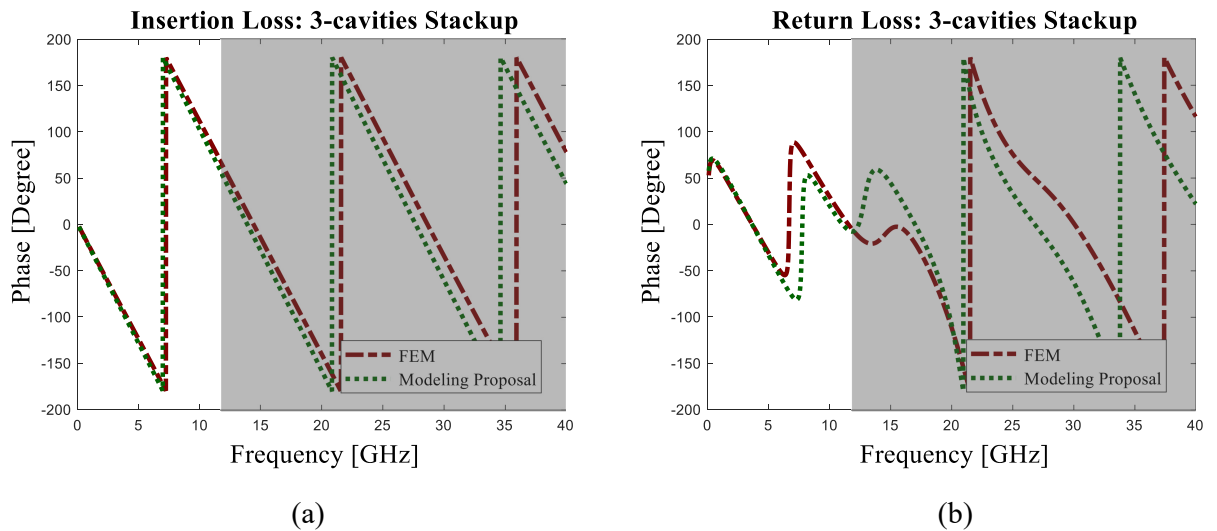


**Figure 4.11:** Phase parameters for the 3-cavities stackup shown in Figure 4.7 (b). The response for (a) insertion and (b) return losses is presented.

to the differences on the electromagnetic modes propagated in each case, i.e. quasi-TEM and fundamental modes, respectively. Thus, a generalization of the field distribution as a function of the charge density is part of the topics for further investigations, which would improve the modeling accuracy. However, the approximation proposed here presents a good agreement in terms of insertion losses even up to high frequencies, rather than the frequency limitation for return losses, where a relative deviation up to -5 dB is identified compared with full-wave method. In case of the phase response, the agreement is better for all the cases with important deviations at high frequency ranges, but a good one up to around 12 GHz is presented. In case of the number of cavities, there is no a huge difference across validations.

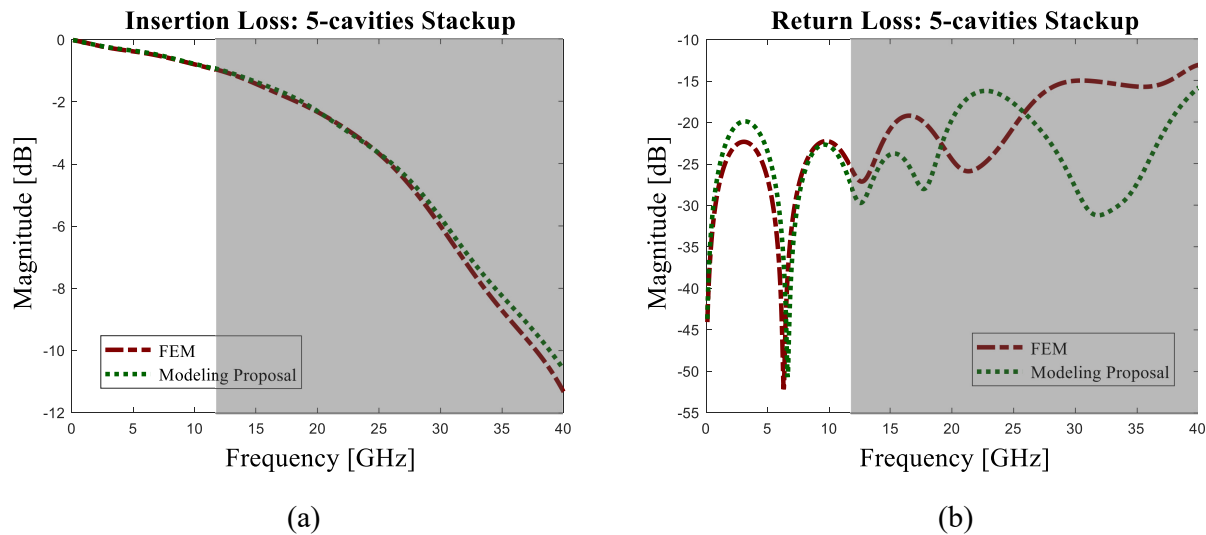


**Figure 4.12:** Scattering parameters for the 5-cavities stackup shown in Figure 4.7 (c). It is depicted the response for (a) insertion and (b) return losses. Similarly as the case of 1-cavity stackup, a good agreement is achieved up to around 12 GHz.

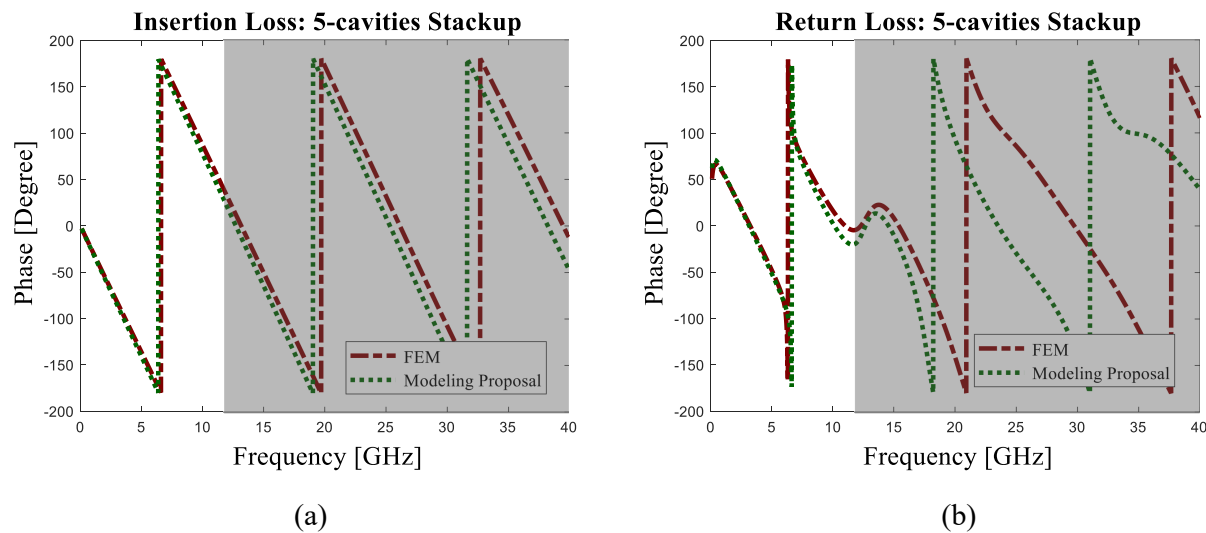


**Figure 4.13:** Phase parameters for the 5-cavities stackup shown in Figure 4.7 (c). It is shown the parameters for (a) insertion and (b) return losses. As similar to the scattering parameters, a good agreement is achieved up to around 12 GHz.

Additionally, it is relevant to analyze also the influence on the modeling by different return vias distances. The validation cases shown in Figure 4.7 are based on the case of study depicted in Figure 3.6, where two ground vias are placed in a distance of 40 mil from the signal via. Here, a comparison on the agreement by considering the stackup configuration depicted in Figure 4.7 (c) is presented, with the ground via placement defined as 30 and 50 mil. This is shown in Figure 4.14 and 4.15, respectively. It is evident that the case when the ground vias are closer to the signal via (Figure 4.14) the agreement at high frequencies improves, by achieving up to around 17 GHz, different than the case in Figure 4.15, where deviations below to 10 GHz are presented. All these variations are

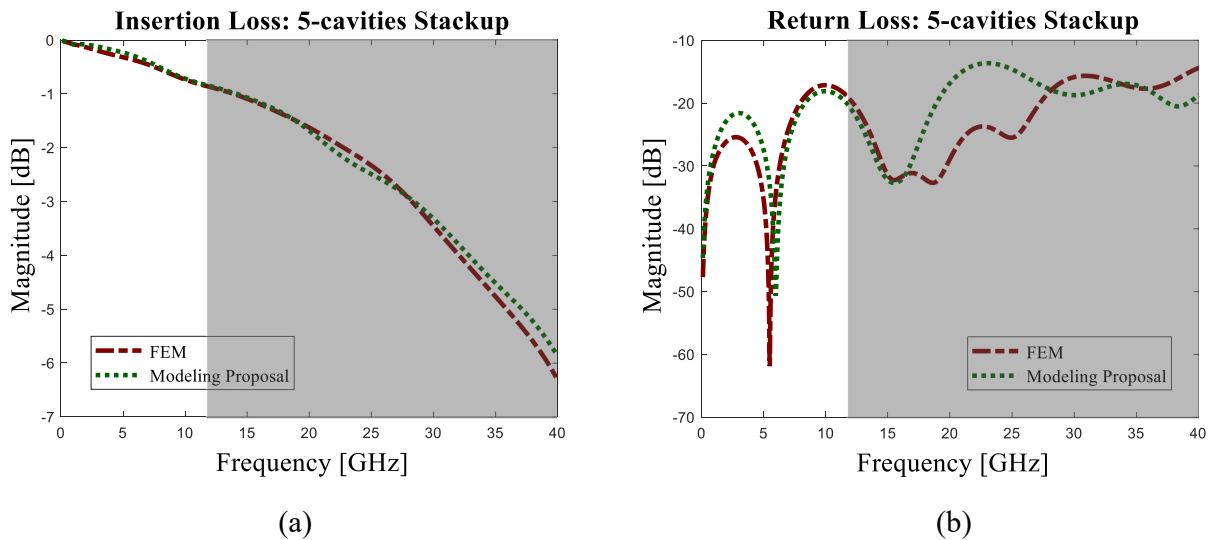


**Figure 4.14:** Scattering parameters for the 5-cavities stackup shown in Figure 4.7 (c) and the ground via distance of 30 mil. The (a) insertion and (b) return losses are shown, and the agreement even up to 15 GHz by improving the return path performance.

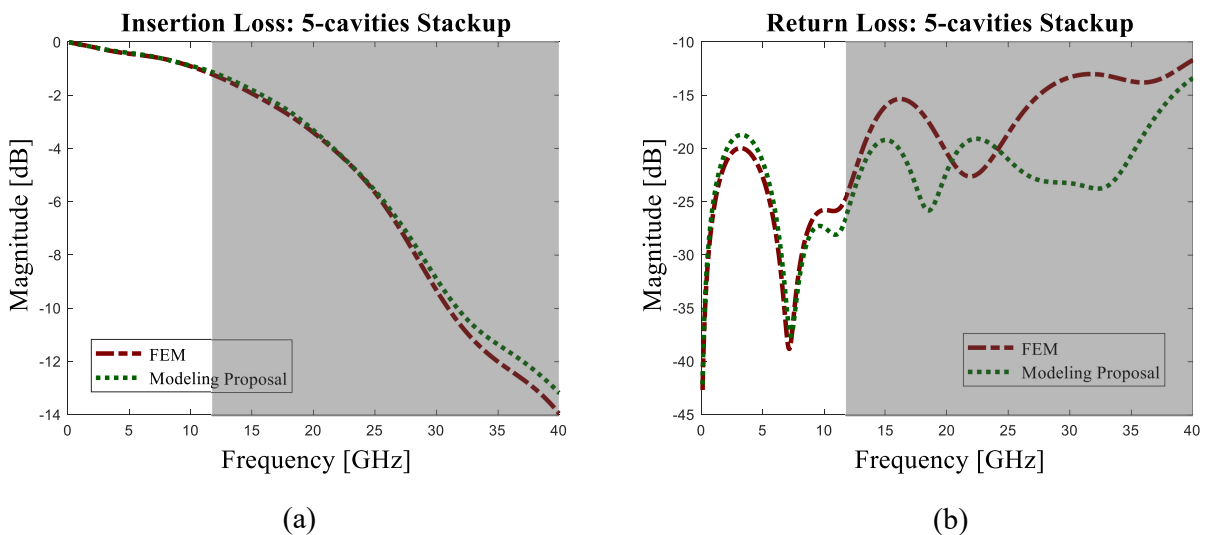


**Figure 4.15:** Scattering parameters for the 5-cavities stackup shown in Figure 4.7 (c) and the ground via distance of 50 mil. Difference at the case of 30 mil distance, the accuracy is reduced even for frequencies below to 10 GHz.

related to return losses, since the insertion losses are not depicting a relevant variance. The validations cases are considering scenarios when a single signal arrives to channel discontinuities, defined by all the sections (microstrip lines, turning vias, etc.). Similar validations can be applied for scenarios that include differential signaling, dense via arrays, etc., but the modeling approach should need to consider a better description for high-frequency ranges, since there is involved coupling across traces and vias that affects the performance of the interconnection. In order to do that, some viable improvements for the calculation of the inductance value can be investigated, as part to the intention to improve the high-frequency ranges model fitting. Also, the cases when a turning via co-

exists at upper or lower of the cavity section, can be analyzed as well, where the case of the current distribution at the time the signal arrives to the discontinuity, might be different and present different field distributions across turning via implementations.

# Chapter 5

## Analysis of Mode Conversion Due to Asymmetrical Via Stubs

The increase of data rates in digital systems has made the design of printed-circuit boards more challenging, since high frequency effects start to play a more important role, such as material losses, impedance mismatches, crosstalk, and mode conversion. Differential signaling is a convenient approach for crosstalk reduction and immunity to common-mode noise. However, non-idealities in geometries and signaling lead to differential-to-common-mode conversion. Several mechanisms that introduce mode conversion are well known, such as skew caused by asymmetrical configurations and unbalanced differential signals [41] from the IC transmitter, which compromise the electrical performance of the link and cause undesired EMI radiations. Also, the manufacturing process deals with inherent effects that affect directly the performance of high-speed applications, and an estimation of some of these effects is appropriate to consider in pre-layout stage to avoid EMC issues. The effect analyzed here refers to the mode conversion due to residual via stubs, which has not been previously addressed in the literature.

In case of differential signaling, the differential to common-mode conversion is a typical issue to be avoided. This effect affects directly the signal integrity, since part of the energy used for the information signaling is converted on ground noise. A well known source of mode conversion are the interconnection asymmetries across the signals of the differential pair. For instance, several sources of mode conversion have been analyzed in literature, such as differential pair length mismatching, asymmetrical ground vias configurations, etc. [41]. All these sources of mode conversion can be prevented in pre-layout design and manufacturing process. However, it is impossible to avoid these effects completely, and every differential link has to deal with mode conversion losses. Thus, the analysis of limitations and inherent effects on manufacturing process is important on pre-layout stage. The Figure 5.1 depicts a configuration that presents asymmetrical via stubs. Tolerances on manufacturing process can result of around 10 mil so, it is an important effect that are present in modern implementation. As shown in Figure 5.1, the parameter  $\Delta l_{stub}$  is the source of the mode conversion, which represents the asymmetry between both stub

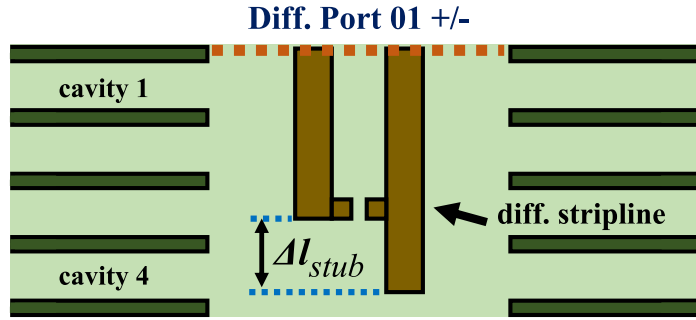


**Figure 5.1:** Asymmetrical via stubs in a differential pair - cross sectional view. The difference  $\Delta l_{stub}$  deals with differential to common-mode conversion. Differences in range of back-drilling tolerances can generate important amounts of this loss.

lengths. In this way, asymmetrical via stubs sharing an antipad would lead to excite parasitic modes as well as mode conversion. These types of coupling are not actually considered in physics-based modeling. As a first best approximation from the author's knowledge, an extension from the approaches in [42] and [43] can deal with good modeling agreement. In case of the analysis of mode conversion due to via stubs, an approximation for low frequency ranges is proposed here, based on a first-order low-pass filter that estimates the magnitude of this effect as a function of the residual stub length.

## 5.1 Investigation of Mode Conversion Due to Asymmetrical Via Stubs

As mentioned, several sources of mode conversion in differential links have been analyzed in literature, such as asymmetric ground via placement configurations, differential pair length mismatching [41], among others. The design and manufacturing of printed circuit boards plays an important role to minimize the detrimental effects on the signals at high frequencies, since multiple processes on those stages have their respective tolerances and inherent effects, and can be the root cause of electromagnetic compatibility issues. For instance, plated through-hole (PTH) vias are widely used due to their low cost and the ease of manufacturing. However, these vias can introduce stubs which affect directly the transmission, by adding undesired resonances at certain frequencies [44], [45]. Thus, back-drilling processes are used to remove these stubs, and depending on the tolerance of the process, residual stubs can remain [46]. In this case, these residual via stubs might be analyzed in order to explore the influence on the mode conversion in differential signaling. The geometry investigated to explore the mode conversion is shown in Figure 5.2, where a differential link is built with an 8-cavity stackup with a 15 mil of dielectric thickness per cavity. A differential stripline trace with a length of 200 mil connects to the other end of the differential via pair. The via radius is 5 mil and the antipad radius is 15 mil as well. Absorbing boundary conditions are defined in order to avoid reflections from the

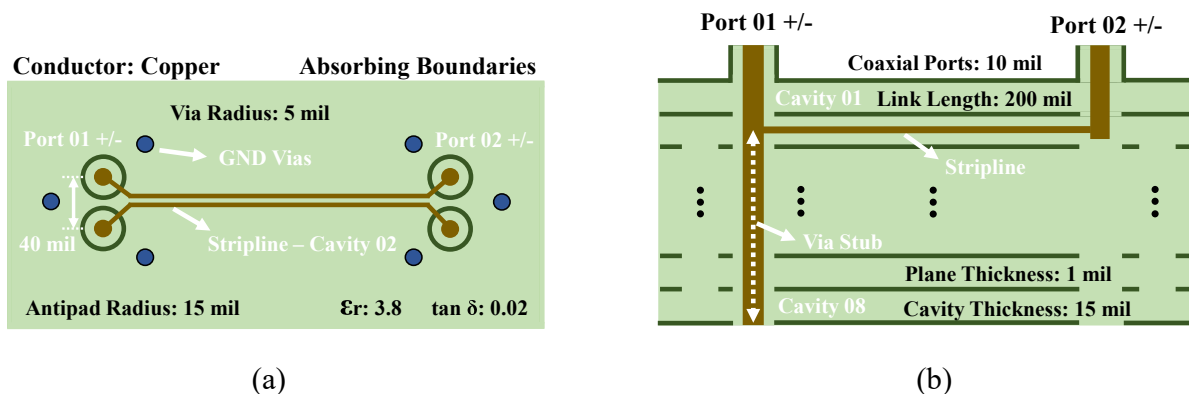


**Figure 5.2:** Differential via-to-via configuration: (a) top and, (b) side view. Differential stripline traces are routed on cavity 2 and via stub length on port 01 (-) has been varied to analyze the effect on mode conversion.

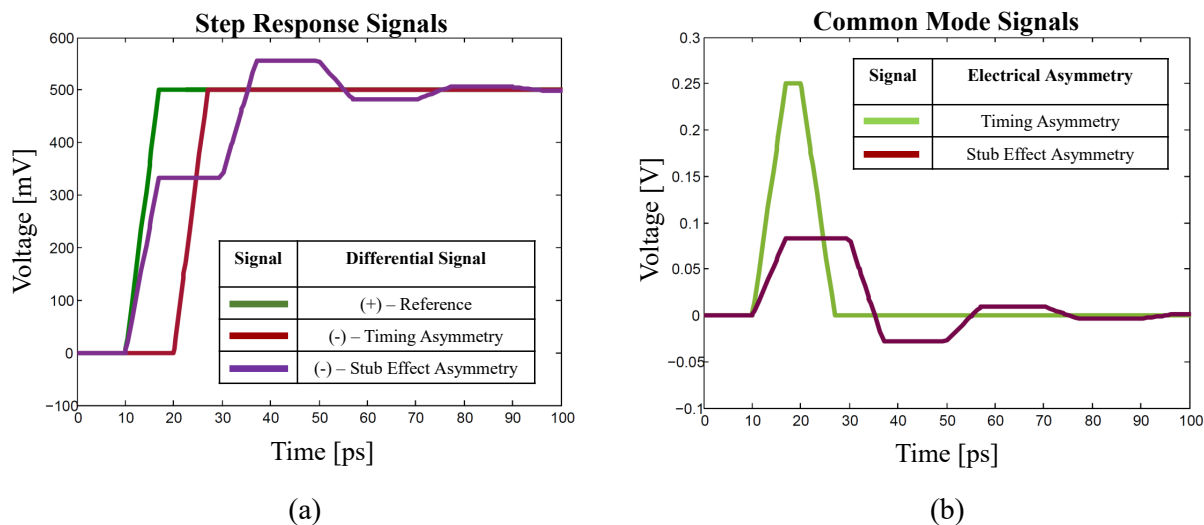


**Figure 5.3:** Skew effect observed at the Port 02 (+/-) in the differential pair for symmetrical and asymmetrical via stub cases (a) timing and stub effect for step responses, and (b) common-mode signals for each case, respectively. Generator and termination impedances are 50 Ohm.

edges. These residual via stubs can be present in several scenarios. Thus, regarding the manufacturing process, tolerances in back-drilling processes can result in residual stubs of around 10 mil and these small differences can also introduce mode conversion, which results in a timing asymmetry in the differential pair. In order to clarify this statement, Figure 5.3 presents the asymmetry effect reflected in time domain, from the step response and common-mode signals perspective. As depicted in Figure 5.3 (a), the effect of a stub asymmetry is reflected by steps in the edges. This effect induces a skew in the differential pair that is converted into common mode signals. Figure 5.3 (b) shows common mode signals caused by a phase shifting and skew by the stub effect. In this lane, extreme cases with the effects of long and short stubs are considered in order to analyze the effect in frequency domain and understand the scenarios under this could be a relevant issue that can affect differential links.

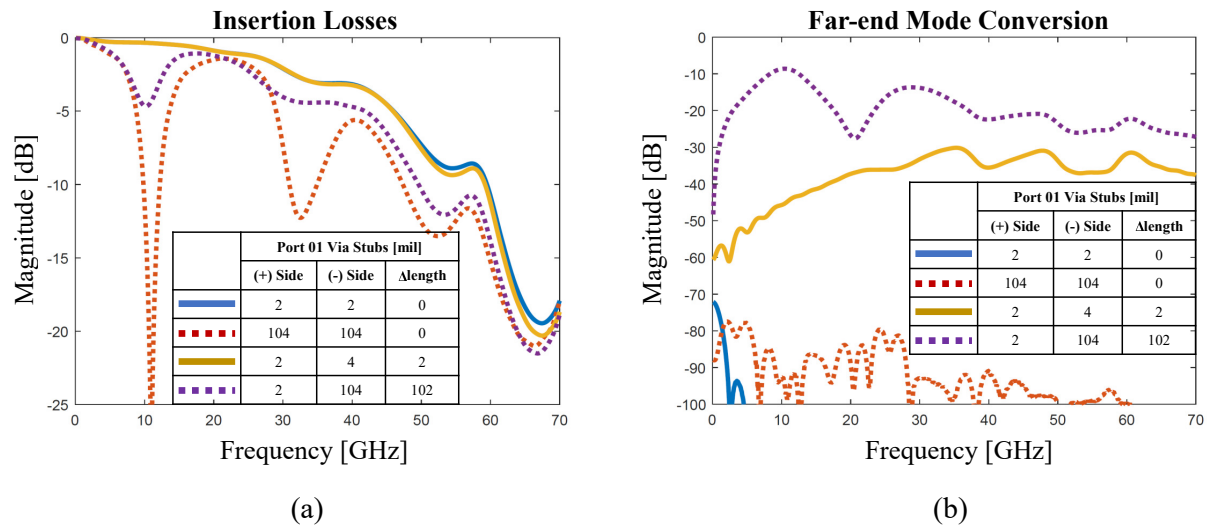


**Figure 5.4:** Via stub effect in (a) differential transmissions, and (b) far-end mode conversion for reference cases including symmetric and asymmetric configurations. The mode conversion magnitude has a direct relation with the differential via asymmetry. Simulations performed with FIT method [10], considering a reference impedance of 50 Ohm.

Thus, Figure 5.4 describes the cases of transmission (a) and mode conversion (b) depending of via stub configuration, i.e. symmetrical or asymmetrical structures. For the cases when there is no asymmetry, the mode conversion remains below -70 dB. This behavior is different to the insertion loss, where it is observed that the long via stubs clearly induce resonant frequencies. Even, an asymmetry of 2 mil among short via stubs induces a higher amount of mode conversion in comparison to the symmetric case with 104 mil stub length in Port 01 (+) and (-). Hence, asymmetries in via stub configurations are the main source of mode conversion and not the stub length in symmetrical cases. Results show that the maximum value of mode conversion is present around the resonant frequencies. Based on this, the asymmetry that causes the mode conversion does not depend only on the length difference of the intentional electrical path, but also on the unintentional path along the stubs, whose length is linked to the maximum magnitude of the mode conversion. Also, balanced asymmetries in both sides of the differential pair do not imply a mitigation of mode conversion. In fact, a cancellation of the effect due to asymmetrical via stubs can exist only in a full-symmetrical configuration, where the sides of the differential pairs have the same via stub lengths on the same physical sections of the interconnection. For residual via stub length ranges, Figure 5.5 (a) presents the magnitudes of mode conversion for specific asymmetries. Compared with the cases when the asymmetry between the differential via stubs increases from 2 to 22 mil, mode conversion has an increment of around 25 dB. An important fact to consider is that asymmetries at the order of a cavity thickness can induce mode conversion up to -15 dB, which are in the range of the back-drilling tolerances. Besides, another case of interest to analyze is the effect of mode conversion for different fundamental frequencies, which can be important for the electrical performance in the design of high-speed links. In that way, Figure 5.5 (b) shows the far-end mode conversion as a function of the asymmetry of the differential via stubs,

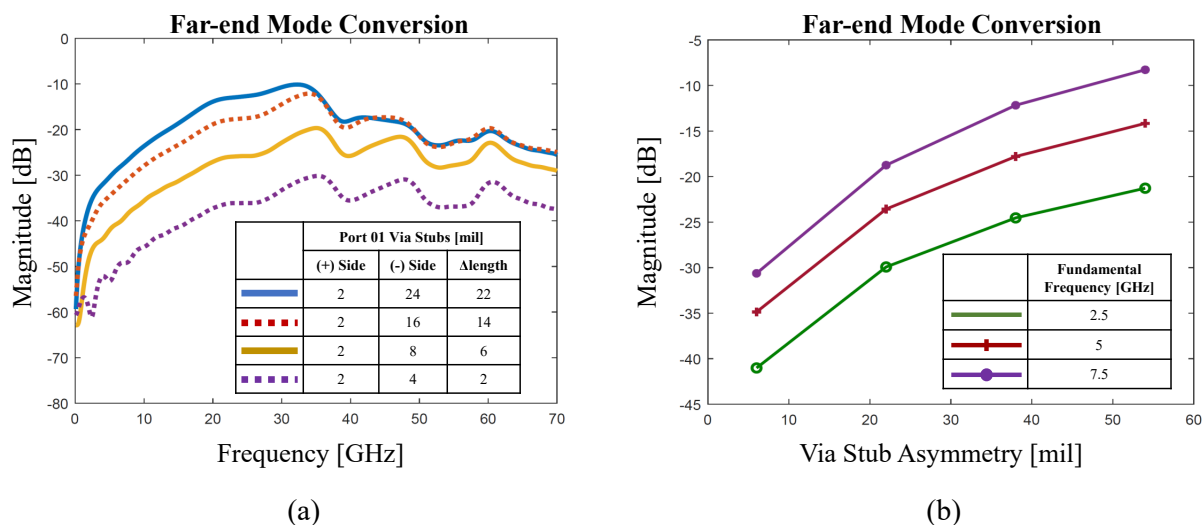


**Figure 5.5:** Magnitude of far-end mode conversion for different via stub asymmetries. In (a), it is depicted the effect of asymmetries in the order of back-drilling residual tolerances, and in (b) the magnitude across fundamental frequencies and via stub asymmetries as well.

for three different fundamental frequencies. Similarly, Within the range of one cavity thickness, i.e. from 10 to 20 mil, the impact of the stub asymmetry on the far-end mode conversion is between -20 and -30 dB.

## 5.2 Estimation of Mode Conversion as a Function of Via Stub Mismatches

It has been shown that residual via stub length asymmetries can contribute to mode conversion. In the previous section, mode conversion due to residual via stubs at the length order of back-drilling process tolerances was investigated. These asymmetries can induce a mode conversion above -20 dB for the specific fundamental frequency of 17.5 GHz. Thus, in order to get a better understanding of this effect, Figure 5.6 describes an electrical representation where the Port 01 (-) has a longer via stub than Port 01 (+). The signals in the differential pair have different delay times at the Port 02, because of the difference of stub lengths introduces an extended electrical path on the (-) side of the link [47]. At the moment when the signal arrives at the interface of the stripline and the via stub, part of the signal propagates through the stub and then is reflected, which causes a delay in the signal arriving at the Port 02 (-). This explains the root cause of the mode conversion, where the field distribution is not symmetrical at the time the differential signals arrive to that channel section. Actually, even though the asymmetry is compensated in different sections of the physical channel, the mode conversion may be worst, since the conversion occurs directly at the time the signals face to an asymmetrical channel section across the differential pair.

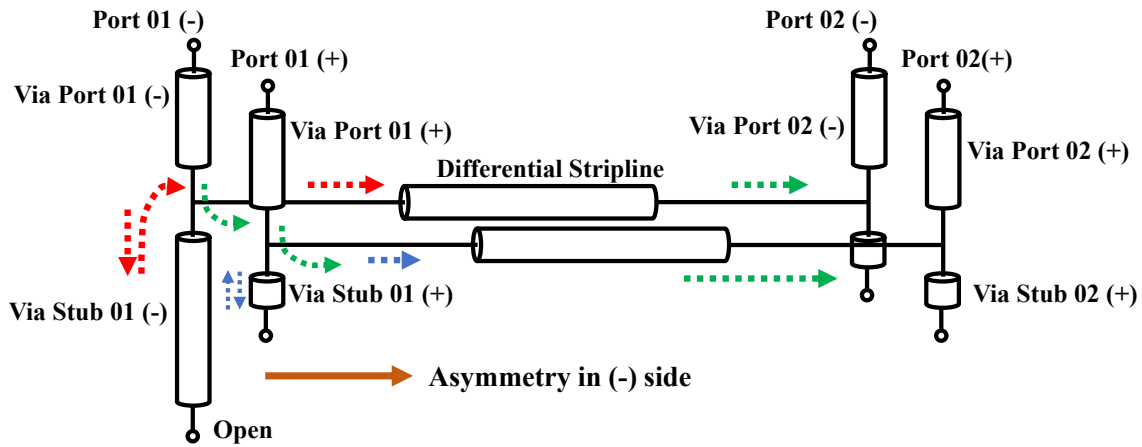


**Figure 5.6:** Asymmetric differential via-to-via link under analysis: electrical description of the stub effect in a differential pair. Skew exists between the signal (-) and signal (+) due to part of the signal propagating through the via stub and then being reflected (the red signal)

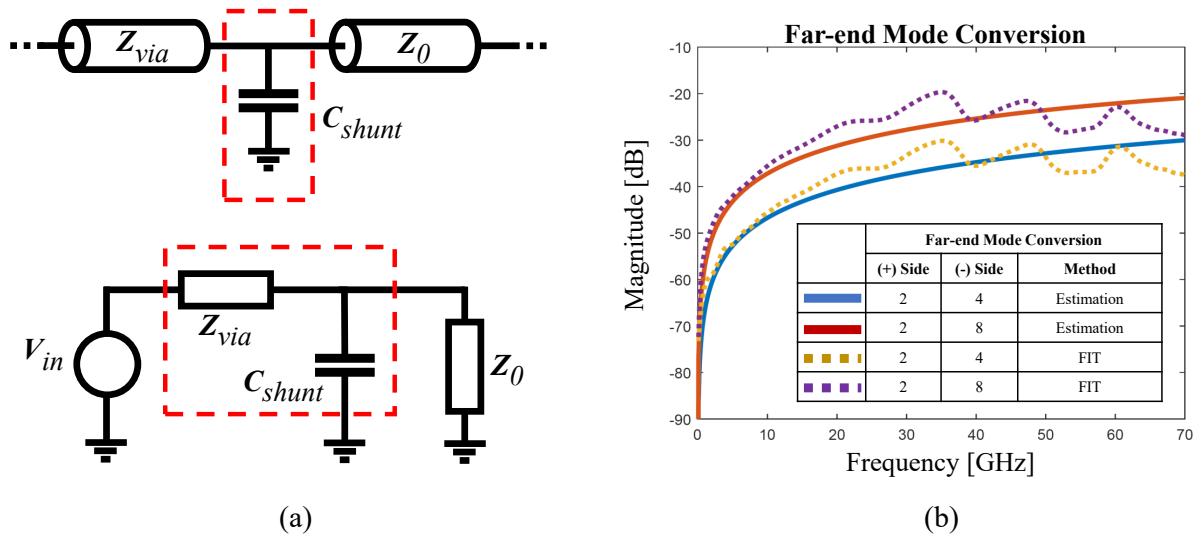


**Figure 5.7:** Estimation of the far-end mode conversion magnitude (a) modeling approximation based on a first order low-pass filter and (b) frequency response as a function of the length stub difference. This approximation is based on low frequency response of the  $\Delta l_{stub}$  in the differential configuration.

Here, an analysis of the estimation of far-end mode conversion as a function of this length asymmetry is carried out. For relative low-frequency ranges, the via stub can be considered as a shunt capacitor if the via stub delay is shorter than half of signal rise time, approximately. For instance, a worst stub length asymmetry scenario is defined in previous analysis as 102 mil, which represents approximately a round trip time of the signal of 34.54 ps, i.e. two times the stub delay time. Based on that statement, it is possible to represent the via stub as a lumped element, by considering a rise time of 35 ps (maximum frequency of 14.28 GHz), which is around two times the maximum time delay present in the configuration. In this way, in each side of the differential pair, the discontinuities can be simplified as a combination of the via impedance ( $Z_{via}$ ) and

an equivalent stub capacitances ( $C_{shunt}$ ). This is depicted in Figure 5.7 (a), where the channel section is considered as a first-order low-pass filter with the respectively lumped circuit equivalence. Thus, a low-pass behavior is present, and the capacitance can be approximated as follows:

$$C_{shunt} \approx \frac{l_{stub}}{v_{ph} \cdot Z_{via}} \quad (5.1)$$

where  $l_{stub}$  is the physical length of the via stub and  $v_{ph}$  is the propagation velocity in the substrate. Based on (5.1), the calculation of the associated capacitance of each via stub allows the estimation of the mode conversion magnitude for low frequencies as a first approximation, in order to correlate the effect with stub asymmetries, by assuming a via impedance value of 50 Ohms. For example, Figure 5.7 (b) shows the estimation for the cases when the  $\Delta l_{stub}$  is 2 and 6 mil, respectively. These estimations are correlated with full-wave FIT simulations [10]. A good agreement can be observed up to 10 GHz. Table 5.1 shows some correlation values between full-wave results and the proposed estimation, for the fundamental frequency of 2.5 GHz, where the maximum deviation across correlations is not above 2 dB.

**Table 5.1:** Magnitude of far-end mode conversion for different via stub asymmetries.

Reference Case [mil]	Fundamental Frequency - @2.5 GHz	
	FIT [dB]	Estimation [dB]
$\Delta l_{stub} = 22$	-30.33	-31.95
$\Delta l_{stub} = 14$	-34.51	-35.86
$\Delta l_{stub} = 6$	-42.11	-43.21
$\Delta l_{stub} = 2$	-52.44	-52.75

© 2019 IEEE. Reprinted with permission, from J. Cedeño-Chaves, et al. *Mode Conversion Due To Residual Via Stubs in Differential Signaling*. IEEE 23rd Workshop on Signal and Power Integrity (SPI), pp. 1-4, 2019.



# Chapter 6

## Conclusions and Outlook

In this thesis, the physics-based modeling approach has been revisited and two main contributions have been done. The correlation has been made by using network parameters, and the comparison between solutions of full-wave and the proposed modeling has validated the viability of the approach in a multilayer substrate simulation framework.

First, the evaluation of the model to handle microstrip line transitions in a generalized way with a simple transition model that works well up to 12 GHz for typical through-hole high-speed stack dimensions. Through this integration, a semi-analytical modeling proposal for turning vias is developed and validated, which suggests an acceptable agreement up to 12 GHz, with a maximum deviation of around 5 dB. The validation results have shown that the influence of the number of cavities for a generic stackup is not relevant in terms of the frequency range where the modeling approach has viability, whereas the improvements on the return path by getting closer to the ground vias placement achieve a good agreement up to around 15 GHz.

The second contribution was the study of the impact of asymmetrical stubs, which escapes the physics-based modeling capabilities, but it is shown to be a potentially important effect that can impact the performance of high-speed differential links. Differences in the order of the tolerance of the back-drilling process can induce a mode conversion higher than -20 dB. A low-frequency analysis was used to approximate the amount of mode conversion depending on the via stub length asymmetry. From this part of the work, a conference submission was presented and published.

As part of the further investigations, a more detailed analysis of the high-order modes as a function of the axial charge density can be addressed. Also, a specific case of study includes the understanding of the via-to-stripline transitions into the antipad sections. There exist approximations based on the decoupling of the cavity and stripline modes, but a generalization of the electromagnetic behavior of the via transitions to regular traces might need a dedicated analysis.

Moreover, a comparative analysis against other known mode conversion sources, such as asymmetrical ground via configurations, and the effect of multiple via stub asymmetries

can be studied. Besides, a formulation for the coupling across the antipad section when there exists via stubs under different symmetrical and asymmetrical scenarios, as well as the effect of the propagation of high-order modes under different characteristic impedance cases.

# Bibliography

- [1] R. Rimolo-Donadio. *Development, Validation, and Application of Semi-Analytical Interconnect Models for Efficient Simulation of Multilayer Substrates*. Doctoral Dissertation, Institute of Electromagnetic Theory, TUHH, 2011.
- [2] A. G. Williamson. *Radial-line/coaxial-line junctions: analysis and equivalent circuits*. International Journal of Electronics, vol. 58, no. 1, pp. 91-104, Jan. 1985.
- [3] Y. Zhang and J. Fan. *An Intrinsic Circuit Model for Multiple Vias in an Irregular Plate Pair Through Rigorous Electromagnetic Analysis*. IEEE Transactions on Microwave Theory and Techniques, vol. 58, no. 8, pp. 2251-2265, Aug. 2010.
- [4] S. Müller. *Via Array Modeling for Application in Fast, Energy-Efficient Digital Systems*. Doctoral Dissertation, Institute of Electromagnetic Theory, TUHH, 2014.
- [5] R. Rimolo-Donadio, H. Brüns, and C. Schuster. *Including Stripline Connections into Network Parameter Based Via Models for Fast Simulation of Interconnects*. 20th International Zurich Symposium on Electromagnetic Compatibility, Zurich, pp. 345-348, 2009.
- [6] H. Wang, S. Pan, J. Kim, A. E. Ruehli, and J. Fan. *Capacitance Calculation for Via Structures Using an Integral Equation Method Based on Partial Capacitance*. IEEE Transactions on Components, Packaging and Manufacturing Technology, vol. 3, no. 12, pp. 2134-2146, Dec. 2013.
- [7] A. Hardock. *Design of Passive Microwave Components on Multilayered Printed Circuit Boards Using Functional Vias*. Doctoral Dissertation, Institute of Electromagnetic Theory, TUHH, 2015.
- [8] Y. Zhang, J. Fan, G. Selli, M. Cocchini, and F. de Paulis. *Analytical Evaluation of Via-Plate Capacitance for Multilayer Printed Circuit Boards and Packages*. IEEE Transactions on Microwave Theory and Techniques, vol. 56, no. 9, pp. 2118-2128, Sept. 2008.
- [9] K. C. Gupta and M. D. Abouzahra. *Analysis and Design of Planar Microwave Components*. New Jersey, USA: IEEE Press, Chapter 3, pp. 75-86, 2004.
- [10] CST Corporation. *CST EM Studio Ver. 2015*. CST EM Studio [Online]. Information available: <https://www.cst.com/>, 2015.

- [11] D. G. Kam, M. B. Ritter, T. J. Beukema, J. F. Bulzacchelli, P. K. Pepeljugoski, Y. H. Kwark, L. Shan, X. Gu, C. W. Baks, R. A. John, G. Hougham, C. Schuster, R. Rimolo-Donadio, and B. Wu. *Is 25 Gb/s On-Board Signaling Viable?* IEEE Transactions on Advanced Packaging, vol. 32, no. 2, pp. 328-344, May. 2009.
- [12] M. Leone and V. Navratil. *On the electromagnetic radiation of printed-circuit-board interconnections.* IEEE Transactions on Electromagnetic Compatibility, vol. 47, no. 2, pp. 219-226, May. 2005.
- [13] V. Stojanovic and M. Horowitz. *Modeling and analysis of high-speed links.* Proc. IEEE Custom Integr. Circuits Conf. pp. 589-594, 2003.
- [14] C. Schuster, Y. H. Kwark, G. Selli, and P. Muthana. *Developing a physical model for vias.* Proc. IEC Designcon Conf. pp. 1-24, Santa Clara, CA, USA, Feb. 2006.
- [15] R. Rimolo-Donadio, X. Gu, Y. H. Kwark, M. B. Ritter, B. Archambeault, F. de Paulis, Y. Zhang, J. Fan, H. Brüns, and C. Schuster. *Physics-Based Via and Trace Models for Efficient Link Simulation on Multilayer Structures Up to 40 GHz.* IEEE Transactions on Microwave Theory and Techniques, vol. 57, no. 8, pp. 2072-2083, Aug. 2009.
- [16] S. Müller, X. Duan, M. Kotzev, Y. Zhang, J. Fan, X. Gu, Y. H. Kwark, R. Rimolo-Donadio, H. Brüns, and C. Schuster. *Accuracy of Physics-Based Via Models for Simulation of Dense Via Arrays.* IEEE Transactions on Electromagnetic Compatibility, vol. 54, no. 5, pp. 1125-1136, Oct. 2012.
- [17] G. Selli, C. Schuster, and Young Kwark. *Model-to-hardware correlation of physics based via models with the parallel plate impedance included.* IEEE International Symposium on Electromagnetic Compatibility, pp. 781-785, 2006. EMC 2006, Portland, OR, USA, 2006.
- [18] C. Schuster, G. Selli, Y. H. Kwark, M. B. Ritter, and J. L. Drewniak. *Progress in representation and validation of physics-based via models.* IEEE Workshop on Signal Propagation on Interconnects, pp. 145-148, Genova, 2007.
- [19] M. Stumpf and M. Leone. *Efficient 2-D Integral Equation Approach for the Analysis of Power Bus Structures With Arbitrary Shape.* IEEE Transactions on Electromagnetic Compatibility, vol. 51, no. 1, pp. 38-45, Feb. 2009.
- [20] X. Duan, R. Rimolo-Donadio, H. Brüns, and C. Schuster. *Circular Ports in Parallel-Plate Waveguide Analysis With Isotropic Excitations.* IEEE Transactions on Electromagnetic Compatibility, vol. 54, no. 3, pp. 603-612, June 2012.
- [21] X. Duan, R. Rimolo-Donadio, H. Brüns, and C. Schuster. *Extension of the Contour Integral Method to Anisotropic Modes on Circular Ports.* IEEE Transactions on Components, Packaging and Manufacturing Technology, vol. 2, no. 2, pp. 321-331, Feb. 2012.

- [22] Guang-Tsai Lei, R. W. Techentin, P. R. Hayes, D. J. Schwab, and B. K. Gilbert. *Wave model solution to the ground/power plane noise problem*. IEEE Transactions on Instrumentation and Measurement, vol. 44, no. 2, pp. 300-303, Apr. 1995.
- [23] J. C. Parker. *Via coupling within parallel rectangular planes*. IEEE Transactions on Electromagnetic Compatibility, vol. 39, no. 1, pp. 17-23, Feb. 1997.
- [24] S. Gao, F. de Paulis, E. Liu, A. Orlandi, and H. M. Lee. *Fast-Convergent Expression for the Barrel-Plate Capacitance in the Physics-Based Via Circuit Model*. IEEE Microwave and Wireless Components Letters, vol. 28, no. 5, pp. 368-370, May. 2018.
- [25] S. Gao, F. de Paulis, E. Liu, A. Orlandi, and H. M. Lee. *Transmission Line Representation of the Capacitive Via-Plate Interaction Toward a Capacitor-Free Via Model*. IEEE Transactions on Components, Packaging and Manufacturing Technology, vol. 9, no. 11, pp. 2248-2256, Nov. 2019.
- [26] A. Hardock, D. Dahl, H. Brüns, and C. Schuster. *Efficient calculation of external fringing capacitances for physics-based PCB modeling*. IEEE 19th Workshop on Signal and Power Integrity (SPI), pp. 1-4, 2015.
- [27] S. Wu, X. Chang, C. Schuster, X. Gu, and J. Fan. *Eliminating via-plane coupling using ground vias for high-speed signal transitions*. IEEE-EPEP Electrical Performance of Electronic Packaging, San Jose, CA, pp. 247-250, 2008.
- [28] R. Rimolo-Donadio, A. J. Stepan, H. Brüns, J. L. Drewniak, and C. Schuster. *Simulation of Via Interconnects Using Physics-Based Models and Microwave Network Parameters*. IEEE 12th Workshop on Signal Propagation on Interconnects, pp. 1-4, 2008.
- [29] I. N. Imam and L. M. Lamont. *An algorithm using the Schur complement in inverting large matrices*. IEEE Energy and Information Technologies in the Southeast', Columbia, SC, USA, pp. 421-426 vol.2, 1989.
- [30] C. R. Paul. *Decoupling the multiconductor transmission line equations*. IEEE Transactions on Microwave Theory and Techniques, vol. 44, no. 8, pp. 1429-1440, Aug. 1996.
- [31] A. E. Engin, W. John, G. Sommer, W. Mathis, and H. Reichl. *Modeling of striplines between a power and a ground plane*. IEEE Transactions on Advanced Packaging, vol. 29, no. 3, pp. 415-426, Aug. 2006.
- [32] T. Reuschel, S. Müller, and C. Schuster. *Segmented Physics-Based Modeling of Multilayer Printed Circuit Boards Using Stripline Ports*. IEEE Transactions on Electromagnetic Compatibility, vol. 58, no. 1, pp. 197-206, Feb. 2016.
- [33] T. Reuschel, M. Kotzev, D. Dahl, and C. Schuster. *Modeling of differential striplines in segmented simulation of printed circuit board links*. IEEE International Symposium on Electromagnetic Compatibility (EMC), pp. 911-916, Ottawa, ON, 2016.

- [34] C. Tsai, Y. Cheng, T. Huang, Y. A. Hsu, and R. Wu. *Design of Microstrip-to-Microstrip Via Transition in Multilayered LTCC for Frequencies up to 67 GHz*. IEEE Transactions on Components, Packaging and Manufacturing Technology, vol. 1, no. 4, pp. 595-601, April 2011.
- [35] S. Müller, X. Duan, R. Rimolo-Donadio, H. Brüns, and C. Schuster. *Non-uniform currents on vias and their effects in a parallel-plate environment*. IEEE Electrical Design of Advanced Package Systems Symposium, pp. 1-4, Singapore, 2010.
- [36] D. M. Pozar. *Microwave Engineering*. 4th Ed., New York, USA: John Wiley Sons, 2012.
- [37] B. C. Wadell. *Transmission Line Design Handbook*. Norwood, MA, USA: Artech House, 1991.
- [38] T. C. Edwards and M. B. Steer. *Foundations for Microstrip Circuit Design*. IEEE Press, John Wiley Sons, Ltd. United Kingdom, 2016.
- [39] ANSYS. Inc. (2018). *ANSYS Electromagnetics Suite Version 19.1.0*. ANSYS HFSS-TM 2018. Canonsburg, PA, USA. [Online]. Available: <http://www.ansys.com>, 2018.
- [40] CONMLS. (2017). *Multilayer Substrate Simulator CONMLS*. Institut für Theoretische Elektrotechnik, Technische Universität Hamburg, Hamburg, Germany. [Online]. Available: <http://www.tet.tuhh.de/en/concept-2/multilayer-substrate-analysis>, 2017.
- [41] R. Rimolo-Donadio, X. Duan, H. Brüns, and C. Schuster. *Differential to common mode conversion due to asymmetric ground via configurations*. IEEE Workshop on Signal Propagation on Interconnects, Strasbourg, pp. 1-4, 2009.
- [42] Y. Zhang, L. Ren, D. Liu, S. De, X. Gu, Y. H. Kwark, C. Schuster, and J. Fan. *An Efficient Hybrid Finite-Element Analysis of Multiple Vias Sharing the Same Antipad in an Arbitrarily Shaped Parallel-Plate Pair*. IEEE Transactions on Microwave Theory and Techniques, vol. 63, no. 3, pp. 883-890, March 2015.
- [43] H. Wang, A. E. Ruehli, and J. Fan. *Capacitance calculation for a shared-antipad via structure using an integral equation method based on partial capacitance*. IEEE 20th Conference on Electrical Performance of Electronic Packaging and Systems, pp. 271-274, San Jose, CA, 2011.
- [44] A. Hardock, R. Rimolo-Donadio, S. Müller, Y. H. Kwark, and C. Schuster. *Signal integrity: Efficient, physics-based via modeling: Return path, impedance, and stub effect control*. IEEE Electromagnetic Compatibility Magazine, vol. 3, no. 1, pp. 76-84, 2014.

- 
- [45] K. Scharff, T. Reuschel, X. Duan, H. Brüns, and C. Schuster. *Exploration of differential via stub effect mitigation by using PAM4 and PAM8 line coding*. 2017 IEEE 21st Workshop on Signal and Power Integrity (SPI), Baveno, pp. 1-4, 2017.
- [46] D. Kim, J. Byun, S. Lee, S. Oh, C. Schuster, K. Kang, and H. Lee. *Signal Integrity Improvements of a MEMS Probe Card Using Back-Drilling and Equalizing Techniques*. IEEE Transactions on Instrumentation and Measurement, vol. 60, no. 3, pp. 872-879, 2011.
- [47] G. Shiue, C. Yeh, L. Liu, H. Wei, and W. Ku. *Influence and Mitigation of Longest Differential via Stubs on Transmission Waveform and Eye Diagram in a Thick Multilayered PCB*. IEEE Transactions on Components, Packaging and Manufacturing Technology, vol. 4, no. 10, pp. 1657-1670, 2014.

